UNIVERSITY OF COPENHAGEN
FACULTY OF SCIENCE

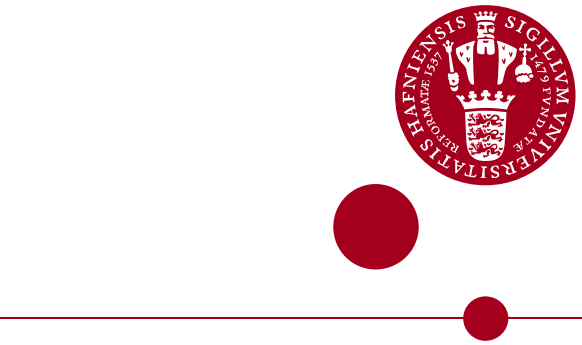

Probing the nuclear structure in ultra-relativistic heavy-ion collision with standardized cumulants of mean transverse momentum fluctuations

by

Frederik S. K. Rømer

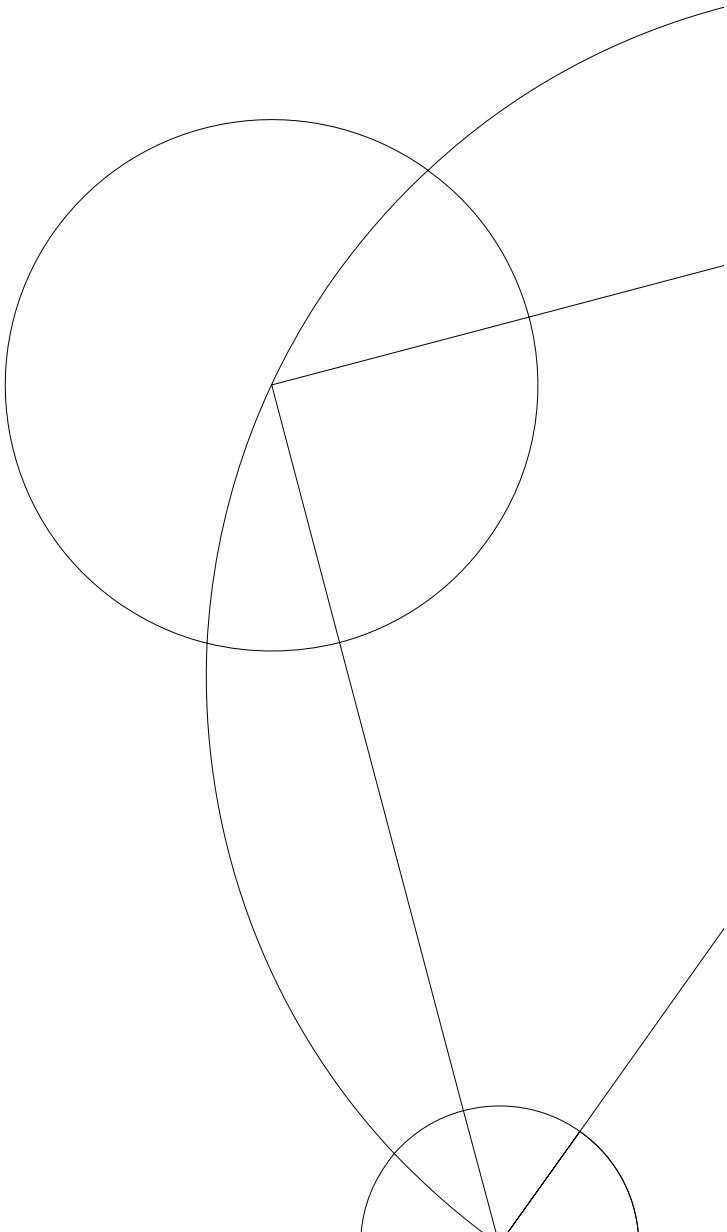

Supervisor: assoc. prof. You. Zhou

High Energy Heavy-Ion Group
The Niels Bohr Institute

Master thesis
22/05-2023
gtl238

Abstract

While it has been known for decades that most atomic nuclei can exhibit intrinsic deformation, it has recently been realized, that this information also can be accessed in ultra-relativistic AA collision at LHC energies. This motivates the exploration of high and low-energy experiments to act in conjecture with each other and to probe past the strong force to precisely characterize nuclear structures. Using higher order standardized cumulants of transverse momentum correlation $\widetilde{\kappa}(p_T'^m)$, a novel approach to accessing the initial conditions such as energy density and nuclear shape is presented. By analysing ultra-relativistic heavy-ions collision of ^{129}Xe and ^{208}Pb at LHC energies and comparing the transverse momentum p_T spectrum, it is investigated how quadrupole deformation β_2 and triaxiality γ affects the final p_T spectrum. Monte Carlo models such as HIJING and AMPT are employed to interpret the experimental results and provide a deeper understanding of the observed phenomena. The results show that while it should be possible to access information about the nuclear structure using standardized cumulants $\widetilde{\kappa}(p_T'^m)$, the current theoretical understanding of the probe does not allow for direct extrapolation of these quantities.

Acknowledgments

Firstly, I want to express my gratitude to my wife Christine Rømer, and our two beautiful children, Emma and Marvin. Two months before starting my bachelor's degree, Emma came into our lives, and one month before starting my master's degree, Marvin joined our family. Balancing studies with two young children would not have been possible without the immense love and unwavering support of my wife, who has always been there for our kids while I focused on reading, programming, and preparing for conferences. That is all while you also had your studies to take care of. You are the backbone of our family, providing love every day and every second of our lives. You three are my everything and always will be!

Secondly, I would like to extend my gratitude to my supervisor, You Zhou. Over the course of six years, we have worked together on various projects, starting from a simple first-year project to attending conferences such as Quark-Matter and soon Initial Stages. Your dedication and high ambitions have contributed immensely to my knowledge and growth. I cannot imagine a better mentor. Thank you!

I also want to thank the entire ALICE collaboration at the Niels Bohr Institute (NBI). Stepping into Building Q meant becoming part of the collaboration, attending group meetings, and participating in various activities. A special thanks go to Børge Svane, who organized a guided trip to Geneva during our first year, where we had the incredible opportunity to visit the LHC and get a close look at ALICE. This inspired me and increased my passion for studying high-energy physics. My appreciation for my fellow master's students Alexander, Mikkel, and Laura should also be mentioned. Our discussions, chats, coffee breaks, and shared laughter have made our time together memorable and enjoyable. I wish you all the best in everything you pursue. Lastly, a big thanks go out to Emil, who has been the go-to person for vital interpretation of results and discussion on nuclear structure heavy-ion collisions.

Me as DCS operator in ARC

"Do. Or do not
There is no try"

-Yoda

List of Contributions

1. **Probing nuclear deformation in ultra-relativistic collisions with higher order cumulants of transverse momentum fluctuations**
   Poster presentation at *Initial Stages 2023*

2. **Probing nuclear structure in heavy-ion collisions**
   Poster presentation at *Dansk Fysisk Selskab Årsmøde 2022*

3. **Generic formula for cumulants of mean transverse momentum fluctuation**
   Poster presentation at *Quark-Matter 2022*

4. **Searching for a droplet of QGP in proton-proton collisions**
   Poster presentation at *Dansk Fysisk Selskab Årsmøde 2019*

Contents

1 Introduction

In this introductory chapter, I will present the relevant terminology, theoretical concepts, and experimental aspects necessary for understanding the intricate phenomenology of heavy-ion physics and nuclear structure. Firstly, I will introduce the effective theory that describes the fundamental particles and forces in our universe, known as the Standard Model (SM). This will lay the foundation for a comprehensive explanation of ultra-relativistic heavy-ion collisions and their ability to serve as a means for probing the strong nuclear force. This will be followed by an explanation of the theoretical framework addressing nuclear deformation in both low and high-energy physics and how the coupling between the two fields can provide precise measurements of nuclear structures. Finally, the chapter will introduce the nuclear structure frameworks used in this thesis and in high-energy physics in general.

1.1 The standard model

The Standard Model (SM) of particle physics consists of the most fundamental description of all matter and interaction in our universe (not including gravity). The SM divides particles into two main types depending on the intrinsic quantity *spin*. The first type is the matter particles known as *fermions*, which constitute our visible universe. Fermions are particles with a half-integral spin that obey Fermi-Dirac statistics, which govern the behavior of indistinguishable particles. This is primarily described by the *Pauli's exclusion principle*, which describes the unique occupation of energy eigenstates in a quantum system [1, 2]. The second type is *bosons*, which act as the force carriers of all known matter and constitute the most fundamental exchanges between interacting particles. The bosons have a one-integral spin, and obey the laws of Bose-Einstein statistics. This is are contrary to fermions, meaning that a collection of bosons can occupy the exact same quantum state [1, 2]. A summary table of the SM particles and their respective properties, including mass, spin, and charge, can be seen below in Figure 1.1.

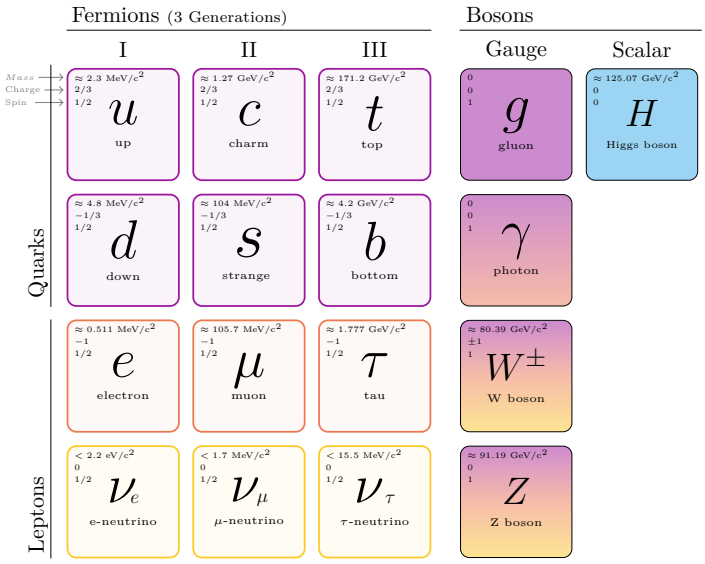

Figure 1.1: Illustration of the standard model of particle physics

Additionally, the fermions are split into quarks (q) and leptons (ℓ), each containing six particle species, commonly referred to as flavors. Each particle has a corresponding antiparticle, carrying the opposite charge but the same mass and spin[1]. The antiparticles are denoted as $\bar{q}$ and $\bar{\ell}$ for antiquarks and antileptons, respectively. Both quarks and leptons are arranged into generations

[1] Additionally, the antiparticles also carry the opposite flavor quantum number

that reflect a hierarchical mass structure, which increases according to the generation number[3]. Each generation of quarks contains two flavors: one carrying an electric charge of $+2/3$ and one carrying a negative charge of $-1/3$[2]. The six flavors of quarks are called *up* (u), *down* (d), *charm* (c), *strange* (s), *top* (t), and *bottom* (b). Although quarks are fundamental particles, they are never observed freely but only in the confined state as hadrons, either as quark triplets known as *baryons* (qqq), *antibaryons* ($\bar{q}\bar{q}\bar{q}$), or as quark doublets known as *mesons* ($q\bar{q}$). Some well-known examples of baryons are protons and neutrons consisting of (uud) and (udd) quarks, respectively. Additionally, the confinement of quarks inside baryons gives rise to the baryon number.

$$B \equiv N_q/3 = [N(q) - N(\bar{q})]/3$$

Here, $N(q)$ and $N(\bar{q})$ denote the total number of q and $\bar{q}$ present, respectively. While primarily an empirical law, the baryon number is a conserved quantity in all known interactions [4]. Consequently, this implies that each quark carries a baryon number $B = 1/3$, while anti-quarks carry $B = -1/3$. This conservation ensures that no free quarks are observed or left alone in interactions, which aligns with experimental observations. Each generation of leptons consists of a *charged lepton* ℓ and an associated *neutral lepton* (typically denoted as ν_ℓ). The charged leptons interact via both electromagnetic and weak nuclear interactions and can combine to form composite particles, such as atoms. On the other hand, neutral leptons only interact through the weak nuclear force and are typically detected through processes such as β-decays of atomic nuclei and hadrons. For example, a free neutron decays into a proton with the emission of a high-momentum electron and an electron antineutrino [5].

$$\mathrm{n} \rightarrow \mathrm{p} + e^- + \bar{\nu}_e$$

While lepton phenomenology is a complex and rich subject by itself, the leptons do not interact with the carrier of the strong nuclear force. Consequently, they do not contribute to nuclear models[3] and emphasis will therefore be put on quarks and the strong interaction.

Force carriers

Aside from the fundamental matter particles that constitute our universe, there are four fundamental forces: *gravity*, the *electromagnetic force*, the *weak force* and the *strong force*. Beside from gravity, each of the forces results from the exchange of so-called *carrier* particles that transfer energy from one particle to another. The force carriers belong to the boson group in the SM. The electromagnetic force is carried by the photon γ and interacts with all charged particles. As the photon does not carry charge itself it additionally does not interact with itself but has an infinite range of interactions. Secondly, the weak nuclear force is meditated by the charged $W^\pm$ and neutral Z bosons. Due to their large masses ($\approx 80\mathrm{GeV/c}$) they have a very short interaction length and therefore decay before they can be observed as final state particles. The weak force can be exchanged between all particles and account for the decay as well as the transformation of quark flavors. The before-mentioned decay of a free neutron to a proton can be seen in Figure 1.2, as illustrated through a Feynman diagram. The neutron decay is thus a more fundamental decay of one of the two u valance quarks, through the exchange of a W^- boson that subsequently decays to the observed electron (and not observed neutrino). The final interaction to outline is the strong nuclear force, but as it is of great importance of this thesis the next section will go through a dedicated explanation of the theory as well as current experimental measurements.

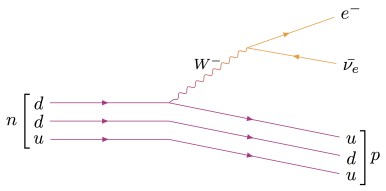

Figure 1.2: Illustration of a free decaying neutron to a proton under weak interaction

[2]The charge is given in units of elementary charge corresponding to the magnitude of the electric charge in an electron, $e = 1.602 \cdot 10^{-19}$ C

[3]Not to be confused with atomic models

1.1.1 Quantum Chromo Dynamics

Quantum Chromo Dynamic (QCD) is the effective theory describing quark interaction in the SM. The strong interaction is mediated by massless spin-1 bosons called *gluons* (g). Both quarks and gluons carry *color charges* denoted as *red* (r), *green* (g), and *blue* (b). The term color is not related in any way to the light we observe every day, but merely a label for the current state of the quark/gluon. Just like antiparticle carries opposite electromagnetic charge with respect to their particle counterpart, anti-quarks carries anti-color which are denoted as $\bar{r}, \bar{g}$ and $\bar{b}$. While there is a lot of experimental evidence for the existence of quarks, as well as color charge, it is a fact that we do not observe these particles or forces in nature and experiments. This has led to the hypothesis of *colour confinement* that only bind quarks as colorless objects[6]. Consequently, quarks can only combine into a singlet state, either in a hadron form as $(q^r q^g q^b)$, or meson form as $(q^r \bar{q}^{\bar{r}})$. With a bound colorless state the sum of color charges need to be zero which can be inferred by letting $r + g + b = 0$ and $r + \bar{r} = 0$.[4]. For a bound meson state, the movement of two quarks can be described by a non-relativistic potential with a column-like term from the color charge, and an additional confinement term that increases linearly with the separation distance[7].

$$V_{QCD}(r) \approx -\frac{4}{3}\frac{\alpha_s}{r} + \kappa r$$

A direct consequence of color confinement is that as the two quarks in a bound state are separated, an increased amount of energy will be deposited in the color field connecting them. At some point, it will become energetically favorable for the pair to split and create a new quark-antiquark pair as can be seen Figure 1.3

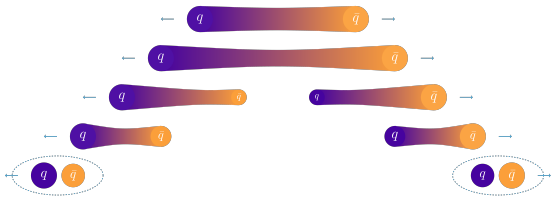

Figure 1.3: Illustration of the creation of a new quark anti-quark pair pulled from the vacuum as the color field tension increases

Asymptotic freedom

The exchange gluon between two quarks in their bound state can momentarily create a virtual quark anti-quark pair. Similarly like in QED, this can lead to a screening effect where a cloud of virtual $q\bar{q}$ pairs shields the original color charge at large distances (low energies). However, as the gluon can couple to its own charge, an additional virtual gluon-gluon pair can fluctuate in and out of existence, creating an additional cloud of color charges. Unlike the screening effect created by the intermediate quark-antiquark pairs, the gluon pairs act as a catalyzer of the color field between two quarks, creating an effective ant-screening thundercloud[7]. As the quark pair are separated the thundercloud grows more violent, and the attractive force is effectively increased. In addition, when the quarks are joined within a small proximity, they exist inside the eye of the cyclone, where the attractive forces diminish. As a consequence, they act as a quasi-free particle at low distances (high energies). This behavior is known as *asymptotic freedom* and effectively diminishes the coupling strength with respect to the momentum transfer Q. The coupling strength of the strong interaction can thus be expressed in terms of a *running* coupling constant given by[7].

$$\alpha_s(Q) \propto \left(\frac{1}{1 - \ln(Q^2/\mu^2)}\right)$$

[4] where the other two color neutral states of the mesons are given by $b + \bar{b} = 0$ and $g + \bar{g} = 0$

The running strength of $\alpha_s(Q)$ as obtained in different experiments, as well as different methods can be seen in Figure 1.4. As the strength $\alpha_s(Q)$ depends on the momentum transfer in the process, QCD can be divided into a non-perturbative low-energy regime, and a perturbative high-energy regime. This makes high-energy experiments suitable, and necessary, for probing the strong nuclear force.

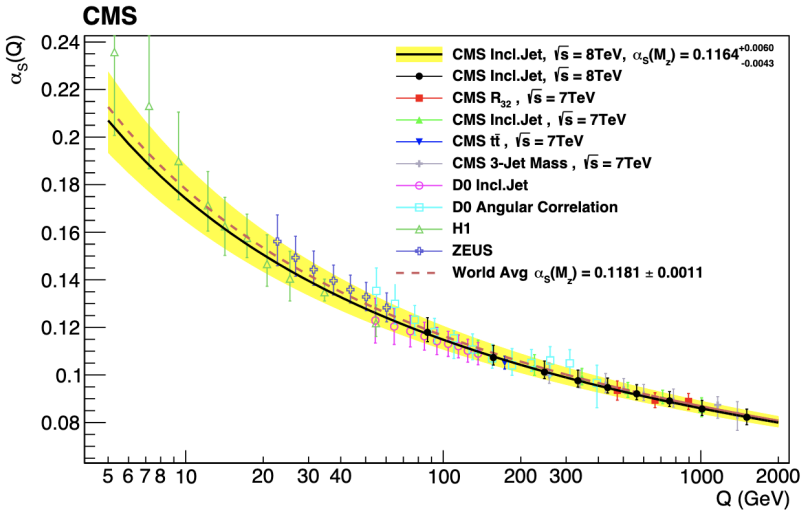

Figure 1.4: The running coupling constant $\alpha_s(Q)$ as a function of momentum transfer Q as obtained in a wide variety of different experimental methods. Figure taken from [8]

1.2 Heavy ion collisions

At the Large Hadron Collider, heavy nuclei such as lead (Pb) and xenon (Xe) are accelerated to ultra-relativistic energies before being brought into collision. With the close-to-light-speed velocities, the nuclei get Lorentz contracted into a high-density disk in the transverse plane. Consequently, at the impact of the two colliding nuclei, extreme energy densities are reached and the strong force effectively decouples from interacting partons, which makes a suitable environment for studying this complex force of nature. In this stage of the collision, the interacting system has reached a thermal equilibrium where the primordial matter of Quark-Gluon-Plasmsa (QGP) is formed at temperatures above $T_c \approx 145$ MeV[9]. This phase of matter, in where partons propagate in a deconfined state, has following proved to behave like an almost perfect liquid, with low shear viscosity[10]. Consequently the low shear viscosity results in a collective (fluid-like) expansion of partons, from the equilibrium stage until the system has once again cooled down and hadrons are formed. The main purpose of the ALICE experiments was to study and extract the transport properties of this form of matter. Though, while the strongly interacting matter of QGP has been studied to a great extent in decades, the pre-equilibrium condition, such as nuclear shape and initial interaction is not understood properly. With the collisions happening at ultra-relativistic energies the initial interaction of nucleons is well described in the transverse plane only. With this in mind, the initial conditions and sequent evolution dynamics of heavy-ion collision are often left to theoretical calculation and/or prediction in a transverse plane. From the onset of collision, the evolution can roughly be described by the following (summarised) stages[11] which are also illustrated in Figure 1.5

1. **Pre-equilibrium**
   The two nuclei collide and the first interaction of nucleons leads to chaotic hard processes. The hard processes are mainly responsible for the production of particles with large transverse energies, consequently resulting in hadronic jets.

2. **Thermal Equilibrium, QGP**
   Interacting partons reach a thermal equilibrium in which they can propagate freely. The system formed behaves as a strongly interacting fluid with low shear viscosity. The partonic fluid is characterized as Quark-Gluon-Plasma (QGP) and follows ideal hydrodynamics.

3. **Phase transition**
   As the system expands, it starts to cool down as it reaches a critical temperature T_c. In this phase, partons start to undergo hadronization which is the formation of hadrons out of gluons and quarks.

4. **Hadron gas**
   The system has completely transitioned from a fluid phase to pure hadronic gas. The hadron gas is composed of a system of free particles. This process is also characterized as the *freeze-out*.

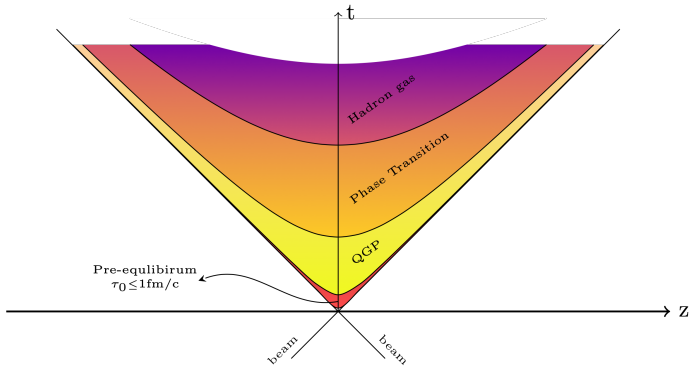

Figure 1.5: Illustration of the evolution of heavy-ion collision as described in light cone hyperbola along the beam axis z, and with proper time t.

While every aspect of the collision is crucial for a comprehensive understanding of its evolution, from the pre-equilibrium stage to the final stage of hadron gas, particular emphasis will be placed on the initial conditions. This focus stems from the clear assumption that the influence of nuclear deformation and its subsequent effects on final state observables play a dominant role during the pre-equilibrium and Quark-Gluon Plasma (QGP) stages. In the subsequent section, I will provide a summary of the effective theory that describes the initial stage interaction in heavy-ion collisions.

1.2.1 Pre-equilibrium and initial conditions

The initial conditions and sequent pre-equilibrium phase are to this date still one of the most incomplete subjects in heavy-ion collisions. While some models show excellent agreement between experimental measurements and simulation, more complex observables shows greater sensitivity to implementation physics, and small tunings of it[12]. The initial density profiles created by two colliding nuclei in the transverse plane are model dependent, as we do not have a complete understanding of it. One of the most used initial stage models, is the MC-Glauber model. The framework is based on a Monte-Carlo approach where nucleons are sampled from a density function in the xy plane. The resulting nucleon distribution of the colliding nuclei can be seen in Figure 1.6 (Left). Another model, the IP-Glasma, implements additional pre-collision effects such as Color-Glass-Condensate (CGC)[5] and treats the initial density profile with respect to gluon field and nucleons[14], see Figure 1.6 (Right). The large discrepancy between density

[5]CGC is a relativistic effect describing the evolution of gluon fields in high energy heavy-ion collisions [13]

profiles in models, shows the gap between theoretical understanding and implementation of the early stages in heavy-ion collisions. This emphasizes the need for additional studies to reveal the correct path.

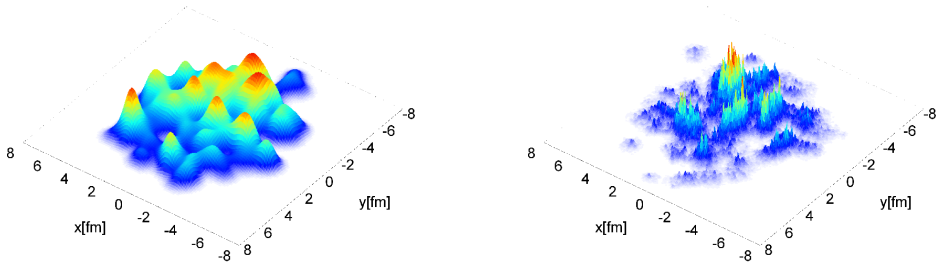

Figure 1.6: Initial energy density of a heavy-ion collision created by the nucleon projection in the transverse plane. Left: IP-Glasma model. Right: MC-Glauber model. Figure from [15]

Accessing the initial conditions

While we do not have direct access to the initial state of the colliding nuclei, recent studies have predicted an almost linear response of the energy density E and the measured mean transverse momentum $\langle p_T \rangle$ off final state particles[16]. With fixed impact parameter $b = 2.5$ fm, Pb-Pb collisions at $\sqrt{s_{NN}} = 5.02$ TeV are simulated. The system is then expanded in hydrodynamical evolution to final state particles. While the total entropy of the system were kept fixed for each event, the initial density profile were random, and fluctuated event by event. The results presented in Figure 1.7 show a clear positive correlation of the energy density E and $\langle p_T \rangle$. More interesting we note a negative correlation between the $\langle p_T \rangle$ and the size of the interacting system R implying a relation

$$\langle p_T \rangle \propto \frac{1}{R} \tag{1.1}$$

The presented results from the study in[16] and Equation 1.1 highlight the significance of the transverse momentum spectrum as a crucial observable for investigating the early stages of heavy-ion collisions. This observable can serve as a valuable tool not only for constraining initial stage models but also as a new direct supplement for studying nuclear structure. As a result, there is a strong motivation to utilize ultra-relativistic collisions as a complementary approach to low-energy experiments and the study of nuclear structure.

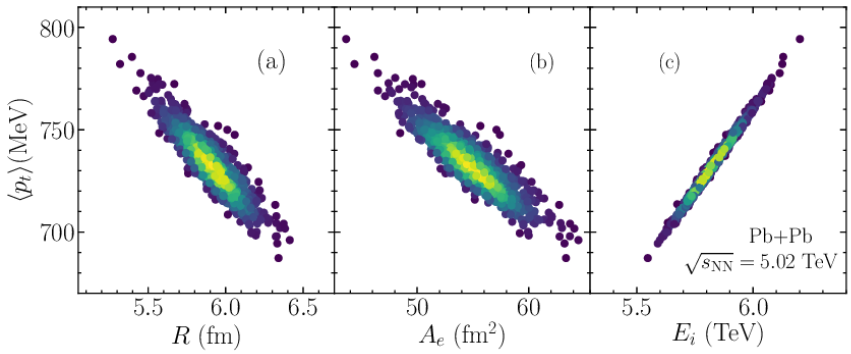

Figure 1.7: Correlation between initial energy density and final state transverse momentum of Pb-Pb collisions at $\sqrt{s_{NN}} = 5.02$ w. fixed entropy and impact parameter $b = 2.5$ fm

1.3 Nuclear structure

While the fundamental laws of particle physics are covered in great detail, and it is possible to obtain measurements with accuracies on the order $\approx 10^{-12}$[17], areas such as nuclear structure, are still very poorly understood. Some of the first accurate descriptions of atomic nuclei are made through the collective model created in 1975 by Aage Bohr and Ben Mottelson. The collective model is based on the already existing shell model, where nucleons follow a similar orbital structure as electrons, but also included additional rotations and collective motion within the shells[18, 19]. Since then, a number of ways have been introduced to effectively describe the nucleus in low-energy physics, both theoretical but also experimentally. The current state of nuclear theory covers *Ab Initio* calculations for atomic nuclei with atomic number up to $A = 60$. The *Ab Initio* approach is based on solving the non-relativistic Schroedinger equation for ground state nuclei, this includes all constituent nucleons and the additional forces between them[20].

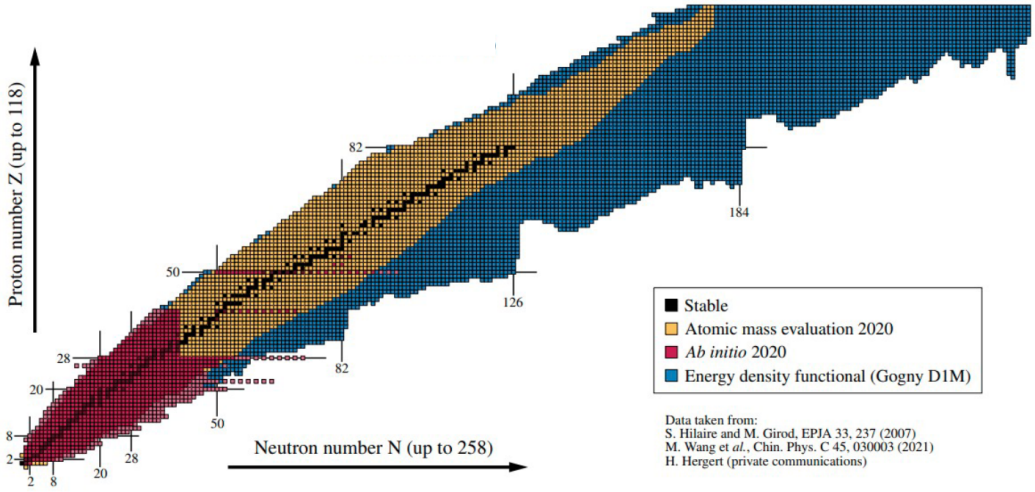

Figure 1.8: State as of 2020 of the nuclear chart. The chart shows the current description of atomic nuclei in Ab initial (red), Atomic mass evaluation (yellow), and energy density functional (blue). Figure taken from [21]

From these ground state descriptions of the nuclei, the low-energy experiment has been able to attribute transition energies of nuclei to fit the model description that favors multi-pole moments of the nucleon destribution[22, 23]. While it can not be observed directly due to the subatomic scale, the multipole moment directly impacts the shape of the nuclei by small shape perturbations. These perturbations of the nuclear shape lead to deformed nuclei. The deformation strength is denoted as β_n where n corresponds to the $n´$th multi-pole expansion of the nucleon density, and characterizes different shapes, such as quadruple deformation β_2, and octupole deformation β_3. While it is possible to experimentally measure the moments to some extent, the shape itself cannot be correctly determined. This can be due to $free$ nucleons in the nuclei that do not contribute much to the collective effects, and therefore not to the multi-pole mode. Though they are still there and thus contribute to additional shapes perturbation that can not be easily measured. The rms radius of the nucleon distribution of deformed nuclei can be described in terms of spherical harmonics to second order as[24, 25]

$$R'(\theta, \varphi) = R_0 \left[1 + \beta_2 \left[\cos(\gamma) Y_{20}(\theta, \varphi) + \sin(\gamma) Y_{22}(\theta, \varphi)\right]\right] \tag{1.2}$$

where the radius $R'(\theta, \varphi)$ denotes the nuclear surface, R_0 the rms radius of a spherical nuclei, β_2 the quadrupole deformation strength and γ the triaxiality. Though, in this more streamlined surface description of the nuclei, it is important to note that deformation strength β_2 does not

reflect the exact quadrupole moment as measured in low-energy physics[26]. To first order the dominant deformation is caused by the quadrupole moment of the nucleon density[24], which is also the reason why it is the only moment considered here. An illustration of the induced shape from Equation 1.2 can be seen in Figure 1.9, with fixed deformation strength $\beta_2 = 0.30$ and varying γ. Here it can also more clearly be noted how each shape is different, but they still carry the same quadruple moment.

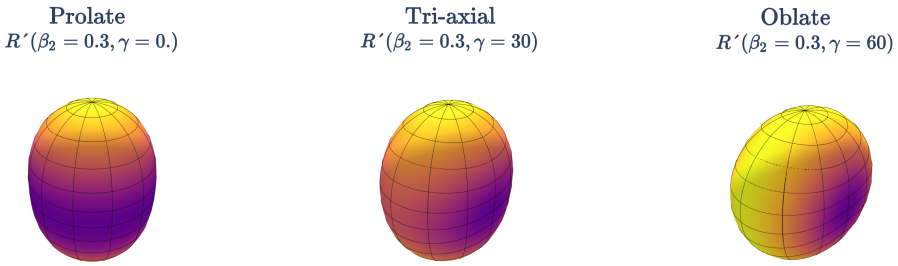

Figure 1.9: Illustration of the surface of nuclei with different quadrupole deformation. From left to right: Prolate, Tri-axial, Oblate. All carries the same deformation strength β_2 but different tri-axiality γ which consequently changes the shape

Though quadrupole deformation β_2 can be measured experimentally with great precision[22, 23], the current framework does not allow for precise measurements of the triaxial structure. In current studies [27] it can be observed, as shown in Figure 1.10, how experimental measurements of quadrupole deformation and triaxiality cannot be described by current theoretical models. The sensitivity to triaxial deformation suffers from larger deviations than measurements on β_2. Moreover, it can be noticed how the discrepancy between data and models on γ gets gradually larger for lighter nuclei with a small atomic number A, Figure 1.10 (Left). An important thing to remember is that the current studies of the nuclear structure only depend on the proton distribution through the charge radi of the nuclei. In a heavy-ion collision, we can obtain the total energy density that also accounts the neutrons. These challenging measurements bring forward the motivation for other fields and methods, to be brought forward, and to act in conjecture with current low-energy experiments.

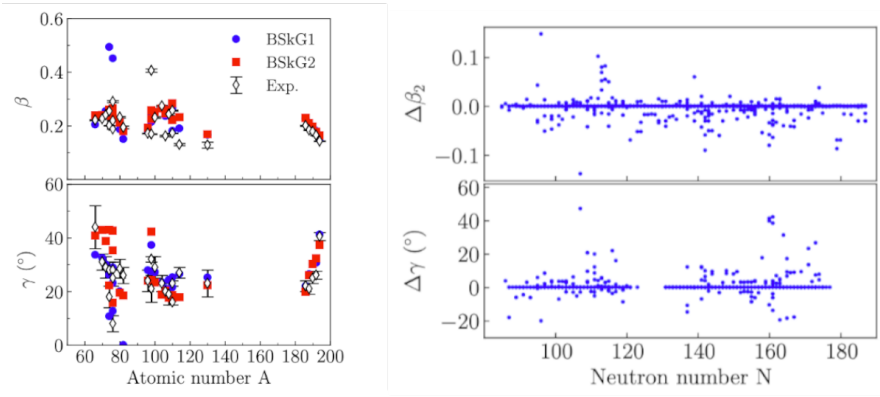

Figure 1.10: Comparison of low-energy measurements of β_2 and γ with respect to energy density functional nuclear theory BSkG. Left: Measurements of β_2 and γ and theoretical prediction in BSkG1 and BSkG2. Right: Difference between experiments and model prediction. Figure taken from Figure 1.10

1.3.1 Nuclear structure in high energy phsysics

As presented in the previous section, there exists an inverse correlation between the interacting system and the observed $\langle p_T \rangle$ of the final state particles. With the introduction of nuclear deformation, there should then also be accounted for a new type of collision. While the energy and system remain the same, the deformation of atomic nuclei gives rise to rotational degrees of freedom. Thus for nuclei that have a quadrupole deformation, their bodies will be elongated along some principal axis. For ultra-central collisions, where the quadrupole deformed nuclei are colliding at a small impact parameter $b \approx 0$, we can distinguish two very different types of collisions, depending on their orientation, at the moment of impact. If both their principal axis are aligned in the xy-plane, we consider a body+body collisions which consequently produces a large overlap area. This effectively spreads out the nucleons across a larger area and the interaction system is therefore also larger. Likewise, we can also have a tip+tip collision where the principal axis is aligned with the z-plane. This however will concentrate the same amount of energy as in body+body collisions but on a smaller area. Following Equation 1.1 where we know $\langle p_T \rangle \propto 1/R$, the interacting system will be denser and the subsequent explosion will bare larger. A schematic of the different kinds of collisions with respect to different deformation parameters is outlined in Figure 1.11.

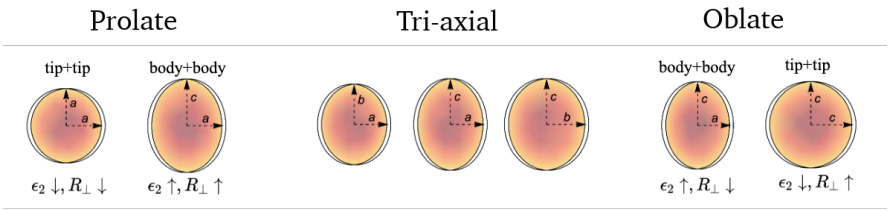

Figure 1.11: The initial density profile in the collision of deformed nuclei. Here it can be seen how the deformation of nuclei directly affects the overlap of the colliding nuclei, and consequently how the initial energy density will depend on it. Taken from [24]

In simulations of heavy-ion collision the colliding nuclei are typically sampled by the geometric Glauber model as also introduced in the previous section. As the Glauber model is based on nucleon sampling in the transverse plane it is possible to introduce rotations of the colliding nuclei before the projection is made. The nucleon distribution in atomic nuclei is in high-energy physics, modeled by the mean-field *Wood-Saxon* (WS) potential, given by

$$\rho(r, \theta, \varphi) \propto \frac{n_0}{1 + \exp([r - R'(\theta, \varphi)]/a_0)} \tag{1.3}$$

Here n_0 is the nucleon density, a_0 is the surface diffusion and r denotes the distance from the center of the nuclei. Though instead of using the radius of spherical nuclei, the radius $R'(\theta, \varphi)$ is given as in Equation 1.2 for the surface of deformed nuclei. The possibility of varying these parameters makes it a suitable tool for studying the effect of nuclear deformation on final state observables in collisions at the LHC energies.

In part of this thesis, heavy-ion collisions of ^{129}Xe are simulated. By varying β_2 and γ, different shapes are created, from where it is studied, if the nuclear shape affects the final $\langle p_T \rangle$ fluctuations. This will directly be compared to Xe-Xe and Pb-Pb collision at the LHC to see if like signals can be observed, and if it is possible to probe the nuclear structure with $\langle p_T \rangle$ fluctuations.

2 Experimental setup

This chapter provides a brief summary of the experimental setup for obtaining data in heavy-ion collisions. As this does reflect the most hours of work, and most relevant measurements, the simulation of deformed AA collisions will be summarised inAppendix D. Firstly, the Large Hadron Collider (LHC) is introduced. Subsequently, the main experiment of the analysis, A Large Ion Collider Experiment (ALICE), is presented, along with a description of the sub-detectors. It should be noted that many of the sub-detectors have undergone major (and minor) upgrades since the construction of ALICE. Hence, the focus will be on the detector state during LHC Run2, as all the presented data were obtained during this period.[6]. Finally, the base unit for measurements, the centrality classification is presented.

2.1 The Large Hadron Collider (LHC)

The Large Hadron Collider (LHC) is located on the France-Schweiz border near Geneva and is currently the largest and most powerful particle accelerator in the world[28]. The accelerator components and detectors are placed in a circular tunnel with a circumference of 27 Km, located approximately 100 m below the surface. The accelerator consists of an alternating set of electromagnets and electromagnetic cavities used to accelerate and focus the particles respectively. The main colliding system is proton-proton (pp), and lead-lead (Pb-Pb) but a special test run of Xenon-Xenon (Xe-Xe) has also been recorded in 2017[29]. Each proton beam is accelerated to a maximum of 7 TeV before colliding, resulting in a center-of-mass energy $\sqrt{s} = 14$ TeV, while the Pb-Pb nuclei collide with $\sqrt{s_{NN}} = 5.02$ TeV. As the particles reach the desired energy, the beams are made to collide at interaction points where dedicated detectors are placed to record, detect and discover physic. Along the LHC ring, there are four major experiments located, ATLAT, CMS, LHCb and ALICE as can be seen marked in blue text in Figure 2.1. ATLAS and CMS are general purpose detectors built to explore a broad range of physics, and played the key role in the discovery of the Higgs boson[30][31]. The LHCb is one of two dedicated detectors and are built to study matter-antimatter relations[32], additionally, it is the only forward spectrometer[7]. The final of the four experiments is the ALICE detector, which acts as the second dedicated experiment. The main purpose of ALICE is to study the strong interaction in the extreme energy densities that are reached in heavy ions collisions[33]. With this project and analysis being an active component of ALICE, a more in-depth description of the experiment will be given in the following section.

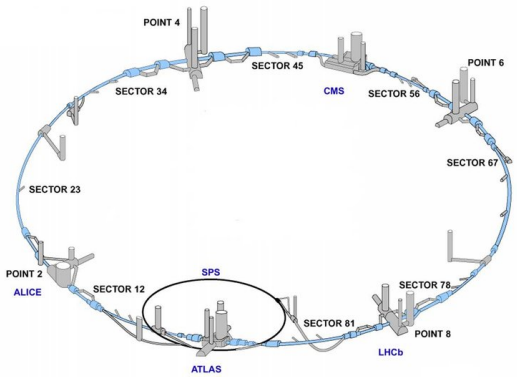

Figure 2.1: Schematic of the Large Hadron Collider and the four major experiments located at CERN. Figure taken from [34]

[6]LHC Run2 spanned from early 2015 to 2018
[7]The particles are not colliding with each other but with an end "plate"

2.2 A Large Ion Collider Experiment (ALICE)

A Large Ion Collider Experiment (ALICE)[33, 35, 36] is one of the four major experiments located at the LHC. The collaboration itself, where founded in 1993 and currently consist of roughly 2000 active members, spread across a total of 40 countries. Additionally, the ALICE Collaboration has an active Junior program that ensures educational quality and engagement of both young and early career scientists. The detector is designed to investigate the strongly interacting matter under extreme energy densities. Under these conditions, it is possible to recreate the dense QGP fluid which composed our universe in the first few microseconds after the big bang. The detector consists of numerous specialized sub-detectors, each designed for specific collision dynamics, and can roughly be categorized into a central and forward segment. The central segment is used for high-resolution tracking and particle identification, and is covered by a large solenoid magnet, see Figure 2.2. It consists of three Si semiconductors which form the Inner Tracking System (ITS), a Time Projection Chamber (TPC), and the Time-Of-Flight (TOF) detector. The forward segments are used for global collisions characteristic and are positioned with relatively small angles with respect to the beam-axis, in both the forward and backward regions. In the forward and backward region is the Zero-Degree-Calorimeter (ZDC) used for event characterization, and the VZERO detector used for centrality determination.

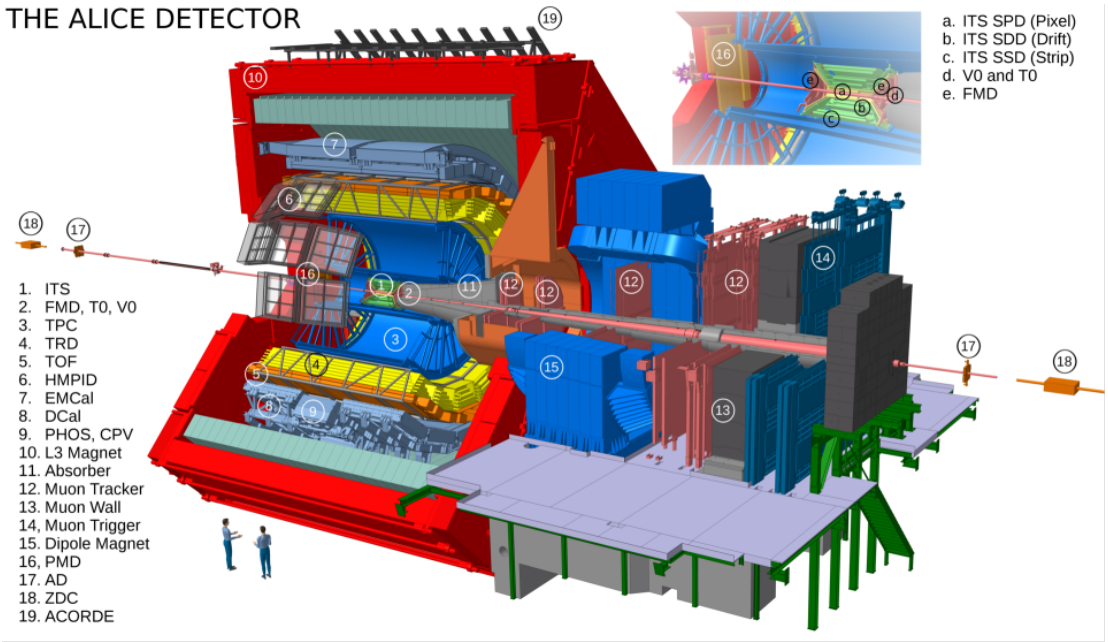

Figure 2.2: Schematic of the ALICE detector during run2. Figure taken from [37]

2.2.1 Detector components

In the following section, a technical description will be presented for the ITS, TPC, and VZERO sub-detectors which are the most important detectors concerning this thesis. While every component of ALICE composes a vital part of the whole experiment, a description of every sub-detector would simply be out of scope. Each section is based on technical design reports in which the relevant references will be made at the beginning of each section.

Inner Tracking System (ITS)

Located in the central region and in close proximity to the beampipe, the Inner Tracking System (ITS)[36, 38] acts as the first interaction point of the thousands of particles produced in each collision. The ITS covers a full 2π in the azimuth and a pseudo-rapidity range of $|\eta| < 0.9$. The primary task of the ITS is to localize the primary vertex V_z of the two colliding nuclei, i.e. the interaction position along the beamline. It consists of three distinct types of Si based detectors stacked radial outwards, each with two layers. The inner layer of the ITS is composed of Silicon Pixel Detectors (SPD) that provide a high track resolution and trigger rate. The SPD covers a radial distance of 3.9 cm $< r <$ 7.6 cm and is built to manage the high particle densities close to the interaction point that is reached in heavy-ion collisions. The second and third layers of the ITS consists of Silicon Drift-Detectors (SDD) and Silicon Strip-Detectors (SSD) respectively and are positioned at 15 cm $< r <$ 43 cm, where particle densities are much lower. The SSD together with the SDD, both have analog-based readout that allows particle identification through energy loss measurements dE/dx.

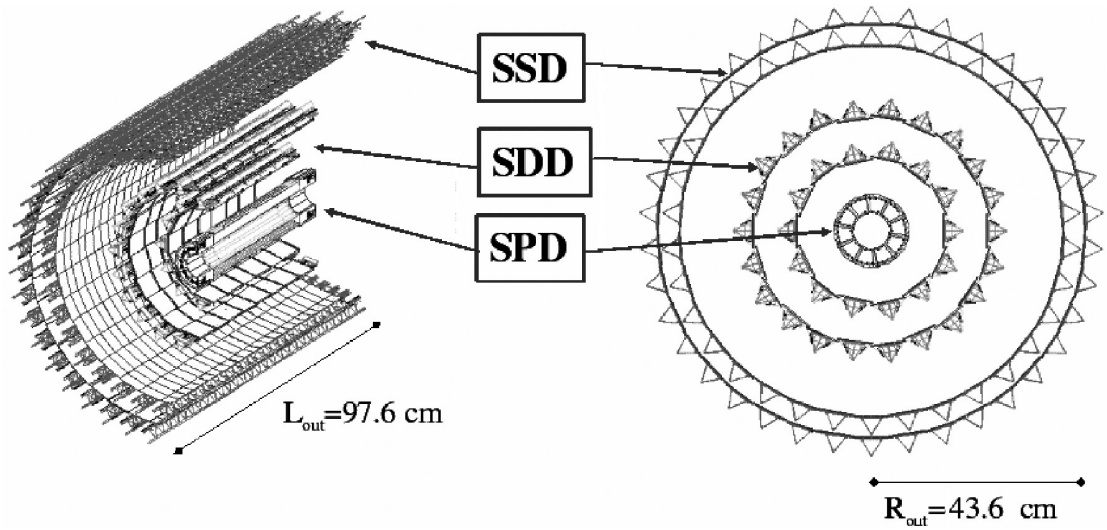

Figure 2.3: Schematic of the ITS, figure taken from [36].

Time Projection Chamber (TPC)

Located in the outer segment of the central barrel is the Time Projection Chamber (TPC) [36, 39] functions as the main detector for tracking, as well as particle identification through energy loss measurement dE/dx. Combined with the ITS this ensures a large tracking range with a high space point resolution. The TPC is a cylindrical chamber covering the ITS with a full 2π in the azimuth, except for some minor dead zones. The pseudo-rapidity coverage is $|\eta| < 0.9$ from where it provides full tracking in the range $\eta| < 0.8$. The detector consists of a large field cage covering a radial distance of 85 cm $< r <$ 250 cm. The active volume (90 m^3) of the cylinders is filled with a gas mixture of $Ne/CO_2/N_2$ (90/10/5). The chamber is divided in half by a central cathode, and an anode, placed on each side of the detector. The potential difference of the anode and cathode creates a potential field difference the particle can move, and be moved in The working principle of the TPC is as follows: As charged particles propagate through the detector, the gas mixture is ionized alongside its path. The free electron sequentially drifts towards the end plate where read-out chambers are placed, and the transferred energy is converted to an analog signal that can be used to track direction and energy.

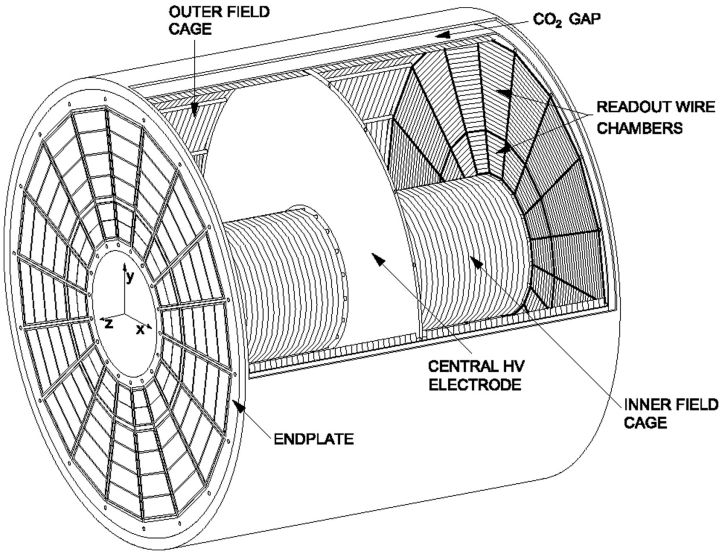

Figure 2.4: Schematic of the TPC, figure taken from [39]

VZERO Detector (V0)

The VZERO detector[36, 40] consists of two scintillator arrays, named V0C and V0A, positioned at the forward and backward region of the interaction point. The arrays cover a pseudo-rapidity range of V0C ($-3.7 < \eta < -1.7$) and V0A ($2.8 < \eta < 5.1$) and each consists of 32 scintillator counters that are distributed across four rings in a radial direction, covering 2π in the azimuthal angle. The VZERO detector has several use cases but primarily functions as a minimum bias (MB) trigger for the central barrel detector in pp and AA collisions and an additional centrality-specific trigger for AA collision only. Besides given trigger signals, the VZERO also provides measurements of charged particle multiplicity $dN_{CH}/d\eta$ that is used for classifying the centrality of a given AA collision.

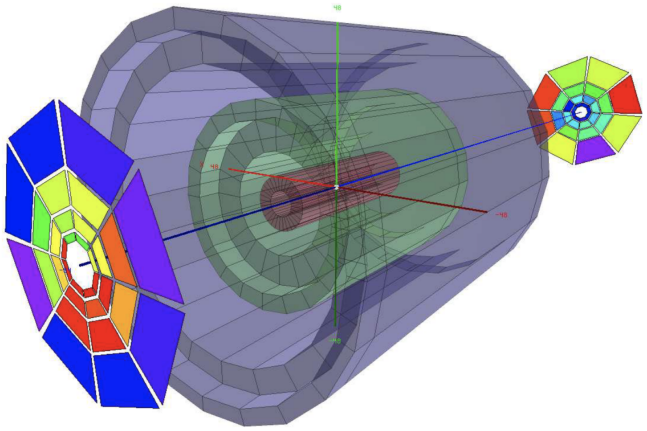

Figure 2.5: V0A and V0C segments positioned at the forward and backward region of the interaction point. The figure is taken from[41].

2.3 Centrality

Observables in AA collision are dependent on geometrical quantities such as the plane of interaction and are therefore needed to properly study different forms of physics, in ultra-relativistic collisions. Such a quantity can be the transverse distance between two colliding nuclei which is denoted as the impact parameter b. These quantities are though not directly accessible in experiments and other estimators are needed to precisely classify events. Instead, collisions are classified and measured with respect to centrality. The experimental centrality c_{exp} of an event is an approximate estimator of the fully measured visible cross-section of an observable[42]

$$c_{\text{exp}} = \frac{1}{\sigma_{\text{vis}}} \int_X^\infty \mathrm{d}X \frac{\mathrm{d}\sigma_{\text{vis}}}{\mathrm{dX}'} = \frac{1}{N} \int_X^\infty \mathrm{d}X' \frac{\mathrm{d}N}{\mathrm{d}X'}$$

In the context of heavy ion experiments, the centrality is often calculated on the basis of observed charged particle multiplicity such that $X = N_{ch}$. With this, we can classify events according to *central* collision, low impact parameter b, or as *peripheral* collisions with high impact parameter b. Intuitively, a low impact parameter would mean a head-on collision, which consequently would result in more particles produced. Likewise, a large impact parameter would result in few particles produced. The relation between multiplicity and centrality can be seen in Figure 2.6. This not only allows for a nice and intuitive representation but also ensures that all data are distributed uniformly. Thus it becomes easier to notice the statistical sensitivity of measurements in different ranges. Centrality calculations based on multiplicities are a very often complex process that requires additional fitting [43] and are therefore left for the experts[8].

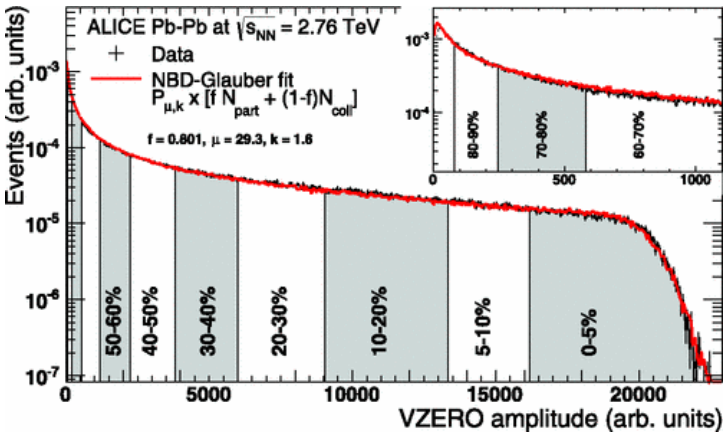

Figure 2.6: Figure of the charged particle multiplicity and corresponding centrality class of Pb-Pb collision at $\sqrt{s_{NN}} = 2.76$ TeV. The black points represent data, and the fitted line shows the Glauberfit. Figure taken from [43]

[8] Though, an impact parameter-based estimator for centrality is calculated and presented under Appendix D which is used for centrality estimation in the local deformation study.

3 Analysis method

The direct correlation of mean transverse momentum and the area of interaction in Equation 1.1 gives rise to additional information that can be extracted in the early phase of the collision. With an overlap region in the transverse plane $R_\perp$ denoting the average area of participating nucleons it is by definition directly related to the nucleon density $d_\perp$. The fluctuation of transverse momentum has been shown to exhibit a significant response to both pre-equilibrium dynamics and the following hydrodynamic evolution of the bulk media through[24]

$$\frac{\delta\langle p_T\rangle}{\langle p_T\rangle} = k_0\frac{\delta d_\perp}{d_\perp} = -k_0\frac{\delta R_\perp}{R_\perp} = -k_0\frac{1}{2}\frac{\delta S_\perp}{S_\perp} \tag{3.1}$$

where $S_\perp$ denotes the transverse entropy density respectively and k_0 is coefficient regarding the transport properties of the QGP. Consequently, as the area of the interacting system is reduced, the pressure gradient from participating nucleon will rise and increase the "explosion" of the QGP fireball. The experimental methods centering around the fluctuations are of increased interest as they can contribute to the exploration of initial conditions in heavy-ion collisions, and thus help to refine our understanding of the nuclear structure and strong interactions [12, 44]. In the following chapter, the basic definitions of intrinsic moments, cumulants, and multi-particle correlation are discussed together with application, properties, and physical relation to energy fluctuations in heavy-ion collisions. As this is all re-derived from previous work, this constitutes a mostly historical and conceptual understanding of the basic theory. Sequently new observable probes will be presented for the first time in the form of a generic formula that generalizes the method of standardized cumulants of transverses momentum fluctuation to arbitrary orders. The new probes will provide never seen "snapshots" of the initial stage in ultra-relativistic heavy-ion collisions, unraveling the nuclear structure and composition at the moment of impact. The chapter will continue with the exploration of applied suppression techniques for non-collective behaviour[9], known as the sub-event method. This will be presented together with its integration into the generic formulas.

3.1 Multi-particle correlation

For any m particles observed, their joint density function f_m can be decomposed into a series of symmetric function g_m known as *correlation function*[45, 46]. The expansion of the distribution function is defined as all partitions of g_m that can be formed from the m particles and are to third order decomposed as follows

$$\begin{aligned} f_1(x_1) =& g_1(x_1) \\ f_2(x_1,x_2) =& g_1(x_1)g_1(x_2) + g_2(x_1,x_2) \\ f_3(x_1,x_2,x_3) =& g_1(x_1)g_1(x_2)g_1(x_3) + g_2(x_1,x_2)g_1(x_3) \\ &+ g_2(x_1,x_3)g_1(x_2) + g_2(x_2,x_3)g_1(x_1) + g_2(x_1,x_2,x_3) \end{aligned} \tag{3.2}$$

Here an illustration of the three-particle distribution function can be seen in Figure 3.1, where the last term would denote the *genuine* correlation of the three particles.

Figure 3.1: Illustration of the three-particle distribution and its corresponding decomposition into symmetric correlation functions g_m

[9] non-collective behaviors are effects that do not originate from the initial QGP phase, which consequently bias the measurements by shielding the observables in a background noise

It is clear that even though the distribution function f_m contains the complete information about the system, it is challenging to directly distinguish between *correlated* and *uncorrelated* contributions from each g_m. The correlation functions are themselves non-trivial and are typically inaccessible in experiments since the correlation reflects an unknown nature. On the other hand, f_m can be directly related to a physical equation or problem[41, 46]. To obtain a direct measurement of the genuine m-particle correlation g_m it can therefore be advantageous to express g_m in terms of f_m. By substituting the one-particle distribution functions f_1 in Eq. 3.2 and isolating for g_2 we can obtain an expression for the genuine 2-particle correlation.

$$g_2(x_1, x_2) = f_2(x_1, x_2) - f_1(x_1)f_1(x_2)$$

The genuine correlation of m particles g_m is also more historically known and referred to as the m'th order cumulant which will also be the formal name in this thesis. Though it can also be noted that the second-order cumulant constitutes the covariance of two observables. In the case of independent random variables, we further note $g_2 = 0$ such that the joint density f_2 can be factorized as a product of marginalized density functions.

$$f_2(x_1, x_2) = f_1(x_1)f_1(x_2)$$

Cumulants in heavy-ion experiments

Consequently, this also implies that the correlation function $g_m \to 0$ in the case of independent random variables, is the key property of interest. In reality, we have no way of experimentally accessing the correlation function but we can estimate key properties of the joint distribution by sampling from an appropriate ensemble of events.

$$\mathbb{E}_g\left[x_1 x_2\right] = \mathbb{E}_f\left[x_1 x_2\right] - \mathbb{E}_f\left[x_1\right]\mathbb{E}_f\left[x_2\right]$$

An unbiased estimator for $\mathbb{E}_f\left[x_1 x_2\right]$ is taken as the all-event average of all pair-wise combinations of the observables x_1 and x_2[41]. Letting $x_1 \equiv p_T^{(i_1)}$ and $x_2 \equiv p_T^{(i_2)}$ we can obtain the expression for the second-order cumulants of transverse momentum correlation.

$$\mathbb{E}_g\left[p_T^{(i_1)} p_T^{(i_2)}\right] = \mathbb{E}_f\left[p_T^{(i_1)} p_T^{(i_1)}\right] - \mathbb{E}_f\left[p_T^{(i_1)}\right]\mathbb{E}_f\left[p_T^{(i_2)}\right]$$

For a more proper and generic notation, we will denote the general m-order cumulant of transverse momentum correlation as follows

$$\kappa(p_T'^m) \equiv \mathbb{E}_g\left[p_T^{(i_1)} \cdots p_T^{(i_m)}\right] \tag{3.3}$$

3.1.1 Intrinsic moments

The isolation of transverse momentum fluctuations is in itself a very complicated procedure as we are dealing with a PDF defined only by the measured p_T. Consequently, any properties have to be extracted from this one variable. To accommodate for this, high-energy experiments such as RHIC and the ALICE have been utilizing the method of multi-particle correlation to obtain anisotropies in the final state distribution of the azimuthal angle φ[47, 48]. In this approach, an event averaged estimate is calculated by combining every possible, and unique, m-particle tuple to form a m-*particle intrinsic moment*. Sequently the method of cumulants as described in the chapter Multi-particle correlation are used to isolate the *genuine* correlation, and thus reveal if the particle distribution is random or correlated in nature.

The intrinsic moments are firstly calculated by looping over all charged particle tuples in a single event. The single event average (or particle average) which will be denoted by an angular

bracket $\langle\cdot\rangle$. The moments are sequentially calculated for a sufficiently large number of events from where the all-event averaged moments are obtained. The all-event average will be denoted by a double angular bracket $\langle\langle\cdot\rangle\rangle$. The first step involves calculating the single-event moments with the first, second, and third order being defined by

$$\langle p_T'^1\rangle \equiv \langle p_T'^1\rangle \equiv \frac{1}{\mathrm{W}_{N_{ch},1}} \sum_{i_1} p_T^{(i_1)} \tag{3.4}$$

$$\langle p_T'^2\rangle \equiv \langle p_T^{(i_1)} p_T^{(i_2)}\rangle \equiv \frac{1}{\mathrm{W}_{N_{ch},2}} \sum_{i_1\neq i_2} p_T^{(i_1)} p_T^{(i_2)} \tag{3.5}$$

$$\langle p_T'^3\rangle \equiv \langle p_T^{(i_1)} p_T^{(i_2)} p_T^{(i_3)}\rangle \equiv \frac{1}{\mathrm{W}_{N_{ch},3}} \sum_{i_1\neq i_2\neq i_3} p_T^{(i_1)} p_T^{(i_2)} p_T^{(i_3)} \tag{3.6}$$

where the sum runs over all momentum tuples under the constraint $i_1 \neq i_2 \neq i_3$ which mean that all indices must be taken differently. Each sum is additionally weighted by a factor $\mathrm{W}_{N_{ch},m}$ which accounts for each distinct number of m-particle combinations in the event with multiplicity N_{ch}. The weight is appropriately defined as[41, 44, 49] and accounts for multiplicity fluctuation between different events by construction

$$\mathrm{W}_{N_{ch},m} = N_{ch}(N_{ch}-1)\cdots(N_{ch}-m+1) \tag{3.7}$$

In the second step, the moments averaged over all events are calculated as

$$\langle\langle p_T'^1\rangle\rangle \equiv \frac{\sum_{i=1}^{event} W_{N_{ch},1}^{(i)} \langle p_T'^1\rangle_i}{\sum_{i=1}^{event} W_{N_{ch},1}^{(i)}} \tag{3.8}$$

$$\langle\langle p_T'^2\rangle\rangle \equiv \frac{\sum_{i=1}^{event} W_{N_{ch},2}^{(i)} \langle p_T'^2\rangle_i}{\sum_{i=1}^{event} W_{N_{ch},2}^{(i)}} \tag{3.9}$$

$$\langle\langle p_T'^3\rangle\rangle \equiv \frac{\sum_{i=1}^{event} W_{N_{ch},3}^{(i)} \langle p_T'^3\rangle_i}{\sum_{i=1}^{event} W_{N_{ch},3}^{(i)}} \tag{3.10}$$

where $W_{N_{ch},m}^{(i)}$ and $\langle p_T'^m\rangle_i$ are the associated multiplicity weight and intrinsic moment in event number i respectively. As can be seen by the outlined Equation 3.4-3.10 the formulas are quite easily generalized to arbitrary high orders for both the particle-average and the event-averaged intrinsic moments as given by

$$\langle p_T'^m\rangle \equiv \langle p_T^{(i_1)} p_T^{(i_2)} \cdots p_T^{(i_m)}\rangle \equiv \frac{1}{\mathrm{W}_{N_{ch},m}} \sum_{i_1\neq i_2} p_T^{(i_1)} p_T^{(i_2)} \cdots p_T^{(i_m)} \tag{3.11}$$

$$\langle\langle p_T'^m\rangle\rangle \equiv \frac{\sum_{i=1}^{event} W_{M,m}^{(i)} \langle p_T'^m\rangle_i}{\sum_{i=1}^{event} W_{M,m}^{(i)}} \tag{3.12}$$

Though, while the concept of intrinsic moments in general has a simple expression they are difficult to obtain in practice. This is solely due to the constraint of unique pairs which in general have to be carried out in a nested loop over all particles used. Consequently, the calculation reaches a time complexity of approximately $O(N_{ch}^m)$ which is impossible in heavy-ion collisions with event multiplicities reaching up to $N_{ch} \approx 8000$. To account for the difficulties in carrying out the calculation in practice, a dedicated section will be provided for an efficient method as applied in this thesis and in general heavy-ion experiments.

Momentum vector formulation

To account for the computational dependent task of obtaining the moments, the QCumulant method where introduced[50] as an efficient way of isolating *genuine* particle pairs in anisotropic flow analysis. The method relies on a clever expansion of the multi-variable constrained sum (see Equation 3.11) into a set of independent sums, which would then only require a single pass over the data. Following the procedure[49, 50] we define our momentum vector P_k as the sum of particle momentum $p_T^{(i_j)}$ for all N_{ch} particles in a event as

$$P_k \equiv \sum_{j=1}^{N_{ch}} \left(p_T^{(i_j)}\right)^k \tag{3.13}$$

where k denotes some arbitrary exponent which will be defined later. For two particle moments we can decompose our constrained sum $\sum_{i_1 \neq i_2}$ into following terms

$$\sum_{i_1 \neq i_2} p_T^{(i_1)} p_T^{(i_2)} = \left(\sum_{i_1} p_T^{(i_1)}\right)\left(\sum_{i_2} p_T^{(i_2)}\right) - \sum_{i_1 = i_2} \left(p_T^{(i_1)}\right)^2 = P_1^2 - P_2$$

where we in the last step have substituted the momentum vector definition(Equation 3.13). As noted the decomposition into independent sums only requires a single loop over data and effectively reduces the time complexity. Using the obtained expression we can redefine our two-particle moments into a more accessible form in computational calculations

$$\langle p_T'^2 \rangle = \frac{1}{W_{Nch,2}} \sum_{i_1 \neq i_2} p_T^{(i_1)} p_T^{(i_2)} = \frac{1}{W_{Nch,2}} \left[P_1^2 - P_2\right]$$

For a more clear validation of the momentum vector formulation, we consider a simple example with a slightly more detailed proof of concept for the intrinsic moment, again with second order $\langle p_T'^2 \rangle$ as an example. Consider an event with a very small multiplicity $N_{ch} = 3$ we observe three particles with momentum denoted $p_T^{(i_1)}$,$p_T^{(i_2)}$,$p_T^{(i_3)}$ where i_n denotes the n'th particle. Following Equation 3.13 we loop over our three particles and construct our momentum vectors as

$$P_1 = p_T^{(i_1)} + p_T^{(i_2)} + p_T^{(i_3)} \qquad P_2 = \left(p_T^{(i_1)}\right)^2 + \left(p_T^{(i_2)}\right)^2 + \left(p_T^{(i_3)}\right)^2$$

Inserting our momentum "vectors" we get

$$\begin{aligned}
\langle p_T'^2 \rangle &= \frac{P_1^2 - P_2}{W_{N_{ch},2}} \\
&= \frac{\left(p_T^{(i_1)} + p_T^{(i_2)} + p_T^{(i_3)}\right)^2 - \left(p_T^{(i_1)}\right)^2 - \left(p_T^{(i_2)}\right)^2 - \left(p_T^{(i_3)}\right)^2}{N_{ch}(N_{ch}-1)} \\
&= \frac{\left(p_T^{(i_1)}\right)^2 + \left(p_T^{(i_2)}\right)^2 + \left(p_T^{(i_3)}\right)^2 + 2p_T^{(i_1)}p_T^{(i_2)} + 2p_T^{(i_1)}p_T^{(i_3)} + 2p_T^{(i_2)}p_T^{(i_3)} - \left(p_T^{(i_1)}\right)^2 - \left(p_T^{(i_2)}\right)^2 - \left(p_T^{(i_3)}\right)^2}{N_{ch}(N_{ch}-1)} \\
&= \frac{1}{N_{ch}(N_{ch}-1)}\left[2p_T^{(i_1)}p_T^{(i_2)} + 2p_T^{(i_1)}p_T^{(i_3)} + 2p_T^{(i_2)}p_T^{(i_3)}\right] \\
&= \frac{1}{3\cdot 2}\left[2p_T^{(i_1)}p_T^{(i_2)} + 2p_T^{(i_1)}p_T^{(i_3)} + 2p_T^{(i_2)}p_T^{(i_3)}\right] \\
&= \frac{1}{3}\left[p_T^{(i_1)}p_T^{(i_2)} + p_T^{(i_1)}p_T^{(i_3)} + p_T^{(i_2)}p_T^{(i_3)}\right]
\end{aligned}$$

In the analytical decomposition, it is clear how the method provides quick and efficient separation of particle pairs. Even though the expansion can be carried out to arbitrary orders, it does require an analytical derivation for all terms, which can be far from trivial. Up to the third order, the explicit formulas for direct calculation are obtained as

$$\begin{aligned}
\langle p_T'^1 \rangle &= \frac{P_1}{N_{ch}} \\
\langle p_T'^2 \rangle &= \frac{P_1^2 - P_2}{N_{ch}(N_{ch}-1)} \\
\langle p_T'^3 \rangle &= \frac{P_1^3 - 3P_2P_1 + 2P_3}{N_{ch}(N_{ch}-2)(N_{ch}-1)}
\end{aligned}$$

For higher orders moments a generic formula will be presented in the following section, which effectively reduces the expansion of arbitrary orders into a simple and accessible equation.

3.2 Generic formula

With the more formal definitions in place, we now introduced the generic formula for calculating intrinsic moments of transverse momentum which will provide the baseline for our main cumulants observables. The generic formula for a weighted average between all unique m-particle combinations is given by the definition

$$\langle p_T'^m \rangle \equiv \frac{\sum_{i_1 \neq \cdots \neq i_m}^{N_{ch}} w_{i_1} w_{i_2} \cdots w_{i_m} p_T^{(i_1)} p_T^{(i_2)} \cdots p_T^{(i_m)}}{\sum_{i_1 \neq i_2 \neq \cdots \neq i_m}^{N_{ch}} w_{i_1} w_{i_2} \cdots w_{i_m}} \tag{3.14}$$

where N_{ch} is the charged particle multiplicity in a given event, p_T labels the transverse momentum and w labels the associated weight. In contrast to the multiplicity weights defined in Equation 3.7, the weight w is associated with the p_T, and can thus be used to reduce systematic effects such as detector efficiency. The weights can in general be a function of any desirable properties of the particle track $w(p_T, \eta, \phi, \ldots)$, but will in this thesis be restricted to $w(p_T)$. As can be seen from Equation 3.14 the numerator and denominator are affected by the constrained sum. To reduce calculation the derivation will only concern to the numerator. The same principle can afterward be applied to the denominator. Decomposing our generic definition

in Equation 3.14 we outlined the reduced expressions

$$N\langle p_T'^m\rangle \equiv \sum_{i_1\neq\cdots\neq i_m}^{N_{ch}} w_{i_1}w_{i_2}\cdots w_{i_m}p_T^{(i_1)}p_T^{(i_2)}\cdots p_T^{(i_m)} \tag{3.15}$$

$$D\langle p_T'^m\rangle \equiv \sum_{i_1\neq i_2\neq\cdots\neq i_m}^{N_{ch}} w_{i_1}w_{i_2}\cdots w_{i_m} \tag{3.16}$$

With the above equation outlined, we introduce a redefined momentum vector P_k and add an associated weight vector W_k which will be used in reducing the formula.

$$P_k \equiv \sum_{i=1}^{M}\left(w_i p_T^{(i)}\right)^k, \qquad W_k \equiv \sum_{i=1}^{M} w_i^k \tag{3.17}$$

In the development of a generic framework for anisotropic flow analysis[51], it was noted how the innermost sum could be expanded without the constraints of other particles. Following the same principle we take Equation 3.15

$$N\langle p_T'^m\rangle = \sum_{i_1\neq\cdots\neq i_m}^{N_{ch}} w_{i_1}w_{i_2}\cdots w_{i_m}p_T^{(i_1)}p_T^{(i_2)}\cdots p_T^{(i_m)}$$

expanding the innermost sum accordingly[51] we get

$$= \sum_{i_1\neq\cdots\neq i_{m-1}}^{N_{ch}} w_{i_1}w_{i_2}\cdots w_{i_{m-1}}p_T^{(i_1)}p_T^{(i_2)}\cdots p_T^{(i_{m-1})}\cdot\left(\sum_{i_m=1}^{N_{ch}} w_{i_m}p_T^{(i_m)} - \sum_{j=1}^{m-1} w_{i_j}p_T^{(i_j)}\right)$$

contracting the constrained sum we obtain an expression as Equation 3.15, but with the order reduced by óne

$$= N\langle p_T'^{m-1}\rangle\left(\sum_{i_m=1}^{N_{ch}} w_{i_m}p_T^{(i_m)} - \sum_{j=1}^{m-1} w_{i_j}p_T^{(i_j)}\right)$$

using our momentum vector in Equation 3.17 the first sum in the parentheses can be written as

$$= N\langle p_T'^{m-1}\rangle\left(P_1 - \sum_{j=1}^{m-1} w_{i_j}p_T^{(i_j)}\right)$$

The summation can thus be expanded into lower-order terms by a recursive iteration. Following the expansion through for $m = 2$ we can quickly obtain an expression for the two-particle moments. Additionally, applying the same principle to Equation 3.16 we get

$$N\langle p_T'^2\rangle = P_1^2 - P_2$$
$$D\langle p_T'^2\rangle = W_1^2 - W_2$$

and for the three-particle moment, we have

$$N\langle p_T'^3\rangle = P_1^3 - 3P_2P_1 + 2P_3$$
$$D\langle p_T'^3\rangle = W_1^3 - 3W_2W_1 + 2W_3$$

We note from the direct expansion (and also by the generic formula) that the $k^{'}$ iterated term changes sign according to $(-1)^{k-1}$. Additionally, each term picks up a factor of $(m-k)$. Taking

these term contributions into account, the explicit formulas for isolating particle pairs and hence calculating intrinsic moment to arbitrary orders are given by these generic formulas

$$N\langle p_T'^m\rangle = \sum_{k=1}^{m}(-1)^{k-1}\frac{(m-1)!}{(m-k)!}N\langle p_T'^{m-k}\rangle P_k \tag{3.18}$$

$$D\langle p_T'^m\rangle = \sum_{k=1}^{m}(-1)^{k-1}\frac{(m-1)!}{(m-k)!}D\langle p_T'^{m-k}\rangle W_k \tag{3.19}$$

$$\langle p_T'^m\rangle = \frac{N\langle p_T'^m\rangle}{D\langle p_T'^m\rangle} \tag{3.20}$$

3.3 Transverse momentum fluctuations

Observation of mean transverse momentum fluctuation where measured by the STAR collaboration[52] and has sequentially fallen under the microscope for additional studies[44, 53]. Though all presented data can be attributed directly to some aspect of IC and hydrodynamic expansion, there is no direct road to take so far. Consequently, the direct formulation of p_T fluctuations can vary depending on experiments but are in general defined as central moment[44, 53]. As outlined in the previous section, the generic formula for intrinsic moments represents an alternative to regular moments. While lower order cumulants $\kappa(p_T'^2)$ and $\kappa(p_T'^3)$ are the same whether calculated as central moment or regular moment. Higher order cumulants $\kappa(p_T'^m)$ for $4 \leq m$ do not possess this property by default so a clear deviation is expected if compared. Throughout this thesis, the cumulants obtained will be through regular moments as already presented.

3.3.1 Cumulants

The transverse momentum fluctuations measured in experiments can delicately be expressed in terms of cumulants which reflect genuine correlation amongst particles. The method of azimuthal correlation has for decades relied on flow measurements through cumulant expansions[41, 46, 47, 49, 50, 54, 55] and it should therefore be enough to stick with a brief outline of the approach. The method for obtaining cumulants where first introduced in terms of cluster expansion [45, 56] as presented at the beginning of this chapter. Sequently a recursive formula has been derived [57] to obtain cumulants by an expansion of the moment-generating function. Using the same approach we can directly obtain our cumulants, and hence then genuine correlation, by switching to our intrinsic moments. This will effectively make it possible to easily and efficiently isolate the genuine correlation. With a more proper notation, we then present the generic formula for cumulants of transverse momentum fluctuation.

$$\kappa(p_T'^m) = \langle\langle p_T'^m\rangle\rangle - \sum_{k=1}^{m-1}\binom{m-1}{k-1}\kappa(p_T'^k)\langle\langle p_T'^{m-k}\rangle\rangle \tag{3.21}$$

where $\kappa(p_T'^m)$ and $\langle\langle p_T'^m\rangle\rangle$ are the $m\,'$th cumulant and event averaged moment respectively. The calculation of higher-order cumulants consequently becomes more complex in structure as all lower-order contribution has to be removed. By direct expansion of Equation 3.21 we list present the first eight orders of transverse momentum fluctuations in terms of intrinsic moments.

$$\langle p_T\rangle = \langle\langle p_T'^1\rangle\rangle \tag{3.22}$$

$$\kappa(p_T'^2) = \langle\langle p_T'^2\rangle\rangle - \langle\langle p_T'^1\rangle\rangle^2 \tag{3.23}$$

$$\kappa(p_T'^3) = \langle\langle p_T'^3\rangle\rangle - 3\langle\langle p_T'^1\rangle\rangle\langle\langle p_T'^2\rangle\rangle + 2\langle\langle p_T'^1\rangle\rangle^3 \tag{3.24}$$

$$\kappa(p_T'^4) = \langle\langle p_T'^4\rangle\rangle - 3\langle\langle p_T'^2\rangle\rangle^2 - 4\langle\langle p_T'^1\rangle\rangle\langle\langle p_T'^3\rangle\rangle + 12\langle\langle p_T'^1\rangle\rangle^2\langle\langle p_T'^2\rangle\rangle - 6\langle\langle p_T'^1\rangle\rangle^4 \tag{3.25}$$

$$\kappa(p_T'^5) = \langle\langle p_T'^5\rangle\rangle - 5\langle\langle p_T'^1\rangle\rangle\langle\langle p_T'^4\rangle\rangle - 10\langle\langle p_T'^2\rangle\rangle\langle\langle p_T'^3\rangle\rangle + 20\langle\langle p_T'^1\rangle\rangle^2\langle\langle p_T'^3\rangle\rangle + 30\langle\langle p_T'^1\rangle\rangle\langle\langle p_T'^2\rangle\rangle^2 - 60\langle\langle p_T'^1\rangle\rangle^3\langle\langle p_T'^2\rangle\rangle + 24\langle\langle p_T'^1\rangle\rangle^5 \quad 3.26$$

$$\kappa(p_T'^6) = \langle\langle p_T'^6\rangle\rangle - 6\langle\langle p_T'^1\rangle\rangle\langle\langle p_T'^5\rangle\rangle - 10\langle\langle p_T'^3\rangle\rangle^2 - 15\langle\langle p_T'^2\rangle\rangle\langle\langle p_T'^4\rangle\rangle + 30\langle\langle p_T'^2\rangle\rangle^3 + 30\langle\langle p_T'^1\rangle\rangle^2\langle\langle p_T'^4\rangle\rangle - 120\langle\langle p_T'^1\rangle\rangle^3\langle\langle p_T'^3\rangle\rangle + 120\langle\langle p_T'^1\rangle\rangle\langle\langle p_T'^2\rangle\rangle\langle\langle p_T'^3\rangle\rangle - 270\langle\langle p_T'^1\rangle\rangle^2\langle\langle p_T'^2\rangle\rangle^2 + 360\langle\langle p_T'^1\rangle\rangle^4\langle\langle p_T'^2\rangle\rangle - 120\langle\langle p_T'^1\rangle\rangle^6 \quad 3.27$$

$$\kappa(p_T'^7) = \langle\langle p_T'^7\rangle\rangle - 7\langle\langle p_T'^1\rangle\rangle\langle\langle p_T'^6\rangle\rangle - 21\langle\langle p_T'^2\rangle\rangle\langle\langle p_T'^5\rangle\rangle - 35\langle\langle p_T'^3\rangle\rangle\langle\langle p_T'^4\rangle\rangle + 42\langle\langle p_T'^1\rangle\rangle^2\langle\langle p_T'^5\rangle\rangle + 140\langle\langle p_T'^1\rangle\rangle\langle\langle p_T'^3\rangle\rangle^2 - 210\langle\langle p_T'^1\rangle\rangle^3\langle\langle p_T'^4\rangle\rangle + 210\langle\langle p_T'^2\rangle\rangle^2\langle\langle p_T'^3\rangle\rangle + 210\langle\langle p_T'^1\rangle\rangle\langle\langle p_T'^2\rangle\rangle\langle\langle p_T'^4\rangle\rangle - 630\langle\langle p_T'^1\rangle\rangle\langle\langle p_T'^2\rangle\rangle^3 + 840\langle\langle p_T'^1\rangle\rangle^4\langle\langle p_T'^3\rangle\rangle - 1260\langle\langle p_T'^1\rangle\rangle^2\langle\langle p_T'^2\rangle\rangle\langle\langle p_T'^3\rangle\rangle - 2520\langle\langle p_T'^1\rangle\rangle^5\langle\langle p_T'^2\rangle\rangle + 2520\langle\langle p_T'^1\rangle\rangle^3\langle\langle p_T'^2\rangle\rangle^2 + 720\langle\langle p_T'^1\rangle\rangle^7 \quad 3.28$$

$$\kappa(p_T'^8) = \langle\langle p_T'^8\rangle\rangle + 20160\langle\langle p_T'^1\rangle\rangle^6\langle\langle p_T'^2\rangle\rangle - 6720\langle\langle p_T'^1\rangle\rangle^5\langle\langle p_T'^3\rangle\rangle - 25200\langle\langle p_T'^1\rangle\rangle^4\langle\langle p_T'^2\rangle\rangle^2 + 1680\langle\langle p_T'^1\rangle\rangle^4\langle\langle p_T'^4\rangle\rangle + 13440\langle\langle p_T'^1\rangle\rangle^3\langle\langle p_T'^2\rangle\rangle\langle\langle p_T'^3\rangle\rangle - 336\langle\langle p_T'^1\rangle\rangle^3\langle\langle p_T'^5\rangle\rangle + 10080\langle\langle p_T'^1\rangle\rangle^2\langle\langle p_T'^2\rangle\rangle^3 - 2520\langle\langle p_T'^1\rangle\rangle^2\langle\langle p_T'^2\rangle\rangle\langle\langle p_T'^4\rangle\rangle - 1680\langle\langle p_T'^1\rangle\rangle^2\langle\langle p_T'^3\rangle\rangle^2 + 56\langle\langle p_T'^1\rangle\rangle^2\langle\langle p_T'^6\rangle\rangle - 5040\langle\langle p_T'^1\rangle\rangle\langle\langle p_T'^2\rangle\rangle^2\langle\langle p_T'^3\rangle\rangle + 336\langle\langle p_T'^1\rangle\rangle\langle\langle p_T'^2\rangle\rangle\langle\langle p_T'^5\rangle\rangle + 560\langle\langle p_T'^1\rangle\rangle\langle\langle p_T'^3\rangle\rangle\langle\langle p_T'^4\rangle\rangle - 8\langle\langle p_T'^1\rangle\rangle\langle\langle p_T'^7\rangle\rangle - 630\langle\langle p_T'^2\rangle\rangle^4 + 420\langle\langle p_T'^2\rangle\rangle^2\langle\langle p_T'^4\rangle\rangle + 560\langle\langle p_T'^2\rangle\rangle\langle\langle p_T'^3\rangle\rangle^2 - 28\langle\langle p_T'^2\rangle\rangle\langle\langle p_T'^6\rangle\rangle - 56\langle\langle p_T'^3\rangle\rangle\langle\langle p_T'^5\rangle\rangle - 35\langle\langle p_T'^4\rangle\rangle^2 - 5040\langle\langle p_T'^1\rangle\rangle^8 \quad 3.29$$

The measurements of cumulants can additionally be contaminated by non-collective effects. These are false correlation signals that can arise from the jet and the decay of particles. For this reason, it can be advantageous to use the higher order cumulants as the possibility of m particles being correlated by other measures then the collective expansion is on the order $\approx 1/(N_{ch})^{m-1}$ [41]. If the particles evolve from a collective expansion, as from QGP the particles would be correlated in some manor, regardless of how many are taken into account. While they might not always be accessible in real data due to statistical limitations, they can provide a great method for obtaining possible saturation effects when going to higher orders.

3.3.2 Standerdized cumulants

As the cumulants are very sensitive to analysis details, such as the measured p_T, collision system, and collision energy[44], additional steps are made to assure a more robust observable in where systematic effects are canceled. Additionally, it has been found that the application of weights as introduced in Equation 3.19 results in a non-linear response, which consequently causes failure of any closure tests[10]. To account for these effects we introduce *scaled* cumulants which reduce the observables to dimensionless quantities. Some experiments scale the cumulants by the mean measured transverse momentum $1/\langle\langle p_T'^1\rangle\rangle$ for a simple system comparisons[53] while other experiments scale the cumulants with respect to some of the global parameter[11], and are denoted as intensive ratios[44]. The intensive ratios are constructed to reduce global fluctuations. The scaling is therefore not strictly defined and differs in between experiments due to different motivations. Consequently, direct comparisons of results are not always possible. In this thesis, we provide a standardized baseline for the cumulant scaling. Following the same method of standardized moments with respect to the square root of the variance we get

$$\tilde{\mu}_m = \frac{\mu_m}{\sigma^m} = \frac{\mathrm{E}\left[(X-\mu)^m\right]}{\left(\mathrm{E}\left[(X-\mu)^2\right]\right)^{m/2}} \quad \longrightarrow \quad \widetilde{\kappa}(p_T'^m) = \frac{\kappa(p_T'^m)}{\sqrt{(\kappa(p_T'^2))^m}} \quad 3.30$$

where $\kappa(p_T'^m)$ are the m´th order cumualants as obtained through Equation 3.22-3.27. As a result of the choice of scaling, the standardized cumulant is not defined for second order $m = 2$

[10] This research has mostly been discussed in internal ALICE meetings and analysis notes

[11] this is regarded as a common correlated variable in the analysis range, such as multiplicity or centrality as used in this thesis

as can be directly noted by the formulation in Equation 3.30. The complete formulas for up to eight orders $m = 8$ are provided below.

$$\widetilde{\kappa}(p_T'^1) = \frac{\langle\langle p_T'^1 \rangle\rangle}{\sqrt{(\kappa(p_T'^2))^1}}, \quad \widetilde{\kappa}(p_T'^3) = \frac{\kappa(p_T'^3)}{\sqrt{(\kappa(p_T'^2))^3}}, \quad \widetilde{\kappa}(p_T'^4) = \frac{\kappa(p_T'^4)}{\sqrt{(\kappa(p_T'^2))^4}}, \quad \widetilde{\kappa}(p_T'^5) = \frac{\kappa(p_T'^5)}{\sqrt{(\kappa(p_T'^2))^5}} \tag{3.31}$$

$$\widetilde{\kappa}(p_T'^6) = \frac{\kappa(p_T'^6)}{\sqrt{(\kappa(p_T'^2))^6}}, \quad \widetilde{\kappa}(p_T'^7) = \frac{\kappa(p_T'^7)}{\sqrt{(\kappa(p_T'^2))^7}}, \quad \widetilde{\kappa}(p_T'^8) = \frac{\kappa(p_T'^8)}{\sqrt{(\kappa(p_T'^2))^8}} \tag{3.32}$$

The standardized cumulants for $3 \leq m$ are thus providing a scale-invariant probe that only contains the collective p_T fluctuations of the system. While the second-order cumulants are not directly defined, the first-order standardized cumulant $\widetilde{\kappa}(p_T'^1)$ can be used to indirectly access $\widetilde{\kappa}(p_T'^2)$ information, in the same dimensionless base as the other observables.

3.4 Sub-event method

Measurements of transverse momentum fluctuation are in general contaminated by different sources which are not necessarily part of the initial system which are studied. The non-collective effects might arise due to a number of reasons but primarily arises from back-to-back decays of particles and jets in energetic events. In the presentation of cumulants, it where presented how higher orders are expected to suppress non-collective contribution and provide a more trustworthy measurement. Though, as will also be noted later, the statistical dependence of cumulants scales exponentially. Consequently, this motivates improved methods for low-order cumulants, such that the non-collective effect undergoes additional suppression. In the following section, the method is presented with illustrations and explanations.

3.4.1 Two-Sub event cumulants

In the standard calculation of the intrinsic moments, each particle is taken in the full acceptance region of the detector $|\eta| < 0.8$. Thus by obtaining the correlation measurements in the experiment, we sum the contribution from particles in distant and close proximity to each other. While the correlation between distant particles is considered to arise from the collective expansion of the system, a correlation between particles in close proximity can arise from the energetic stream of particles produced in jets which unfortunately produces a bias in the measurements. These effects are typically denoted as short-range correlations. To suppress these short-range effects a gap in the pseudorapidity $|\Delta\eta|$ can be enforced such that only distant particles are correlated [53][12]. Separating the detector into two independent regions, namely sub-event A and sub-event B an additional constraint must be made. In calculating the moments one would have to make sure that at least one particle is included from both sub-event A and sub-event B.

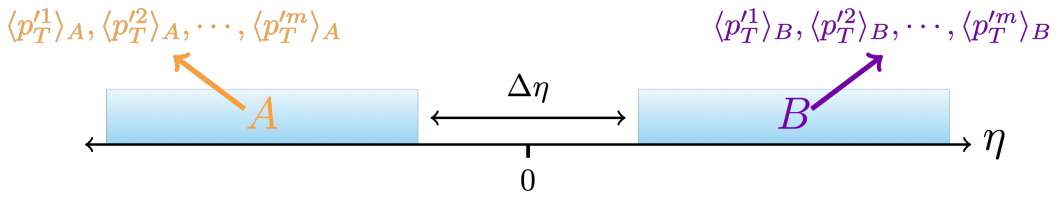

Figure 3.2: Illustration of the side view of the detector with the 2-sub event method with an enforced gap in pseudorapidity $|\Delta\eta|$

[12]The sub-events methods have previously been studied in great details in anisotropic flow analysis of both small and large collisions system [55]

With the generic formula presented, it is possible to apply a shortcut for calculating intrinsic moments with the sub-event constraints. Utilizing the fact that the generic formula isolates every unique particle pair in a given range it is possible to first apply the calculations independently and afterward multiply the sub-events moments. The product will simply expand and mix particles from each event. The principle idea is illustrated in Figure 3.2. The two-sub event moments are defined as

$$\langle p_T'^m \rangle_{2\text{-}sub}^{(ij)} = \langle p_T'^i \rangle_A \langle p_T'^j \rangle_B, \qquad m = i + j \tag{3.33}$$

where (ij) denotes the number of particles used in sub-event A and B respectively. Here it is also noted that for a $m´$th order sub-event moment, there must naturally be a total of m particles in sub-event A and B. The associated cumulants for the sub-event correlation can unfortunately not be derived as easily as previously outlined as the particles in different sub-events now must be treated as different random variables. Consequently, the expansion method[56] does not hold anymore and the cumulants have to be derived according to full expansion in every partition. This approach does unfortunately not have any pretty analytical solution, so the core approach used is kept in Appendix G. We therefore without any further action define the 2-particle cumulant for the two sub-event methods as

$$\kappa(p_T'^2)_{2\text{-}sub} = \langle\!\langle p_T'^2 \rangle\!\rangle_{2\text{-}sub}^{(11)} - \langle\!\langle p_T \rangle\!\rangle_A \langle\!\langle p_T \rangle\!\rangle_B \tag{3.34}$$

4 Data processing and Selection

In this chapter, each step of the analysis procedure will be presented. Firstly a brief summarization of the analysis framework used for data processing on the LHC Grid will be given. Sequently the selection cuts for events and particle tracks will be outlined with the motivation of choice for such cuts. This is followed by applied efficiency correction to account for detector performance, as well as compatibility between different periods of data taking. Finally, the propagation of statistical as well as systematic uncertainties is presented for the final observables.

4.1 Analysis framework

The analysis is performed in two separate steps. The first part of the analysis is performed under the AliPhysics analysis framework developed by the ALICE collaboration for processing of data on the Grid, this is referred to as *online* analysis. The second step consists of final state calculations as well as error propagation which is normally performed on a local machine, this is referred to as *offline* analysis. The effective workflow of the whole analysis is illustrated in Figure 4.1 for a more comprehensible understanding of the different aspects. Each colored component in Figure 4.1 is completely separable, so implementing additional functions or features can be implemented easily. The online analysis is performed by the `AliAnalysisTaskDensity` and `AliPtSubEventContainer` which are two *object-oriented-programming* classes constructed for this thesis. The analysis task has been included on the official AliPhysics GitHub repository[58] and can be found under `PWGCF/FLOW/GF/`.

The `AliAnalysisTaskDensity` task, controls the experiment flow by managing the detector selection criteria which will be outlined in the following section. The class `AliPtSubEventContainer` is used for numerical calculation of the intrinsic p_T moments as introduced in Analysis method and constructed with the generic formulas as the core component. The class is additionally tuned to calculate every term needed for arbitrary orders of two-sub event cumulants, and up to six order p_T cumulants with three-sub events. While they are still accessible within the ALICE analysis framework, they could not be presented in the given time frame of this thesis.

In this analysis presented, data of Pb-Pb collision $\sqrt{s_{NN}} = 5.02$ TeV as well as Xe-Xe collisions at $\sqrt{s_{NN}} = 5.44$ TeV are used. The data were obtained under the LHC Run 2 data-taking period. The collision system, energy, and the anchored run period number are summarised in Table 1. This composes of Pb-Pb data taken in 2015 and 2018 from where additional analysis checks are made to make sure the two periods are compatible with each other.

Collision system	Collision energy	Period number
Pb-Pb	$\sqrt{s_{NN}} = 5.02$ TeV	LHC15o, LHC18q, LHC18r
Xe-Xe	$\sqrt{s_{NN}} = 5.44$ TeV	LHC17n

Table 1: List of the collision system and the data period in which data are obtained

4.2 Event selection

The events used in the analysis are selected from pre-defined criteria already implemented in the ALICE framework. The first layer is used to select events according to the fired trigger. A minimum-bias trigger, kInt7 are selected for all run period and are covering a centrality range of 0-90%. Additional trigger selection for the LHC18qr period is applied with kCentral (0-10% centrality) and kSemiCentral (30-50% centrality). For each event, the centrality is calculated with `AliMultSelection` framework which is an additional integrated part of the AliPhysics analysis framework. The centrality for each event is calculated based on the trigger and centrality estimator. For this analysis, the V0M centrality estimator is used which uses the observed

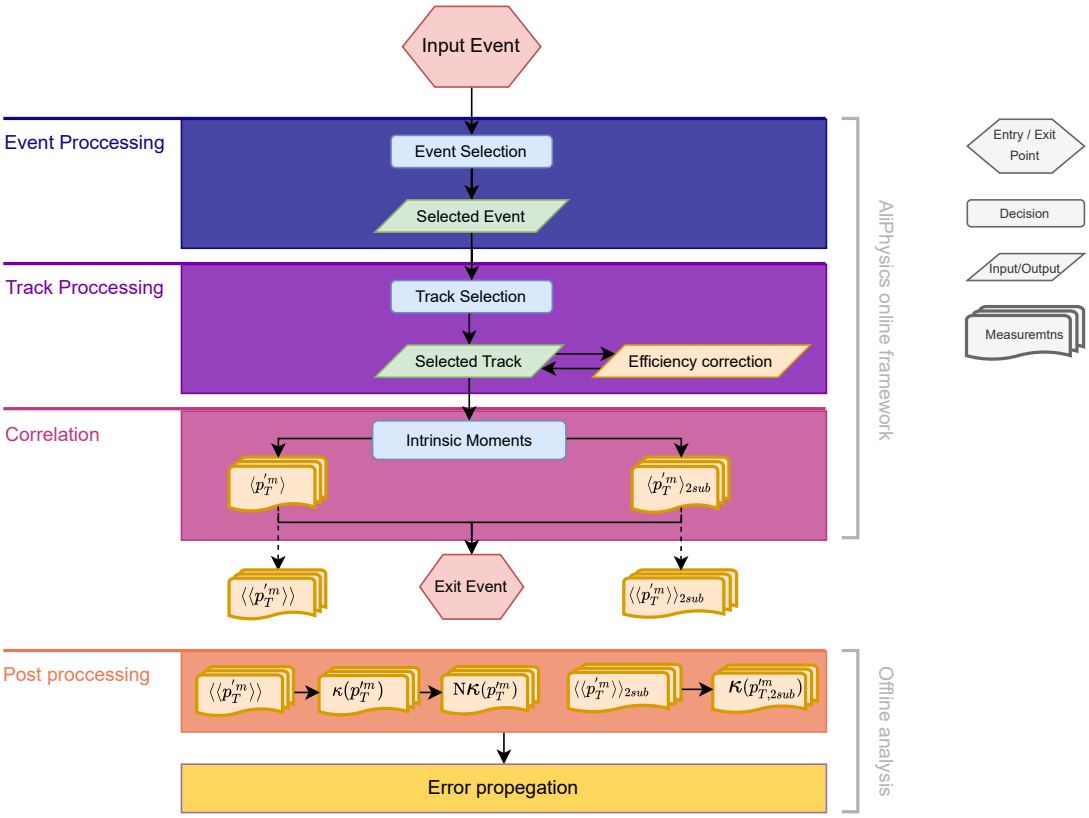

Figure 4.1: Illustration of analysis workflow which consists of a two-step process. The analysis is firstly performed on event-by-event calculations on the LHC Computing Grid, marked by the entry/exit point (red). After online processing, the data are used for post-process calculation and propagation of statistical and systematic uncertainties

multiplicity distribution from V0A and V0C detectors to estimate the centrality. The full event cuts applied to each run period are presented in Table 2.

Primary vertex selection

The events are further required to stem from within ±10 cm of the nominal collision point $|V_z| \leq 10$. This cut is made to ensure full pseudorapidity coverage of produced particle tracks in the central barrel region $|\eta| < 0.8$. The primary vertex is determined from the information of the SPD layer, which is the innermost layer of the ITS detector.

Pileup rejection

With a million events occurring each second, it is not possible for the interactions trigger to completely isolate each event information. Consequently, this leads to the event-mixing of particles originating from different collisions. These events are referred to as pile-up events and are classified as same-bunch or out-of-bunch pile-ups. Same-bunch pile-up events happen from collisions in the same bunch crossing and out-of-bunch happens from collisions in other bunch crossings. Pileup-rejection is managed by the `AliEventCuts`[13].

The first step of pile-up rejection is done by making sure that each event only has a single reconstructed primary vertex as multiple would indicate a large amount of track mixing, and

[13] An additional specialized part of the AliPhysics analysis framework

hence pile-up. The additional track originating in pile-up events would also result in a larger amount of clusters being triggered in the TPC compared to a single event. Additional cuts are thus enforced by ensuring a correlation between the centrality estimation from V0M and CL0 estimators. The correlation before and after pile-up rejection can be seen in Figure 4.2.

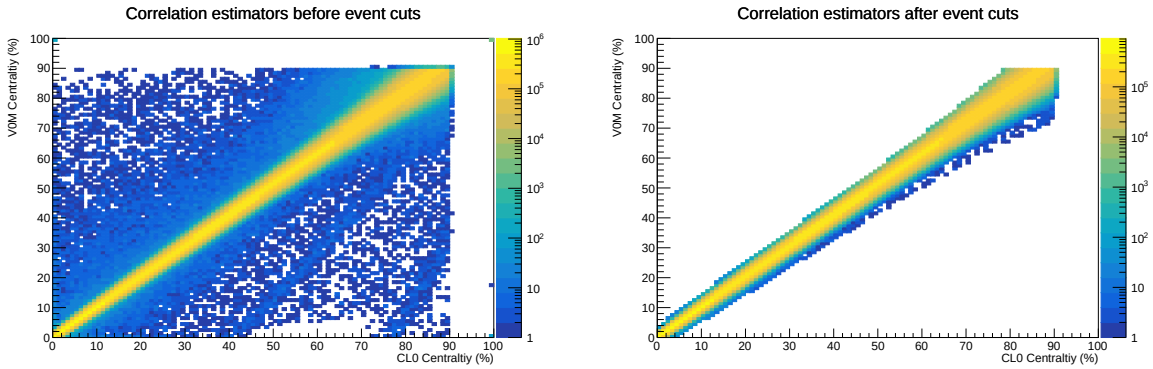

Figure 4.2: LHC15o centrality correlation between V0M and CL0 estimators. Left: Before events cuts. Right: After events cuts. The implementation act as a first step to reduce the number of pileup events

Data	Cut type	Cut value
LHC18qr	Trigger	kInt7, kCentral, kSemiCentral
	V_z	< 10 cm
	Pileup	> 15000
LHC150	Trigger	kInt7
	V_z	< 10 cm
	Pileup	> 15000
LHC17n	Trigger	kInt7
	V_z	< 10 cm
	Pileup	> 15000

Table 2: List of events cuts applied for run periods. During the 2018 run, additional triggers were taken into action. These corresponds are focused to capture central and semi-central events

4.3 Track selection

After an event has passed the selection criteria each track undergoes additional filtering. The online framework allows for quick track selection according to pre-defined cuts. In this analysis *global-tracks* are used, also known as *filterbit 96*, but additional constraints are also implemented. Global tracks use information from both ITS and TPC to constrain the track and ensure high quality. The global track cuts are defined in the following list.

Global Track - Cut list

- Minimum of 70 hits in the TPC clusters
- Maximum $\chi^2 \leq 4$ of the track fit per TPC cluster
- Maximum $\chi^2 \leq 36$ of the track fit per ITS cluster
- A minimum of óne hit in the SPD or SDD

- A cut on the longitudinal distance of closest approach $|DCA_z| < 2$.
- A cut on the transverse distance of closest approach $|DCA_{xy}| < 0.0105 + 0.0350/p_T^{1.1}$
- A converged track fit in the final stage of reconstruction

Each reconstructed track is propagated backward to predict the point of origin and make sure that it is within some range of the nominal interaction point V_z of the collision. This is done through the distance of the closest approach which is applied in the z and xy-plane independently. In the z-plane a distance of the closest approach is chosen within 2 centimeters of the primary vertex $|DCA_z| < 2$. Due to the large solenoid magnet in the detector, the particle trajectory is subject to additional bending and consequently bias in the reconstruction. For this reason, a p_T dependent DCA cut is made in the xy-plane $|DCA_{xy}|$. As can be seen from the list of global track cuts, the $|DCA_{xy}|$ cut is defined such that low momentum particles are required to be closer to the primary vertex in order to minimize the effect of the magnetic field strength. This also makes intuitive sense since a higher momentum would result in less bending and thus provide a more straight line to fit in the final reconstruction phase. Besides the default cut applied in the filter-bit selection, an additional constraint is set on the χ^2 per TPC clusters which are tuned to ≤ 2.5. The additional cut are regularly applied for Pb-Pb collisions after 2015 as part of the ALICE TPC upgrade which resulted in a more narrow χ^2 distribution[14]. The complete list of cuts applied can be seen in **??**, as will be presented in the following section about systematic uncertainties.

Physics selection	Type	Range
	p_T[GeV/c]	$[0.2, 3.0]$
	η	$[-0.8, 0.8]$

Table 3: Kinematic cuts off the track as used in the analysis.

Additional cuts are made to the physical quantities of the track in an event. While the global track cuts constrain the track resolution, the physics selection can pose a greater significance and are prone to more dramatic changes when tuned. Only tracks selected within $|\eta| < 0.8$ of the central barrel are selected such that full tracking is provided for all tracks. The transverse momentum is additionally bounded in the range $0.2 < p_T < 3.0$ GeV/c to exclude low momentum particles and reduce possible jet inclusion[15]. The physics cuts are listed in Table 3. A quality check (QA) is made of all the listed observables before any advancements are made in the data analysis. With the LHC2015o period as an example, the track QA is shown in Figure 4.3-4.4 .

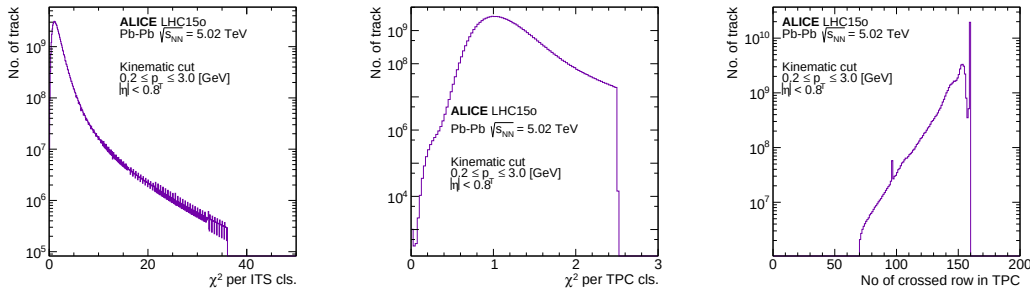

Figure 4.3: QA of track selection in LHC15o for: TPC crossed rows, χ^2 per TPC cls., χ^2 per ITS cls.

[14]This is unfortunately one of these things that are documented in personal analysis note within ALICE and therefore not public

[15]jets normally result in a large number of high momentum particles

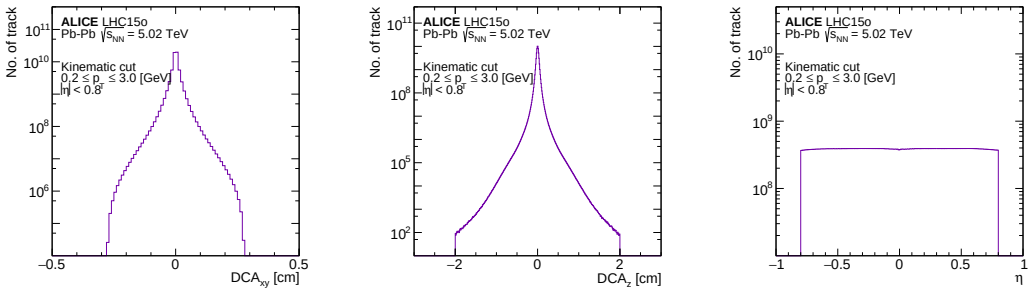

Figure 4.4: QA of track selection in LHC15o for: $|DCA_{xy}|$, $|DCA_z|$, η

4.4 Efficiency correction for transverse momentum

The measurements of particle momenta are determined from track reconstruction as obtained from propagation throughout the detector. As a consequence, the measured momentum is directly affected by detector efficiency. With the measurements of transverse momentum correlation being sensitive to just tiny fluctuation, it is important to obtain a pure estimate of the particle momentum. To account for this an efficiency correction is applied to the measured p_T which will be presented in this section. The efficiency correction is calculated from Monte-Carlo (MC) simulation, as it is not possible to obtain the true p_T distribution, or even predict it. This is done by using simulated collisions for a given system. For heavy-ion collisions, and for this thesis, HIJING is used as an event generator. First, a pure event is generated, this event does not account for detector loss and efficiency and is referred to as the generated MC sample. Through the generated MC sample it is then possible to obtain the p_T distribution noted as $p_T^{\text{generated}}$. Sequently the passage of the particles through matter is simulated using the GEANT4 toolkit[59] and is referred to as the reconstructed event. With the reconstructed event it is possible to obtain an estimate of how particles in different p_T ranges are lost after matter interaction. This is noted by $N_{ch}^{\text{reconstructed}}$. The efficiency correction is then obtained by the ratio between generated and reconstructed momentum, typically calculated in narrow p_T bins as

$$\text{effeciency}(p_T) = \frac{N_{ch}^{\text{reconstructed}}(p_T)}{N_{ch}^{\text{generated}}(p_T)} \tag{4.1}$$

The efficiency is frequently used for calculating an associated weight factor for the p_T off each particle. The weights for a given particle p_T are calculated as

$$w(p_T) = \frac{1}{\text{effeciency}(p_T)} \tag{4.2}$$

The weights can afterward be applied accordingly as outlined in Equation 3.14. By construction of the weights, it is ensured that $w(p_T) > 1$ so that a higher emphasis is put on particles obtained in low-efficiency regions. The reconstructed events are additionally anchored to a specific run period which accounts for the at-the-time state and efficiency of the detector. This is ensured by verifying that the reconstructed data coincide with data as obtained in the experiment. These verifications are made internally within ALICE before the event simulations are made public (to ALICE members), ensuring only high-quality MC productions. Additionally, as each reconstructed MC production is anchored to a specific period of data taking and detector state, it also functions as an important step for making data of different periods compatible with each other. This is due to the continuous upgrades, modification, and not the least degradation of the detector components which happens with the continued years of operation. The efficiencies obtained for Xe-Xe and Pb-Pb collisions with respect to their run period, see Table 1, are presented in Figure 4.5 for different systematic cuts applied.

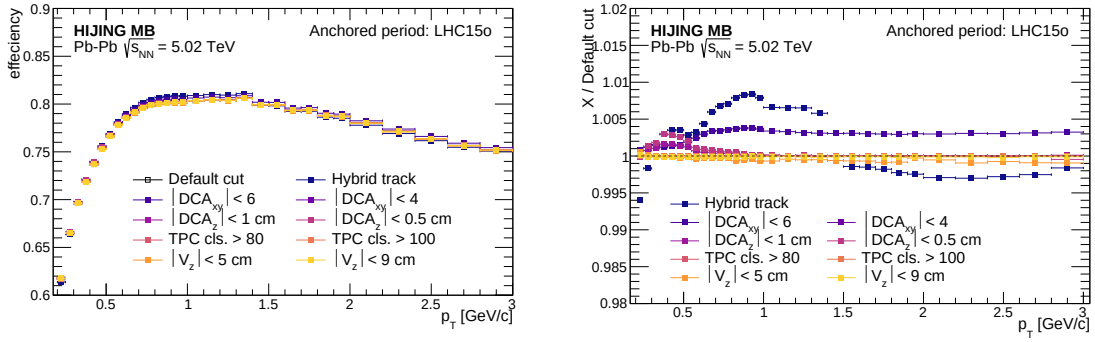

Figure 4.5: Left: Efficiency for Pb-Pb as obtained with different systematics cut. Right: Change of efficiency with respect to the default cut used as outlined under Event selection and Track selection. For systematic cuts with multiple curt values (as will be introduced in the following section), only the upper and lower values are plotted)

The efficiencies are calculated in p_T bins covering the range $0.2 \leq p_T \leq 3.$ [GeV/c], corresponding to the default physics cut as presented in subsection 4.3. As can be seen, the low p_T region surfers larger inefficiency that is shared between every run period and cut. This is partly due to the momentum resolution of the central-barrel detector where the TPC has an effective resolution of $0.1 \leq p \leq 100$ [GeV/c][39]. The most significant change in the Pb-Pb data sets can though be seen to come from the hybrid tracks which have more loose constraints on the track reconstruction such as a higher maximum χ^2 per TPC clusters and $|\mathrm{DCA}_z|$.

4.5 Compatibility check between run periods

While every period of data taking at LHC[16] contains the same physics, it is not always possible to combine data from different periods due to the replacement of detector parts, detector efficiency, and also the sensitivity of observables. Before any data can be merged a qualitative analysis has to be presented and discussed before any proceedings are made. In this section, the compatibility of Pb-Pb collisions at $\sqrt{s_{NN}} = 5.02$ TeV between the LHC15o and LHC18qr periods are outlined with respect to the base observable, the intrinsic moments. The moments $\langle p_T^m \rangle$ for both run periods can be seen in Figure 4.6 (Left) and the ratio of LHC18qr with respect to LHC15o (Right).

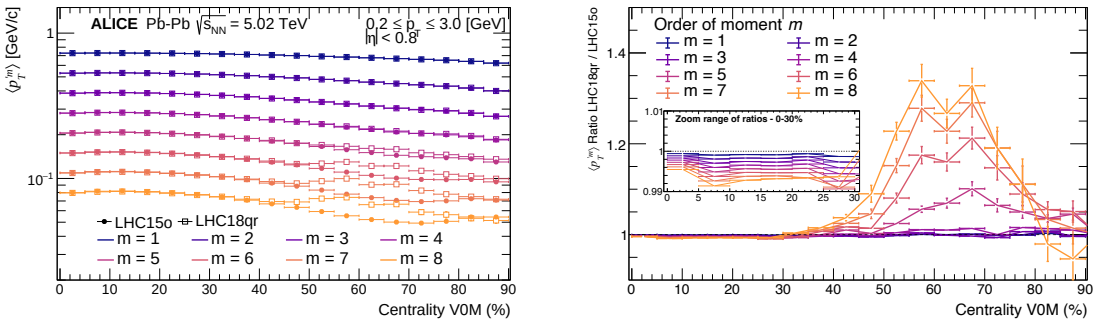

Figure 4.6: Left: Intrinsic moments of the LHC15o and LHC18qr run periods for $m = 1, \ldots, 8$. Right: Ratio of moments of LHC18qr data with respect to LHC15o data. Large deviation observed from semi-central to peripheral centrality range

[16] considering same system and energy

Before the data sets are compared the NUE correction, as presented in the previous section, is applied to the observables in order to minimize the difference in detector performance between periods. For low-order moments $m = 1, 2, 3, 4$ no clear deviation can be observed between the two data sets. Though with the power law scaling of the moments, the trends also get amplified. explained by statistical fluctuations due to low uncertainties. A clear deviation of trends between the two periods can be observed for the higher order $m = 5, 6, 7, 8$ in the semi-central to semi-peripheral centrality range. The observed deviation shows a clear structure that cannot be. While the lower order moments are within 0.5% agreement with each other the explicit expression of the cumulants should also be taken into account. As noted in Equation 3.22-3.25 the cumulants follow a power law expansion of the moments. Consequently, the relatively small deviation will be additionally amplified and the 0.5% deviation could go up to $\approx 2.\%$ and higher. With the power scaling behavior of the observables and observed structure in the LHC18qr it is decided not to go forth with the merging of the two data sets as they are not compatible with each other. Though to keep a complete analysis of the current Pb-Pb collisions that are available, the LHC18qr data will be presented independently as an appendix. The reason for going forwards with LHC15o data is due to its additional years of usage and tests.

4.6 Uncertainties

No physical experiment consists of uncertainty-free data. For this reason, this section provides the steps taken from experimental measurements to final observables and associated observables. Firstly the non-parametric bootstrap method which will function as the base step of error propagation will be outlined for obtaining observable uncertainty. Additionally, the steps for rebinning and comparison of different measurements are outlined.

4.6.1 Statistical uncertainty

As presented in Chapter 3, the number of terms in the final cumulants observables $\kappa(p_T'^m)$ and $\widetilde{\kappa}(p_T'^m)$ reaches a tremendous order. Using analytical error propagation with derivatives would result in all complex terms with associated correlation coefficients which would have to be included in the final result. While it is possible to obtain a full analytical expression for the lower orders m=2, 3 it quickly becomes impossible. To keep a consistent method across both low and higher-order observables the *Bootstrap* method[60] is used for the propagation of final results. The bootstrap method is a non-parametric resampling technique for variance estimation and can therefore be implemented without any complex inferences about the population. In the online part of the analysis, each calculation of the intrinsic moments is randomly divided into sub-samples which all consist of roughly the same amount of data. In the offline part of the analysis, each cumulant observables $\kappa(p_T'^m)$ and $\widetilde{\kappa}(p_T'^m)$ are calculated for each sub-sample set. With 10 sub-samples a total of B data-sample $\widehat{\theta}_i$ is created by combining 10 randomly selected samples with repetition. Each new set is combined as a weighted average with the weight assigned according to the number of samples $w = 1/10$. The central value of the measurements is obtained as the average value of the resampled bootstrap distribution, with the standard deviation calculated as

$$\sigma_\theta = \sqrt{\frac{1}{B-1}\sum_{i=1}^{B}\left(\widehat{\theta}_i - \bar{\theta}\right)^2} \tag{4.3}$$

It was discovered during the analysis that a too high sample size B (≈ 10.000) could result in an underestimation of the errors associated with MC-generated data. The underestimation of error is also a known drawback of the bootstrap resampling method. Though despite the underestimation of errors, the bootstrap method as applied in high-energy heavy-ion physics proves a robust and efficient method[61]. In this analysis, a distribution is made with $B = 500$ samples which were found to be an appropriate bound for the observables.

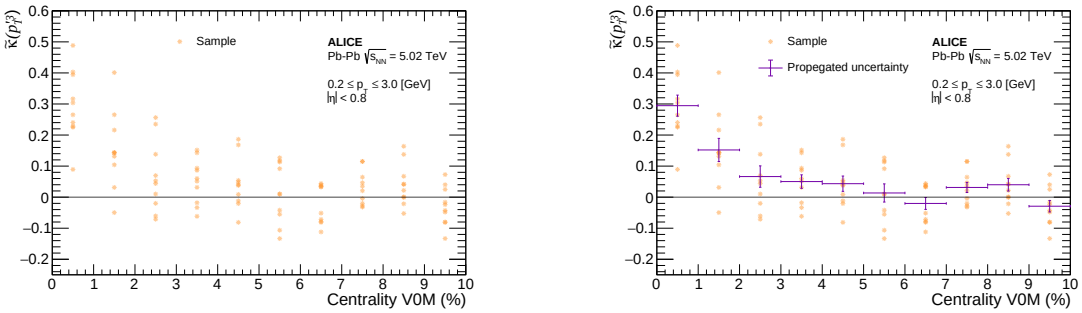

Figure 4.7: Left: The 10 raw sub-samples of the third standardized cumulants $\widetilde{\kappa}(p_T'^3)$. Right: The raw 10 sub-samples of the third standardized cumulants $\widetilde{\kappa}(p_T'^3)$ with bootstrap propagated uncertainties

The method as applied for the third standardized cumulant $\widetilde{\kappa}(p_T'^3)$ can be seen in Figure 4.7 in the central range $(0-10\%)$. The propagated uncertainties (Right) can be seen to comply with the raw samples in each bin. The procedure is done for each observable in the whole centrality range[17]

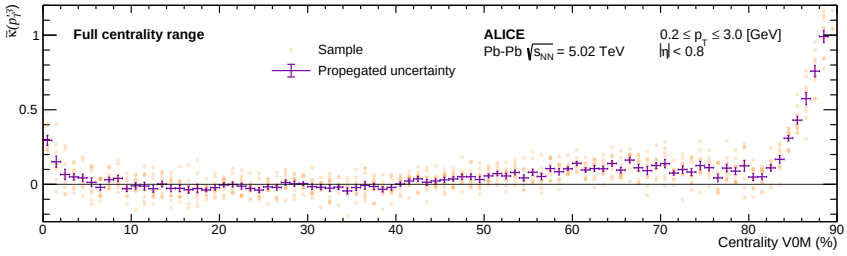

Figure 4.8: The full centrality range as applied for every observable

Rebining of x-axis

To reduce the risk of statistical fluctuation effects between bins all calculations are firstly carried out in centrality bins of c =1% and afterward rebined. This is done to make sure that the data are representative and that small-scale effects are not suppressed. The rebined data are calculated by a weighted mean of the desired neighboring bins c_i given by

$$\bar{c} = \frac{\sum c_i/\sigma_i^2}{\sum 1/\sigma_i^2} \tag{4.4}$$

In Figure 4.9 it can be seen how different bin widths can cause structure suppression in the peripheral region if a too-large bin width is chosen. It can also be seen how a larger bin width can contribute to an underestimation of errors and at the same time result in a more poor representation of data. In general, simulations in this thesis will be presented in bin width of $\Delta\bar{c} = 3$. Though there are still some exceptions as real data suffers from more statistical fluctuations and higher bin widths are therefore needed.

[17] as noted beforehand the centrality range in experiments covers 0-90%

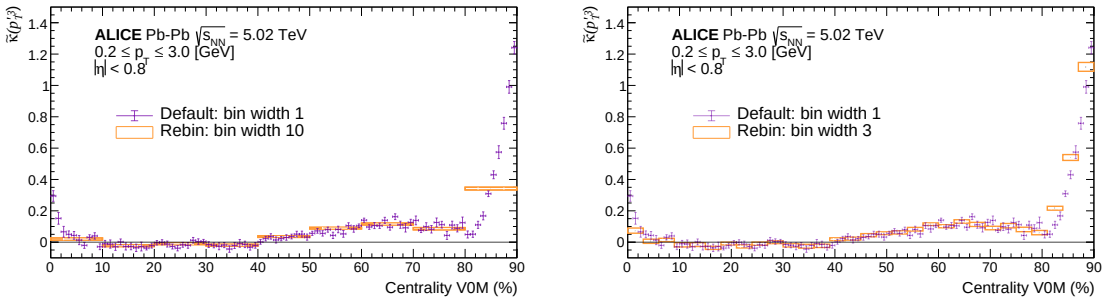

Figure 4.9: Two methods of rebinning. Left: Rebinning of data to a bin width of $\Delta\bar{c} = 10$ together with the default binning. Right: Rebining of data to a bin width of $\Delta\bar{c} = 3$ together with the default binning. As can be seen, the lower bin width conserves the observed structures better

4.6.2 Systematic uncertainties

In the previous section, a description has been outlined regarding the selection of events and subsequent particle tracks in the event. These parameters, such as the requirements of a certain number of hits in the TPC, are more related to the quality of the analysis and not so much to the physics itself. Consequently, the selection of cuts reflects decisions taken by the experimentalist, which can influence the measurements and must therefore be accounted for. This could be by tightening the event selection with respect to the primary vertex V_z. While this would intuitively increase the overall quality of the tracks, it can also affect the statistics as fewer events can be used for the analysis. This section outlines the default cuts, systematic variations, and the complete procedure for including the propagated (systematic) uncertainties in the final results of the thesis. For the selection of the event, the primary vertex is tightened from a default value of $|V_z| < 10$ cm down to $|V_z| < 5$ cm. Additionally, the centrality estimator is switched from the $V0M$ to the $CL0$ and $CL1$ sub-detector which corresponds to the inner and outer components of the ITS. The track cuts are tightened further in $|DCA_{xy}|$ and $|DCA_z|$. The last tight cut is put on the number of crossed rows in the TPC, where it is varied from > 70 to > 100 hits. A loose cut is also tested by using hybrid filterbit 768 tracks. Hybrid tracks are as mentioned more loosely defined in all parameters mentioned. The complete list, with the default cut and the systematic variation, is listed in Table 4 for a complete overview. The p_T dependent cuts applied to DCA_{xy} will be listed as $|DCA_{xy}|$ followed by the associated multiplication factor for that variation, in each figure[18].

For each systematic cut, the statistical significance of variation is calculated for every observable in each bin. The test used is referred to as the Barlow check[62] for fully correlated variables are given by the expression

$$\frac{|x_{def} - x_{sys}|}{\sqrt{|\sigma^2_{def} - \sigma^2_{sys}|}} > 1 \tag{4.5}$$

where x and σ denote the measurement and associated uncertainty respectively. While the measurements are independent of each other, each cut is a subset of the default value and is therefore always correlated to some extent. The Barlow check is calculated bin-by-bin for each observable. If the average Barlow is larger than 1, the variation is considered significant and a systematic uncertainty must be applied to the measurements. If multiple variations of the same cuts, such as $|DCA_z| < 1$ and $|DCA_z| < 0.5$ are considered significant, only the largest contribution will be included. For example, the standardized cumulant $\widetilde{\kappa}(p_T^{|1})$ is calculated for

[18] this is purely to save space in the figures

Parameter	Default cut	Systematic cut
$\lvert V_z \rvert$	< 10 cm	< 9 cm < 7 cm < 5 cm
Centralit est.	V0M	CL0 CL1
$\lvert \mathrm{DCA}_{xy} \rvert$	$< 7 \cdot (0.0026 + 0.005/p_T^{1.01})$	$< 6 \cdot (0.0026 + 0.005/p_T^{1.01})$ $< 4 \cdot (0.0026 + 0.005/p_T^{1.01})$
$\lvert \mathrm{DCA}_z \rvert$	< 2 cm	< 1 cm < 0.5 cm
TPC cls.	>70	>100 >90 >80
Track type.	Global	Hybrid

Table 4: Cuts applied for estimation of systematic variance as done in this thesis. Left panel: Cut variables. Center panel: Default cuts. Right panel: Systematic cuts. The gray-shaded text (CL0 and CL1) denotes variations that are not considered in the final estimation

each cut, see Figure 4.10 (Left). Following the measurements of each cut, the Barlow check is calculated between the *default* and *systematic* cut, see Figure 4.10 (Right). As can be noted every variation gives an average Barlow above unity and is thus considered significant, consequently systematic uncertainties must be applied. While such a high value should raise an eyebrow it can be observed in Figure 4.11 that the relative uncertainty for moat variations, is below 1% which is far from bad. Additionally, as can be observed, the centrality estimators CL0 and CL1 do pose the highest significance score of the Barlow check. With the addition of the direct measurements in Figure 4.10 (Left) this contribution must be commented on as the CL0 and CL1 estimators do not follow the general trend. One explanation of this could be that by using the central barrel of the detector for both analysis and centrality determination, one accidentally introduces a systematic error as the same particle information is used for multiple measurements. For this reason, the systematic cut of CL0 and CL1 is not included in the final propagation and calculation of systematic uncertainties.

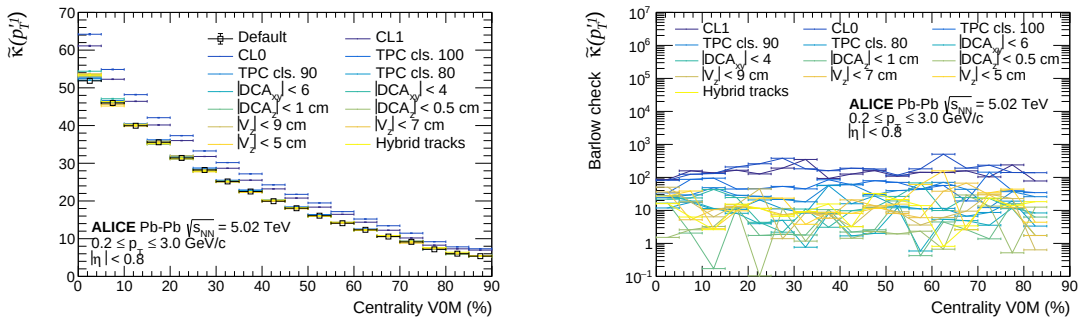

Figure 4.10: Left: Measurements of $\widetilde{\kappa}(p_T^{\prime 1})$ in Pb-Pb collisions at $\sqrt{s_{NN}} = 5.02$ with different systematic cuts. Right: Barlow checks for all systematic variation with respect to the default cut. The values $1 <$ signifies a significant source of variation that must be used to assign additional uncertainties

The relative uncertainty for each systematic source is fitted with a *pol*0 fit as it is assumed to be constant for the whole centrality range. This assumption is also reasonable as presented in

the final bin width as seen from Figure 4.11.

$$\frac{|x^i_{def} - x^i_{sys}|}{|x^i_{def}|} \xrightarrow{pol0} \left(\frac{\Delta x}{x}\right)$$

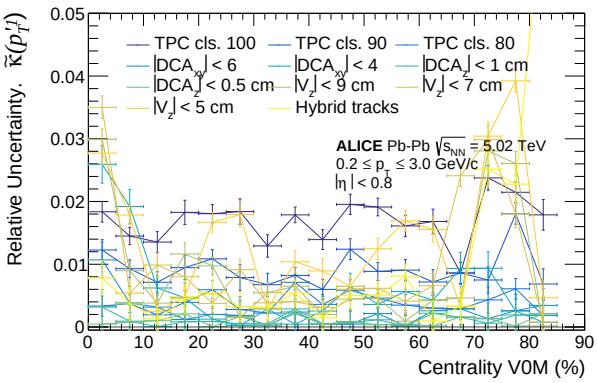

Figure 4.11: Each source contribution to the relative uncertainty of $\widetilde{\kappa}(p_T'^1)$ in Pb-Pb collisions at $\sqrt{s_{NN}} = 5.02$. Each source are then fitted by a pol0 fit which all are available in Appendix C.

The final systematic uncertainties are obtained as the square root of the quadratic sum for each contributing source.

$$\delta x_{sys} = \sqrt{\sum_{j=1}^{N} \left(\frac{\Delta x}{x}\right)^2_j} \tag{4.6}$$

Concluding remarks on the processing of data

After the complete procedure of data processing, from applying NUE correction to the propagation of statistical and systematic uncertainties an overview of the experimental data with respect to the presented probe is obtained. While the measurements of the higher order standardized cumulants $\widetilde{\kappa}(p_T'^m)$ can be obtained with high precision in simulation, the same does not hold true for real data. With the complete data processing as outlined in this section, it has only been possible to make a proper representation of first and third-order standardized cumulants $\widetilde{\kappa}(p_T'^1)$ and $\widetilde{\kappa}(p_T'^3)$ respectively, together with the raw p_T cumulants $\kappa(p_T'^2)$. For Pb-Pb collisions, a total of ≈ 48 million events passed all events selection criteria and were included in the final analysis. Though the Xe-Xe collision recorded during the LHC run2 where not an integrated part of the run schedule, so only a limited amount of events exist. For Xe-Xe collision an ≈ 1.3 million passed all triggers and was used for analysis. While this number is relatively low, compared to the Pb dataset it is possible to make a proper estimation of $\widetilde{\kappa}(p_T'^1)$ and $\kappa(p_T'^2)$. As the statistical fluctuations are quite large of the $\kappa(p_T'^3)$ observable in Xe-Xe collisions, the systematic uncertainties assigned for this should be taken with a grain of salt. A full evaluation of systematics sources is however carried out and the appropriate contribution is added. A complete list of figures and associated fits for each source of systematics in the Pb-Pb and Xe-Xe data can be found in Appendix C. The final systematic uncertainties for each observable in Pb-Pb and Xe-Xe collisions are listed in Table 5-6 on the following page, with the largest contributor for each variation.

Pb-Pb	$\|V_z\|$	$\|DCA_z\|$	$\|DCA_{xy}\|$	#TPC cls.	hybrid tracks	**Assigned unc.**
$\kappa(p_T'^2)$	2.7%	0.2%	1.8%	5.2%	2.4%	**6.6%**
$\widetilde{\kappa}(p_T'^1)$	1.5%	0.1%	0.5%	1.7%	0.7%	**2.4%**
$\widetilde{\kappa}(p_T'^3)$	14%	2.6%	14.%	15.6%	55%	**60.1%**

Table 5: Relative uncertainty from different systematic sources in Pb-Pb collision at $\sqrt{s_{NN}} = 5.02$ TeV. Each outlined variation (in %) is taken at the largest contribution from alike cuts. The combined systematic uncertainties are outlined on the right side of the table.

Xe-Xe	$\|V_z\|$	$\|DCA_z\|$	$\|DCA_{xy}\|$	#TPC cls.	hybrid tracks	**Assigned unc.**
$\kappa(p_T'^2)$	5.6%	n/a	2.%	2.1%	1.1%	**5.8%**
$\widetilde{\kappa}(p_T'^1)$	2.8%	n/a	1.2%	0.4%	0.3%	**3.1%**
$\widetilde{\kappa}(p_T'^3)$	20%	n/a	n/a	7.4%	4.%	**24.9%**

Table 6: Relative uncertainty from different systematic sources in Xe-Xe collision at $\sqrt{s_{NN}} = 5.44$ TeV. Each outlined variation (in %) is taken at the largest contribution from alike cuts. The combined systematic uncertainties are outlined on the left side of the table.

5 Results and Discussions

In this chapter, measurements of standardized cumulants of transverse momentum fluctuations in ultra-relativistic collisions of Pb-Pb at $\sqrt{s_{NN}} = 5.02$ TeV and Xe-Xe at $\sqrt{s_{NN}} = 5.44$ TeV will be presented. These measurements aim to provide insight into collective effects in heavy-ion collisions and reveal how initial-stage effects, such as nuclear deformation, can be observed in experiments. The first part of the chapter utilizes Monte Carlo simulations to study the sensitivity and response of the standardized cumulant $\widetilde{\kappa}(p_T'^m)$ to different physical processes. Monte Carlo simulation is an essential tool for studying such observables as it provides a controlled framework where every physical process is well understood. The study begins by investigating the origin of non-collective effects using the HIJING model. This analysis includes examining the effects of selecting particles within specified p_T ranges and how higher-order cumulants can be employed to suppress collective effects. The sub-event method is also utilized to suppress short-range correlations, allowing for the study of the non-collective effect of jets. Subsequently, the sensitivity to nuclear deformation is explored using the AMPT model, which simulates collisions of ^{129}Xe with different deformations. This investigation aims to provide valuable insights, that can clarify if the probe can accurately capture a "snap-shot" of the collision in the final stage measurements. By varying the deformation strength β_2 and triaxiality γ, the study focuses on the effect of triaxial deformation and its influence on the nuclear structure's sensitivity. Finally, experimental data from Pb-Pb and Xe-Xe collisions at the LHC are presented and compared to the model predictions. Each section of the chapter includes the presentation of relevant data, followed by discussions and summaries of the findings along the way.

5.1 None collective effects

To study non-collective effects, the Heavy-Ion-Jet-Interaction-Generator (HIJING) model is employed. The HIJING model is a Glauber-based model that simulates pp, pA, and AA collisions. In this model framework, AA collisions are simulated by superposing independent collisions between participating nucleons (N_{part}). The HIJING model[63] provides a robust framework for describing jet and mini-jet production in heavy-ion collisions, which are the primary contributors to non-collective effects[19]. From a statistical perspective, cumulants from an independent source should be inversely proportional to the number of participating nucleons ($\kappa(p_T'^m) \propto 1/N^m_{\text{part}}$) [41, 44]. This quantity additionally scales linearly with the final-state number of observed particles (N_{ch}).

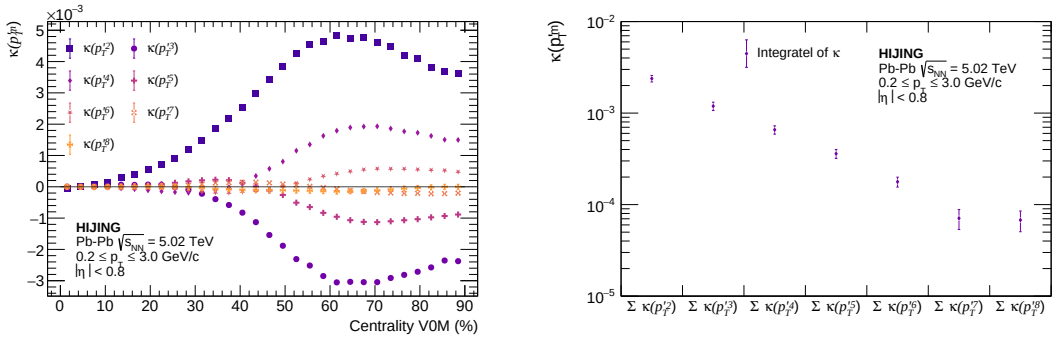

Figure 5.1: Left: Measurements of $\kappa(p_T'^m)$ for $m = 2, 3, 4, 5, 6, 7, 8$ in HIJING. Right: Integrated cumulants values to illustrate independent source scaling

[19] Or at least what is expected based on this model

With the definition of centrality used in this thesis, directly testing the independent source scaling is not possible due to the influence of multiplicity fluctuations in each centrality bin. Instead, the scaling is examined by integrating the measured cumulant values ($\kappa(p_T'^m)$) over the entire centrality range, making the scaling independent of the number of final state particles. The scaling is evaluated based on the magnitude of the integrated cumulant measurements across the 0-90% centrality range, as shown in Figure 5.1 (Left). The integrated cumulants, illustrated in Figure 5.1 (Right), exhibit the expected power scaling behavior. However, it should be noted that summing all $\kappa(p_T'^m)$ contributions in each centrality bin can lead to the loss of included physics. The obtained results demonstrate similar trends to those observed in [53] for $\kappa(p_T'^2)$, $\kappa(p_T'^3)$, and $\kappa(p_T'^4)$, albeit with calculations performed in terms of N_{ch} (number of charged particles).

5.1.1 Short-range correlation

The suppression effect on short-range correlation is tested for the second-order cumulants $\kappa(p_T'^2)$. The efficiency of the method is tested by varying the gap in pseudorapidity $|\Delta\eta|$ from $0 < |\Delta\eta|$ to $0.8 < |\Delta\eta|$. As the applied gap is increased in the pseudorapidity range $\Delta\eta$, as illustrated in Figure 5.2, the effect of short-range correlation is reduced.

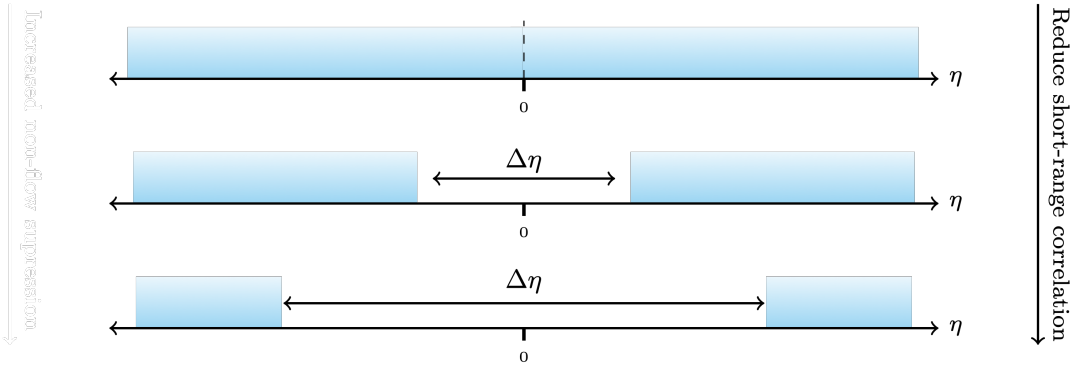

Figure 5.2: Illustration of the side view of the detector with 2-sub event method as non-flow suppression techniques. Increased separation between correlated particles reduces the short-range correlation that is typically associated with jets

In HIJING calculations of $\kappa(p_T'^2)_{2\text{-}sub}$ with different pseudorapidity gaps, the efficiency is tested, as shown in Figure 5.3. It is observed that the applied gap in pseudorapidity reduces the correlation and, consequently, the non-collective contribution. Since collectivity observed in HIJING is mainly associated with jets, this observation indicates that the sub-event method effectively reduces non-collective effects. Additionally, it can be noted that the response is non-linear, and the peripheral range (60-90%) is more biased by non-collective behavior.

Looking at the relative variation in Figure 5.4, it is clear that the central collision is slightly more biased by statistical fluctuations, as there should not exist any physics in the model that would favor such a spike. However, it can be observed that a possible saturation point may be reached at $|\Delta\eta| < 0.4$, as no visible difference is observed beyond this range. This implies that all short-range correlations should be generated within $|\Delta\eta| < 0.4$, which seems reasonable. However, this also suggests that there may be additional sources of collectivity not accounted for in this model that are yet to be understood.

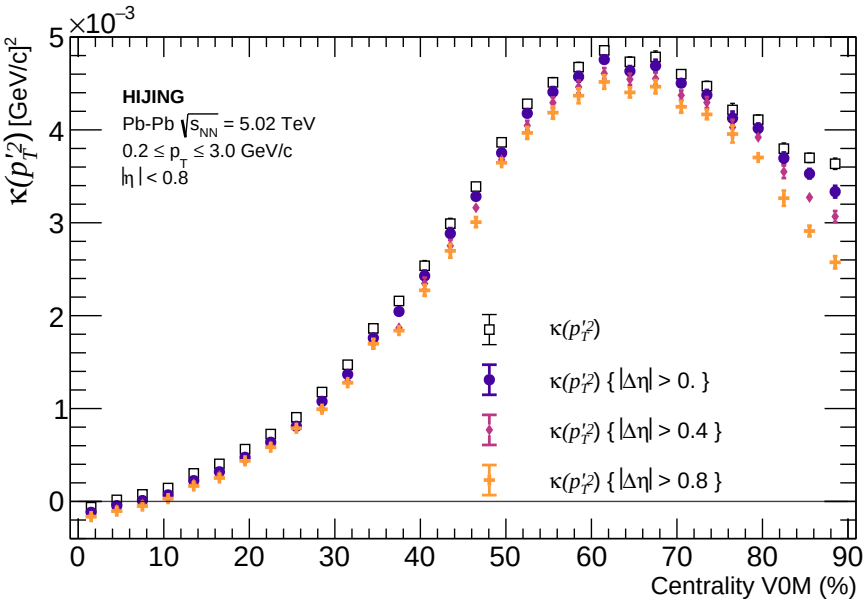

Figure 5.3: Efficiency of two-sub event method for suppression of short-range correlation in HIJING. The cut on pseudorapidity are applied with $0 < |\Delta\eta|$, $0.4 < |\Delta\eta|$ and $0.8 < |\Delta\eta|$. It can be observed that the increased gap between particles reduces short-range correlation

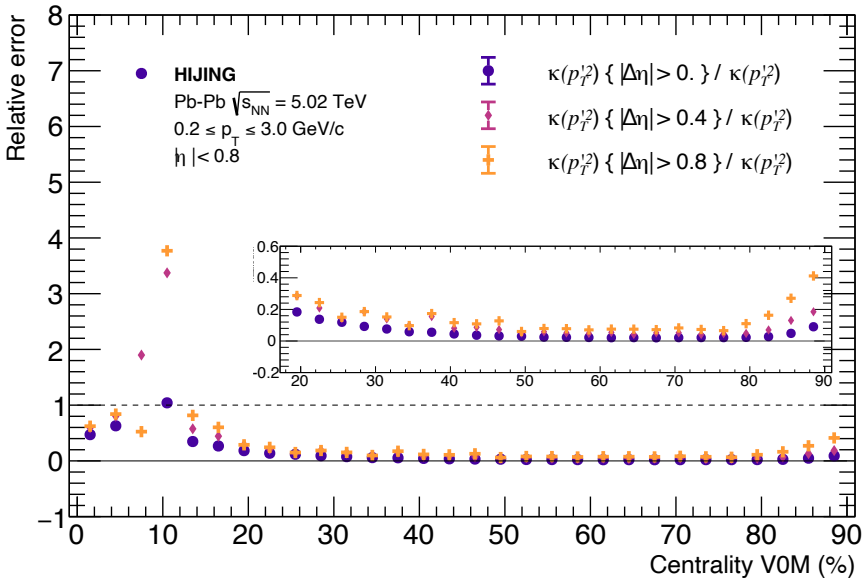

Figure 5.4: Relative deviation between applied eta-gaps for $0 < |\Delta\eta|$, $0.4 < |\Delta\eta|$ and $0.8 < |\Delta\eta|$ with respect to no gaps. Noted in the zoomed-in plot, a saturation point might occur at $0.4 < |\Delta\eta|$ as the increased gap does not pose any significant difference.

5.2 Response to transverse momentum

As mentioned in previous sections, the inclusion of jets is one of the dominant sources of non-collective effects. By varying the cuts on p_T, we can investigate the effect on "jet" regions and differentiate between high and low-momentum particles. The measurements of the raw cumulants $\kappa(p_T'^m)$ exhibit a non-linear response to the chosen p_T range, as shown in Figure 5.5[20]. Applying upper and lower cuts on p_T allows us to observe the differences between low and high-momentum particles. It is evident that increasing the uppercut, potentially introducing jet streams, also increases the magnitude of collective effects as expected. This effect is further amplified by raising the lower cut to $0.5 \leq p_T \leq 3.$ and $0.7 \leq p_T \leq 3.$ [GeV/c], as seen in Figure 5.5-5.6. This clear dependence on high-energy particles indicates their significant contribution to non-collective effects. However, while these measurements confirm the assumption of collective effects arising from jets, they also reveal interesting and unknown effects in the measurements of standardized cumulants, which can lead to ambiguous conclusions.

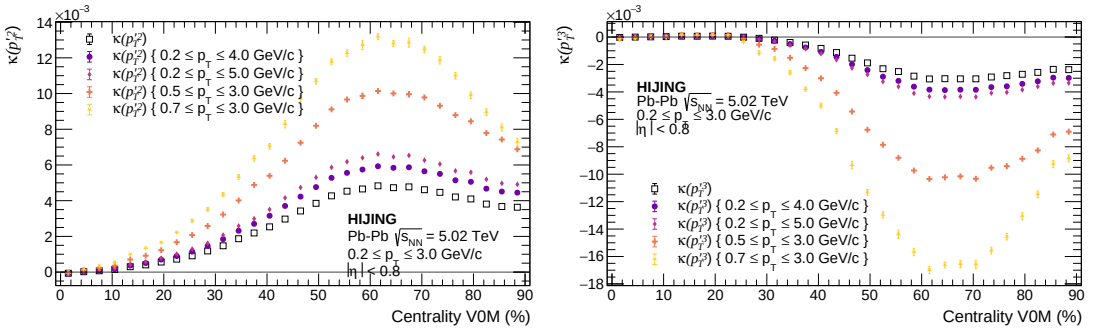

Figure 5.5: Measurements of $\kappa(p_T'^m)$ for $m = 2, 3$ with respect to different p_T cuts. The uppercut can be seen to amplify the response by many factors compared to the lower cut

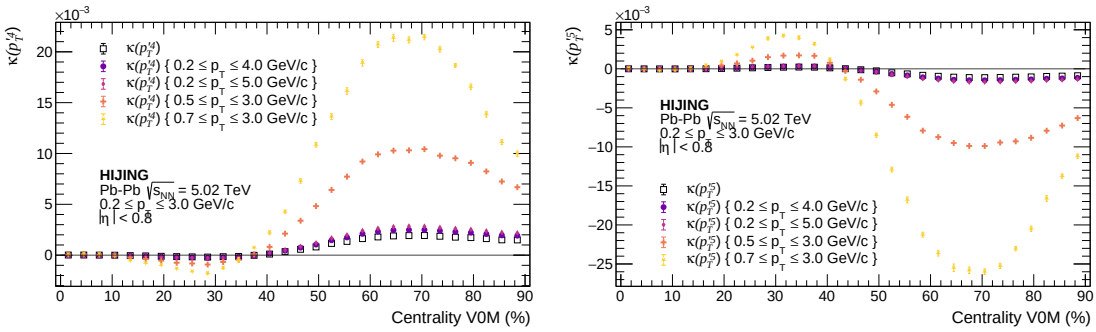

Figure 5.6: Measurements of $\kappa(p_T'^m)$ for $m = 4, 5$ with respect to different p_T cuts. The uppercut can be seen to amplify the response by many factors compared to the lower cut

[20]The full list of results can be found in Appendix B, including additional zoomed-in graphs for the central region.

Standardized cumulants

In HIJING calculations, the results of the second-order cumulant $\kappa(p_T'^2)$ were negative in the low centrality range, which was unexpected. However, this is within statistical fluctuation and could be partially attributed to operational steps in the online framework, which may have affected the full production. As the standardized cumulants depend on $\sqrt{\kappa(p_T'^2)}$, it is not possible to obtain a complete spectrum. Therefore, the range of 0-10% will be shaded gray in the presented figures of standardized cumulants. The measurements show a clear splitting of the upper and lower p_T cuts compared to the regular $0.2 \leq p_T \leq 3$ [GeV/c] range. In both $\widetilde{\kappa}(p_T'^1)$ and $\widetilde{\kappa}(p_T'^3)$, it can be observed that increasing the upper cut from 3. to 4.0 and 5.0 GeV/c, respectively, reduces the magnitude of $\widetilde{\kappa}(p_T'^m)$. This trend is also confirmed by all higher-order $\widetilde{\kappa}(p_T'^m)$ presented in Appendix B. Similarly, by increasing the lower cuts to 0.5 and 0.7 GeV/c, respectively, it can be observed that the magnitude of $\widetilde{\kappa}(p_T'^m)$ increases, indicating the expected response of non-collective contribution. The indication that the inclusion of high-momentum particles should reduce non-collective effects is not understood, and no theoretical explanation can be outlined at this moment.

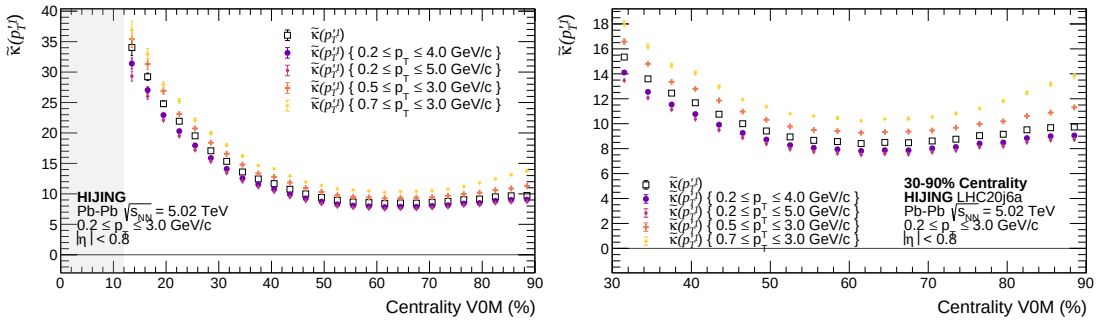

Figure 5.7: Measurements of standardized cumulants $\widetilde{\kappa}(p_T'^1)$ with respect to cuts in p_T range. Left: The standardized cumulants can be observed to split around the $0.2 \leq p_T \leq 3.$ [GeV/c] range with respect to a lower or uppercut the p_T range. The split indicates that by including additional higher-momentum particles, the collectivity should decrease. Right: Same plot but adjusted to 30-90% centrality for a more clear difference in the splitting

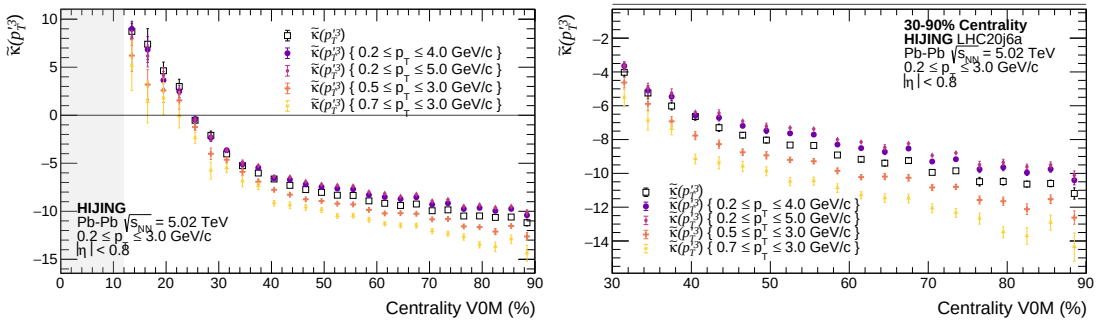

Figure 5.8: Measurements of standardized cumulants $\widetilde{\kappa}(p_T'^3)$ with respect to cuts in p_T range. Left: The standardized cumulants can be observed to split around the $0.2 \leq p_T \leq 3.$ [GeV/c] range with respect to a lower or uppercut the p_T range. The split indicates that by including additional higher-momentum particles, the collectivity should decrease. Right: Same plot but adjusted to 30-90% centrality for a more clear difference in the splitting

Though[21], one suggestion could be that the increased cuts, whether they are lower or upper, introduce a direct scaling of the regular cumulants $\kappa(p_T'^m)$. In the standardization process, this scaling is canceled out, resulting in a more natural reflection of correlation factors. This would imply that by cutting off high-momentum particles, one inadvertently excludes more information about the initial conditions than intended. This idea is also mentioned in [64], where it is discussed that the granularity of the initial condition directly probes higher p_T particles. Although this discussion is in the context of a hydrodynamic picture, it is clear that the initial condition has significant implications for the p_T spectrum.

Summery of non-collective effects

The efficiency of using higher cumulants as a means to suppress non-collective effects has been successfully tested. Moreover, the impact on short-range correlation has been investigated, and the HIJING studies suggest a possible saturation point for an eta separation of $0.4 < |\Delta\eta|$. Importantly, the standardized cumulants $\widetilde{\kappa}(p_T'^m)$ have been shown to be a more effective probe for collective behavior in heavy-ion collisions, but they also reveal unexplained effects. These observations highlight the need for further investigation into the origin of these effects, as the current understanding is insufficient to make definitive claims at this stage.

5.3 Response to quadrupole deformation

To study the effect of nuclear structures on the standardized cumulants of transverse momentum fluctuations, local production of Xe-Xe collisions has been conducted[22]. This includes an improved version where the initial nucleons can be sampled from the deformed density function, as described in Equation 1.2-1.3. The xenon isotope ^{129}Xe has been chosen to match the xenon collisions accessible at the LHC. The deformation study is carried out using the *A Multi-Phase Transport Model* (AMPT) to investigate the conversion from the initial nucleon density d_T to the final state p_T spectra. The AMPT model[65] is a multi-stage framework that aims to describe the entire evolution of heavy-ion collisions. While the model can accurately characterize the initial eccentricity ϵ_2 of the overlap between the colliding nuclei and the measured flow harmonics v_2, it fails to describe the radial flow[24]. Therefore, the higher-order transverse momentum fluctuations cannot be directly compared with data obtained at the LHC. However, the model can provide initial indications and enable the observation of effects during the final stage of the collision. Thus, the model is used solely to study a possible response in the parametrization of nuclear structures/shapes with β_2 and γ.

The deformation effects on transverse momentum fluctuations are studied with four different shapes: spherical, prolate, triaxial, and oblate, as illustrated in Figure 1.9. The spherical nuclei serve as the reference spectrum with $\beta_2 = 0$. The deformed nuclear shapes (prolate, triaxial, and oblate) are tuned with a quadrupole strength of $\beta_2 = 0.18$ and triaxiality values of $\gamma = 0$, $\gamma = 27$, and $\gamma = 60$, respectively. Standardized cumulants $\widetilde{\kappa}(p_T'^m)$ for the deformed nuclei will be presented for $m = 1, 3, 4$. This is because the measurements cannot be completely separated for higher orders due to statistical limitations. The presented figures in the following section will focus on observables that are most relevant for the final discussion. As higher-order cumulants are generally considered to have greater sensitivity to the initial conditions, the lack of statistics is likely the main factor for the limited measurements[23]. The choice of deformation parameters is based on the recent suggestion that ^{129}Xe, in its ground state, exhibits a triaxial structure with $\beta_2 \approx 0.18$ and $\gamma \approx 0.27$[66]. Thus, the triaxial deformation produced in the AMPT model corresponds to the selected baseline. The other forms of deformation are considered to study the sensitivity to β_2 and γ, respectively.

[21] Be part of the solution, not part of the problem, Stephen R. Covey
[22] The post-processing of simulations performed in this thesis is outlined in Appendix D
[23] The complete study includes all orders and can be found in Appendix B

Measurements of $\widetilde{\kappa}(p_T'^1)$ presented in Figure 5.9 (Left) show a small deviation between the different values of β_2 and γ in central 0-15% collisions. However, as the centrality increases towards 30%, a more noticeable grouping, independent of deformation parameters, becomes apparent. Studies on probes for nuclear deformation effects in AA collisions suggest that the strongest impact will be observed in central and ultra-central collisions, where the nuclei collide at a small impact parameter $b \approx 0$[67], allowing for an accurate snapshot of the bodies. As the colliding bodies move away from each other, the rotational degrees of freedom approach those of a spherical baseline, resulting in less deviation in the average observed fluctuation. In measurements of $\widetilde{\kappa}(p_T'^3)$, as seen in Figure 5.9 (Right), a more significant response can be observed for the prolate nuclei in the central region. It can be directly seen that $\widetilde{\kappa}(p_T'^3)$ for the prolate nuclei has a larger magnitude and maintains an opposite sign over a wider centrality range. Additionally, it should be noted that the grouping of every other nuclear shape appears independent of both deformation strength and triaxiality in the central region (0-15%). However, the grouping begins to split in the 15-30% centrality range, where the spherical and deformed nuclei group separate. The increased magnitude of prolate nuclei with $\beta_2 = 0.18$ and $\gamma = 0$ is systematically seen in higher-order standardized cumulants $\widetilde{\kappa}(p_T'^4)$, $\widetilde{\kappa}(p_T'^5)$, $\widetilde{\kappa}(p_T'^6)$, $\widetilde{\kappa}(p_T'^7)$, and $\widetilde{\kappa}(p_T'^8)$, indicating some scaling behavior of the standardized cumulants as a function of deformation.

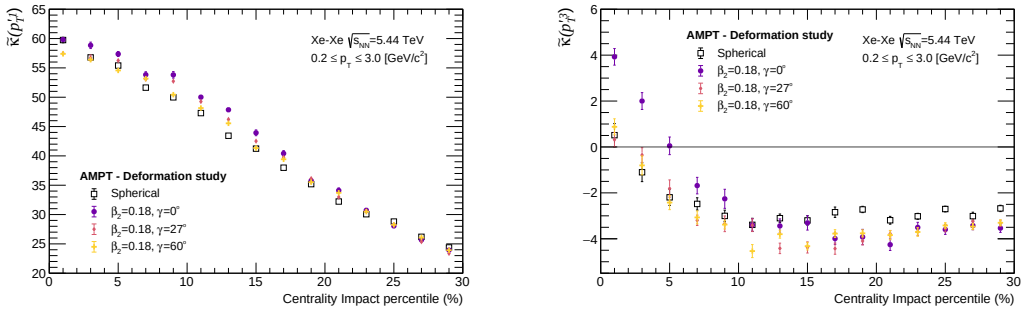

Figure 5.9: Measurements of $\widetilde{\kappa}(p_T'^1)$ and $\widetilde{\kappa}(p_T'^3)$ in collisions of deformed nuclei Left: Measurements of $\widetilde{\kappa}(p_T'^1)$ where a splitting between different deformations can be observed in central collision 0-15%. Right Measurements of $\widetilde{\kappa}(p_T'^3)$ where the prolate can be observed to pose a greater response than the others

In the initial stage calculation, the deformation of nuclei directly affects the transverse nucleon density $d_\perp$, which is also proportional to the final state $\langle p_T \rangle$ fluctuations. Therefore, it is relevant to compare initial and final stage observables to gain insight into the relationship between them. By varying the deformation strength β_2 of colliding uranium nuclei[24], the nucleon density fluctuation S_d increases accordingly, as observed in the final stage $\widetilde{\kappa}(p_T'^3)$. However, when the variation of γ is increased for a fixed $\beta_2 = 0.28$, the shape and slope of S_d decrease, contrary to the observed effect in the final stage, where $\widetilde{\kappa}(p_T'^3)$ only seems to be sensitive to deformation β_2 and not triaxiality γ. It should be noted that in the initial stage calculation, there is a complete opposite sign between S_d and $\widetilde{\kappa}(p_T'^3)$, suggesting a relation such that $S_d \propto -\widetilde{\kappa}(p_T'^3)$. In a hydrodynamic picture, the m'th order $d_\perp$ fluctuation is assumed to be proportional to the m'th order $\langle p_T \rangle$ fluctuation. This would indicate that any constant of proportionality would be negative.

5.3.1 Sensitivity to quadrupole deformation β_2

The relative deviation of the results is calculated with respect to the spherical baseline with $\beta_2 = 0$, and the results are presented in Figure 5.10. This allows for a minor suggestion of possible sensitivity to deformations. The calculations show a relative deviation of approximately

$2-5\%$ for $\widetilde{\kappa}(p_T'^1)$, which remains almost constant over the measured centrality range. Similar behavior is observed for $\widetilde{\kappa}(p_T'^3)$, although there is a clear sign change, as seen in Figure 5.9, specifically for the prolate nuclei. This sign change is not taken into account in the calculation since it is performed based on relative deviations. The behavior of prolate nuclei clearly differs from the others, but a full comparison of the measurements cannot fully account for this. In the initial stage calculation, a formula is used to determine the cumulants of the initial nucleon density, following an expression of the form[24].

$$a' + \beta_2^n(b' + c'\cos(3\gamma)) \tag{5.1}$$

In this parametrization, the centrality-dependent parameters a', b', and c' are not directly correlated to β_2 or γ. Therefore, it is reasonable to assume that the relative deviation presented includes contributions from both γ and β_2, and it is not straightforward to determine the specific contribution of each factor. This concept is further investigated in the sensitivity analysis of triaxiality in the subsequent section.

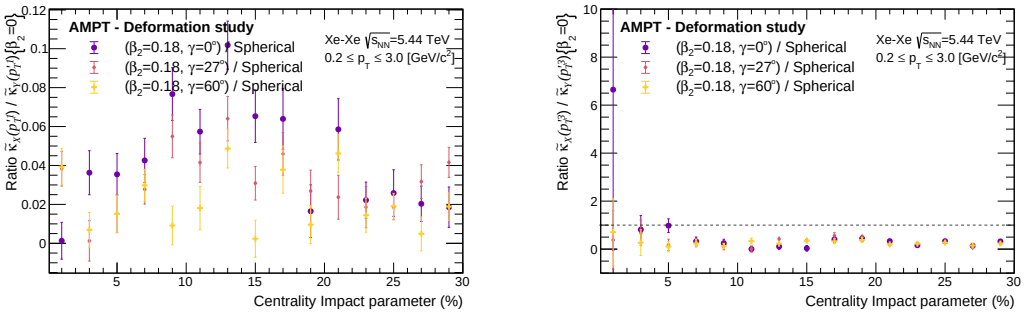

Figure 5.10: Ratios of $\widetilde{\kappa}(p_T'^1)$ and $\widetilde{\kappa}(p_T'^3)$ for collisions of deformed nuclei Left: Ratio of $\widetilde{\kappa}(p_T'^1)$ with respect to the spherical baseline. Right: Ratio of $\widetilde{\kappa}(p_T'^3)$ with respect to the spherical baseline. The observed fluctuation indicates a rather constant difference across the whole centrality range.

5.3.2 Sensitivity to triaxiality γ

In addition to the formula presented in Equation 5.1, it can be observed that when comparing two nuclei with the same quadrupole moment (β_2), the contribution cancels out, and the cumulants become proportional to a centrality-dependent function of the triaxial deformation (γ), given by $a' + c'\cos(3\gamma)$. By examining the relative deviation of nuclei with the same quadrupole moment ($\beta_2 = 0.18$), it is possible to obtain a simplified expression. This reduces the complexity of the problem and allows for a more straightforward analysis. While the first-order standardized cumulant $\widetilde{\kappa}(p_T'^1)$ ratio does not exhibit any apparent response, a more noticeable effect can be observed in the $\widetilde{\kappa}(p_T'^3)$ ratios. The deviation in the $\widetilde{\kappa}(p_T'^3)$ ratios indicates some level of sensitivity to γ after eliminating the influence of the deformation strength, as also observed in the initial stage calculation of the nucleon density.

Motivated by the proposed expression for the ratios ($a' + c'\cos(3\gamma)$), a simple fit is performed to demonstrate the effect, as shown in Figure 5.12. It should be noted that arbitrary functions are proposed and fitted, and the form $p_0 + p_1 \cdot e^{xp_2}$ appears to be favored by the data. The fit is presented with 95% confidence band for each of the nuclei. As can be observed, there is a clear sign that the model is favorable and the deformation effect is significant as observed in the final. Additionally, attempts have been made to analyze higher-order cumulants to investigate if the observed trend persists consistently. However, the available statistics do not provide sufficient

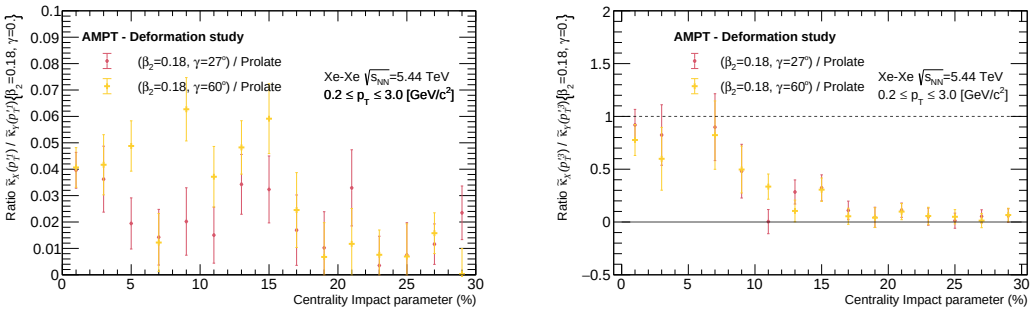

Figure 5.11: Ratios of $\widetilde{\kappa}(p_T'^1)$ and $\widetilde{\kappa}(p_T'^3)$ with respect to prolate nuclei Left: Ratio of $\widetilde{\kappa}(p_T'^1)$. Right: Ratio of $\widetilde{\kappa}(p_T'^3)$ shows a centrality-dependent trend

accuracy for accurate calculations. The result of the fit highlights that there might be a way to access the nuclear structure with $\widetilde{\kappa}(p_T'^3)$ ratios. However, this will mostly be for nuclei with the same quadrupole deformation, as it would only probe the triaxiality γ. As could be observed in calculations of $\widetilde{\kappa}(p_T'^3)$, as shown in Figure 5.9, the quadrupole deformed nuclei approach each other as the centrality range is increased. Consequently, this results in a more apparent trend than could be obtained with respect to the spherical baseline, and hence a more clear description of the data.

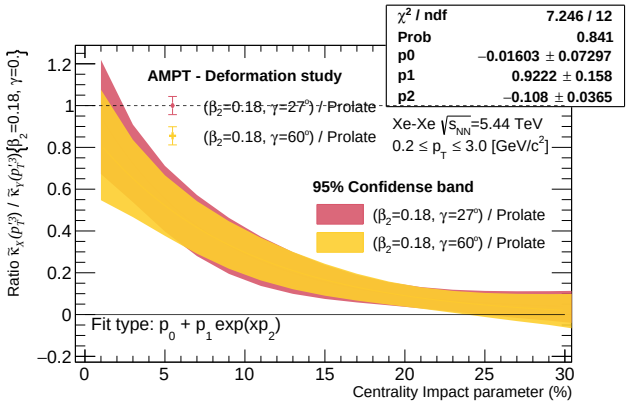

Figure 5.12: Fit of standardized cumulants ratios $\widetilde{\kappa}(p_T'^3)$ with 95% confidence band. While the model does favor the fit, there is no clear difference between the triaxial strength.

Summery of deformation effect

The comparison between the final stage transverse momentum fluctuation ($\widetilde{\kappa}(p_T'^m)$) in collisions of deformed nuclei and the initial stage calculation of nucleon density fluctuation in the overlap region reveals interesting observations. A clear splitting of the prolate nuclei is observed in relation to the third-order standardized cumulant ($\widetilde{\kappa}(p_T'^3)$). However, it cannot be determined at the current stage whether this deviation will increase or saturate for higher orders due to limited statistics. Furthermore, the results indicate that the ratios of $\widetilde{\kappa}(p_T'^3)$ exhibit sensitivity to the triaxiality of the nuclei. This suggests that by comparing measurements of standardized cumulant ratios, it might be possible to further constrain the transverse momentum fluctuation in terms of deformation strength and triaxiality. However, it should be noted that there is still a lack of complete understanding regarding the $\langle p_T \rangle$ spectrum, which should be studied before any conclusion can be made.

5.4 ALICE data

The Monte Carlo studies conducted using the HIJING model revealed splitting between the applied upper and lower cuts which is not fully understood. These findings have motivated the extension of the analysis to real data in order to investigate if similar behavior is present. The analysis involves varying the p_T range used for particle selection, as explained in the previous section. It should be noted that in the data analysis, the uppercut extends beyond the $3. \leq p_T$[GeV/c] range currently available in the NUE (Non-Uniform Efficiency) correction, as shown in Figure 4.5. As a result, the NUE is not included in this additional analysis, and the obtained results cannot be directly compared to the final observables. Furthermore, the study focuses only on Pb-Pb collisions, as this collision system provides the most data. Since the observed effects are expected to be independent of the specific collision system, it is not necessary to include both Xe-Xe collisions in this analysis.

For measurements of $\widetilde{\kappa}(p_T'^1)$ and $\widetilde{\kappa}(p_T'^3)$ in Pb-Pb collisions at $\sqrt{s_{NN}} = 5.02$ TeV, a similar splitting effect as observed in the simulations, is observed in the measurements.

For $\widetilde{\kappa}(p_T'^1)$, the splitting is mostly seen as a constant deviation from the target range of $0.2 \leq p_T \leq 3.0$ [GeV/c]. This deviation is observed from central to semi-central collisions. However, in peripheral collisions (60-90% centrality range), a clear grouping is observed between the applied upper and lower cuts. In the measurements, seen in Figure 5.13 (Left), the splitting can be observed to occur in variations with an increased lower cut. When considering variations in the uppercut ($p_T \leq 4.0$ and $p_T \leq 5.0$ [GeV/c]), it is noted that they both include particles with momentum approaching the lower limit of 0.2 [GeV/c], just as the default cut. This indicates that in the peripheral range, the exclusion of soft particle[24] will increase the magnitude of the measurements. At the same time, it can be observed, how the inclusion of hard particles reduces the measurements, regardless of centrality. This could indicate that by including particles in a wider p_T range, one also includes more information about the system, and the measurements become more robust. Though, before this can be concluded, an additional uppercut on $\leq$ 2.[GeV/c] would need to be measured.

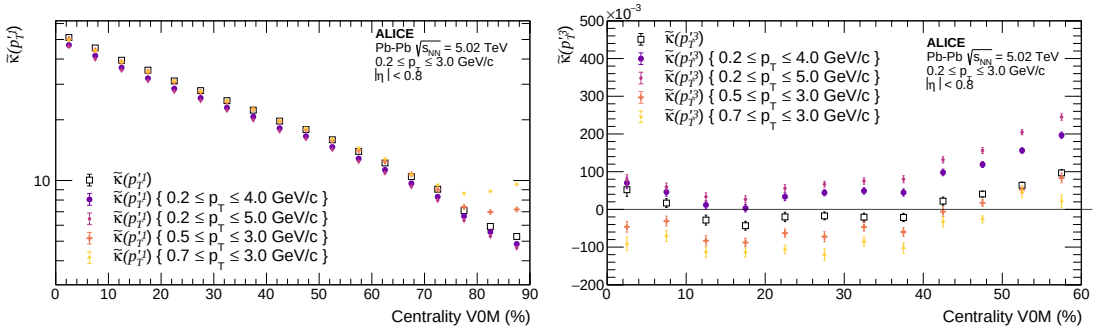

Figure 5.13: Measurements of $\widetilde{\kappa}(p_T'^m)$ response to particle momentum range in Pb-Pb $\sqrt{s_{NN}} =$ 5.02 TeV. The error bars denote the statistical uncertainties associated with each measurement. Left: Measurements $\widetilde{\kappa}(p_T'^1)$ with a different cut on the transverse momentum range. A small grouping and splitting can be observed for peripheral collision in the 60-90% centrality range. Right: Measurements $\widetilde{\kappa}(p_T'^3)$ with different cuts on the transverse momentum range. Switching between the groupings is observed at midcentrality

The splitting effect is also observed in measurements of $\widetilde{\kappa}(p_T'^3)$ across the entire centrality range, as shown in Figure 5.13. Moreover, it can be seen that the default p_T cut undergoes a change in trend around mid-centrality, indicating a shift in the dominant contributions. In

[24] particle with low momentum

low centrality, the dominant contribution is expected to arise from soft processes, while in semi-central collisions, hard scatterings start to become more dominant. Furthermore, the inclusion of high-p_T particles contributes to an overall positive shift in the measurements of $\widetilde{\kappa}(p_T'^3)$ across the probed centrality range. Understanding the behavior of this shift would be relevant in future studies. In related studies, it has been shown that the third-order standardized cumulant of $\langle p_T \rangle$ fluctuations probes the skewness of the p_T distribution. Therefore, a significant sign change as observed in this case, is expected to provide valuable information on the initial conditions and nuclear structure.

5.4.1 Probing nuclear structures at the LHC

Measurements of standardized cumulants, including $\widetilde{\kappa}(p_T'^1)$, $\widetilde{\kappa}(p_T'^3)$, and the second order cumulant $\kappa(p_T'^2)$, have been performed in Pb-Pb collisions at $\sqrt{s_{NN}} = 5.02$ TeV, and in Xe-Xe collisions at $\sqrt{s_{NN}} = 5.44$ TeV. In particular, the measurements of the standardization term $\kappa(p_T'^2)$ show a noticeable difference between the two collision systems, as depicted in Figure 5.14 (Left). This difference might be influenced by the collision energy, making direct comparisons between the systems challenging. Notably, there is a clear deviation between the HIJING model predictions for the two collision systems, suggesting a contradiction in the observed trends that cannot be explained by changes in physics alone. To investigate the possibility of statistical effects causing this deviation, multiple online processing of the data has been conducted, and the deviation can not be associated with the included statistics. In the analysis, the first-order standardized cumulant $\widetilde{\kappa}(p_T'^1)$ incorporates the mean transverse momentum $\langle p_T \rangle$ and is by default dimensionless. Thus, it is suitable for comparing different collision systems. Notably, the measurements of $\widetilde{\kappa}(p_T'^1)$ in Xe-Xe collisions, as shown in Figure 5.14 (Right), are well-described by HIJING calculations compared to $\kappa(p_T'^2)$, as shown in Figure 5.14 (Left). This implies that the fluctuations are more precisely captured by HIJING calculations in the standardized framework. Since HIJING does not include any collective behavior, it raises the question of why these similarities are observed. Furthermore, the measurements of $\widetilde{\kappa}(p_T'^1)$ in Xe-Xe and Pb-Pb collisions exhibit a centrality dependence, where the two measurements approach each other as the collisions become more peripheral. This behavior suggests that the fluctuations converge towards a similar value, in the peripheral collisions. While there is a change in the measurements, it cannot be attributed to any deformation effects. Based on the presented Monte Carlo studies on quadrupole deformation, the first-order standardized cumulants show little to no sensitivity to either deformation strength β_2 or to the triaxiality γ.

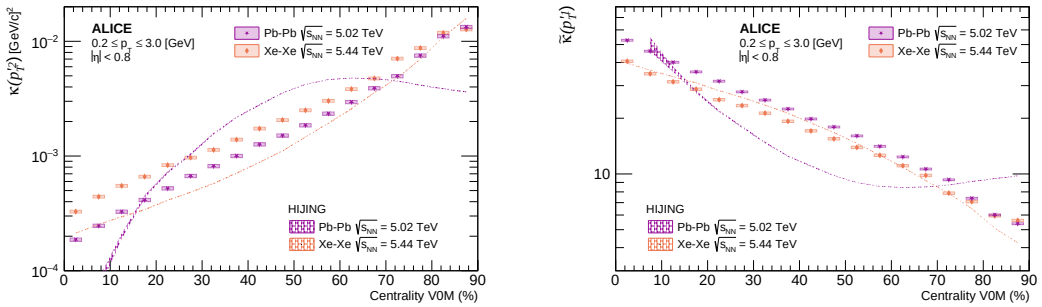

Figure 5.14: Measurements of $\widetilde{\kappa}(p_T'^1)$ and $\kappa(p_T'^2)$ of Pb-Pb (purple star) and Xe-Xe collision (orange diamond) at $\sqrt{s_{NN}} = 5.02$ TeV and $\sqrt{s_{NN}} = 5.44$ TeV respectively with filling representing the associated systematic uncertainties. The anchored HIJING production is shown as the checkered filling matching the collision system color. Left: Measurement of the second order cumulant $\kappa(p_T'^2)$. Right: Measurement of the first order standardized cumulant $\widetilde{\kappa}(p_T'^1)$.

Based on the Monte Carlo studies, the best chance to observe any deformation effect would be in the third-order standardized cumulants $\widetilde{\kappa}(p_T'^3)$. However, due to the current statistics available in Pb-Pb and Xe-Xe collisions at the LHC, it is not possible to provide precise estimates for higher-order cumulants. Furthermore, obtaining accurate measurements in Xe-Xe collisions that are directly comparable to Pb-Pb collisions is challenging. Therefore, it is currently not possible to directly access information on the nuclear structure using the standardized cumulants of transverse momentum fluctuations. Nevertheless, measurements of $\widetilde{\kappa}(p_T'^3)$ in Pb-Pb collisions at $\sqrt{s_{NN}} = 5.02$ TeV, and Xe-Xe collisions at $\sqrt{s_{NN}} = 5.44$ TeV are presented in Figure 5.15. Although these measurements do not provide direct information on nuclear structure, they exhibit certain common characteristics that can contribute to improving our theoretical understanding of the fluctuations observed in collisions.

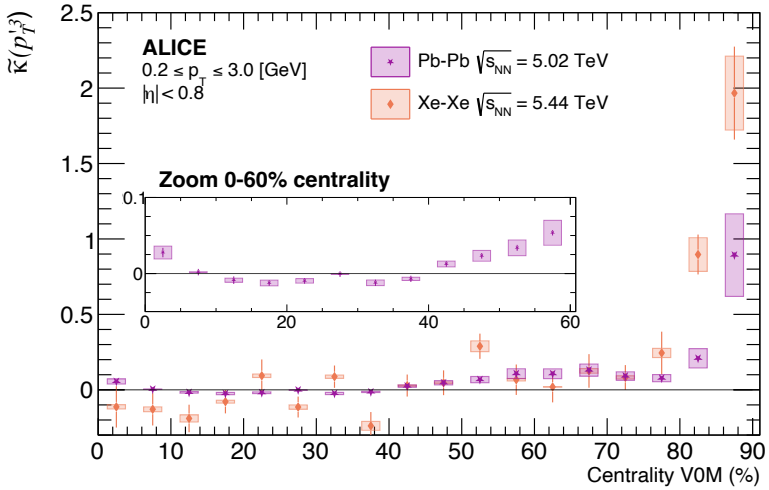

Figure 5.15: Measurements of $\widetilde{\kappa}(p_T'^3)$ in Pb-Pb (purple star) collisions at $\sqrt{s_{NN}} = 5.02$ TeV, and Xe-Xe (orange diamond) collision at $\sqrt{s_{NN}} = 5.44$ TeV with filling representing the associated systematic uncertainties

In higher orders, the HIJING calculation is off by multiple factors and is therefore not included in the figure. In Pb-Pb collisions, a change in sign can be observed in the central regime, followed by an almost constant trend until the 40% centrality region. This change in trend could indicate a transition. It has been noted that only central to ultra-central collisions provide a clear snapshot of the nuclei, while for higher centrality, the nuclear shape plays a less significant role. In these cases, the interacting system behaves more like a large sample of binary collisions, independent of the nuclear structure, without any collectivity or Quark-Gluon Plasma (QGP) formation. As the impact parameter approaches zero, the energy density increases and the system starts to thermalize into a confined high-density region, namely the QGP. In this regime, the binary collisions can be considered as small background perturbations to the overall system. This explains the decrease in the magnitude of transverse momentum fluctuations as the collision becomes more central. Although direct evidence of accessing the nuclear structure at the LHC was not provided in this thesis, it has been demonstrated that the novel method of standardized cumulants $\widetilde{\kappa}(p_T'^m)$ has the potential to provide more precise studies in the future. This would require additional statistics, investigation of additional collision systems, and a comprehensive study of transverse momentum fluctuations in ultra-relativistic heavy-ion collisions. The additional system could provide more variation in the nuclei composition, where the ratio of neutrons and protons in the nuclei might course a noticeable effect. As additional deformed systems are taken into account, it could also be possible to observe common effects and even probe higher multi pole moments β_n in the nuclei.

6 Conclusion

The primary objective of this thesis was to investigate the influence of different nuclear shapes on the final $\langle p_T \rangle$ spectrum and determine if these effects can be observed in ultra-relativistic heavy-ion collisions at the LHC. To achieve this, a novel approach utilizing higher-order standardized cumulants of transverse momentum fluctuations, denoted as $\widetilde{\kappa}(p_T'^m)$, was proposed to analyze initial conditions, including nuclear shape. Extensive Monte Carlo studies were conducted to understand the physical significance of the standardized cumulant method. The thesis presents the first ALICE measurements of standardized cumulants $\widetilde{\kappa}(p_T'^1)$ and $\widetilde{\kappa}(p_T'^3)$, with NUE correction, in both Pb-Pb and Xe-Xe collisions at $\sqrt{s_{NN}} = 5.02$ TeV and $\sqrt{s_{NN}} = 5.44$ TeV, respectively. Furthermore, a framework was developed to allow for the analysis of arbitrary orders. However, due to limited statistical data in Xe-Xe collisions, it was not possible to find accurate evidence for nuclear deformation of the nuclei in the current collision system at the LHC.

Simulations using the AMPT model have been performed for ^{129}Xe collisions with different deformations, and the measurements of $\widetilde{\kappa}(p_T'^3)$ indicated sensitivity to both deformation strength β_2 and triaxiality γ. However, obtaining precise information from standardized cumulant ratios would require an exact reference nucleus with known structure constants, which is currently not available. Additionally, HIJING calculations were conducted to examine sub-event p_T fluctuations in Monte Carlo simulations of Pb-Pb collisions at $\sqrt{s_{NN}} = 5.02$ TeV. The analysis revealed the suppression of non-flow effects and a potential saturation point when applying a gap of $|\Delta\eta| < 0.4$. However, the method did not yield meaningful results when applied to real data and was excluded from the final analysis.

The HIJING calculations also revealed unexpected responses to the choice of momentum range for particle selection, in the standardized cumulants. While regular cumulants exhibited expected behavior, the process of standardization introduced new phenomena that are not yet fully understood. This prompted the extension of the study to Pb-Pb collisions at the LHC, where distinct and contrasting dynamics were observed in applying different p_T ranges. These measurements could potentially capture the transition from the dominant contribution of soft and hard processes as a function of centrality. The increased fluctuations observed in peripheral collisions further enhance our understanding of the collectivity associated with the created Quark-Gluon Plasma (QGP). The energy density decreases as the nuclei move apart, reducing the probability of QGP formation. Therefore, observing a reduction in fluctuations as collisions become more central indicates an increased probability of QGP formation. This suggests that the created system's energy spectrum becomes dominant, while any independent background collision does not significantly influence the fluctuation in the QGP. Considering the current results, it is reasonable to attempt to decompose the cumulant into various components encountered throughout the collision, from the initial nuclear structure to the final passage through matter in the detector:

$$\text{Nuclear Shape} \rightarrow \text{IC} \rightarrow \text{QGP} \rightarrow \text{Final interaction} \rightarrow \widetilde{\kappa}(p_T'^m)$$

While physically deconstructing all these components is currently not possible, it is feasible to test some of them step-by-step through simulations.

While this thesis has primarily focused on the effect of quadrupole deformation, it is evident that other interesting observables can also be studied. One such example is the study of surface diffusion, as introduced in Equation 1.3, which is of great interest for investigating the neutron skin and halo effect [68]. Though, given the multitude of observables and unknown effects that are present in the p_T spectrum, it is crucial to first gain a precise understanding of transverse momentum fluctuations for lower orders, denoted as $\widetilde{\kappa}(p_T'^m)$, before progressing further. By doing so, we can advance our understanding and address the remaining challenges in this field. Perhaps then, standardized cumulants of mean transverse momentum fluctuations may provide a means to probe the nuclear structure in high-energy collisions.

References

[1] A. Zee. *Quantum Field Theory in a Nutshell*. Princeton University Press, 2010. ISBN: 978-0-691-14034-6.

[2] Robert H. Swendsen. *An Introduction to Statistical Mechanics and Thermodynamics*. Oxford University Press, 2012. ISBN: 978–0–19–964694–4.

[3] Maurice Goldhaber. "A Closer look at the elementary fermions". In: *Proc. Nat. Acad. Sci.* **99** (2002). arXiv: hep-ph/0201208.

[4] Graham Shaw Brian R. Martin. *Nuclear and Particle Physics - An Introduction*. Wiley, 2019. ISBN: 978-1-119-34461-2.

[5] Michael F. "Chapter 10 - Neutron Radiation". In: *Radioactivity (Second Edition)*. Ed. by Michael F. L'Annunziata. Second Edition. Elsevier, 2016. ISBN: 978-0-444-63489-4.

[6] Mark Thomson. *Modern Particle Physics*. Cambridge University Press, 2013. ISBN: 9781139525367.

[7] Douglas Ross Alexander Belyaev. *Nuclear and Particle Physics - An Introduction*. Springer Cham, 2021. ISBN: 978-3-030-80116-8.

[8] **CMS** Collaboration. "Measurement and QCD analysis of double-differential inclusive jet cross sections in pp collisions at $\sqrt{s_{NN}} = 8$ TeV and cross section ratios to 2.76 and 7 TeV". In: *Journal of High Energy Physics* **2017**. no. 3, (Mar. 2017).

[9] A. Bazavov et a. "Equation of state in". In: *Physical Review D* **90**. no. 9, (Nov. 2014).

[10] U. Heinz et al. "The viscosity of quark-gluon plasma at RHIC and the LHC". In: *AIP Conference Proceedings*. AIP, 2012.

[11] E. Iancu. "QCD in heavy ion collisions". In: (2012). arXiv: 1205.0579 [hep-ph].

[12] **ALICE** Collaboration. "Characterizing the initial conditions of heavy-ion collisions at the LHC with mean transverse momentum and anisotropic flow correlations". In: *Physics Letters B* **834** (Nov. 2022).

[13] J. Albacete. "CGC and initial state effects in Heavy Ion Collisions". In: *Journal of Physics: Conference Series* **270** (Jan. 2011).

[14] B. Schenke et al. "Features of the IP-Glasma". In: *Nuclear Physics A* **982** (Feb. 2019).

[15] B. Schenke et al. "Fluctuating Glasma Initial Conditions and Flow in Heavy Ion Collisions". In: *Physical Review Letters* **108**. no. 25, (June 2012).

[16] G. Giuliano et al. "Correlation between mean transverse momentum and anisotropic flow in heavy-ion collisions". In: *Physical Review C* **103**. no. 2, (Feb. 2021).

[17] L. Morel et al. "Determination of the fine-structure constant with an accuracy of 81 parts per trillion". In: *Nature* **588**. no. 7836, (2020).

[18] V. K. B. Kota. *SU(3) Symmetry in Atomic Nuclei*. Springer Singapore, 2020. ISBN: 978-981-15-3603-8.

[19] Aage Bohr: Rotational motion in nuclei, Nobel Lecture. Accessed 2023/12/03. https://www.nobelprize.org/uploads/2018/06/bohr-lecture-1.pdf.

[20] A. Ekstroem eta al. "What is ab initio in nuclear theory?" In: *Frontiers in Physics* **11** (Feb. 2023).

[21] Advances and challenges in the ab initio description of the nuclear many-body problem. https://resanet.in2p3.fr/?page_id=1163.

[22] A. Ali. "Shell Model for Study Quadrupole Transition Rates in B2 in Some Neon Isotopes in sd-shell with Using Different Interactions". In: *Journal of Astrophysics & Aerospace Technology* **06** (Jan. 2018).

[23] BN. Lu et al. "Potential energy surfaces of actinide and transfermium nuclei from multi-dimensional constraint covariant density functional theories". In: *EPJ Web of Conferences* **38** (Mar. 2013).

[24] J. Jia. "Probing triaxial deformation of atomic nuclei in high-energy heavy ion collisions". In: *Physical Review C* **105**. no. 4, (Apr. 2022).

[25] PV. Isacker et al. "Symmetries and deformations in the spherical shell model". In: *Physica Scripta* **91**. no. 2, (Jan. 2016).

[26] WRyssens et al. Evidence of Hexadecapole Deformation in Uranium-238 at the Relativistic Heavy Ion Collider. 2023. arXiv: 2302.13617 [nucl-th].

[27] W. Ryssens et al. "Skyrme-Hartree-Fock-Bogoliubov mass models on a 3D mesh: II. Time-reversal symmetry breaking". In: *The European Physical Journal A* **58**. no. 12, (Dec. 2022).

[28] CERN: The Large Hadron Collider. Accessed 2023/12/03. https://home.cern/science/accelerators/large-hadron-collider.

[29] Michaela et.al Schaumann. "First Xenon-Xenon Collisions in the LHC". In: (2018). URL: https://cds.cern.ch/record/2648699.

[30] CERN: ATLAS (A Toroidal LHC Apparatus). Accessed 2023/13/03. https://home.cern/science/experiments/atlas.

[31] CERN: CMS (Compact Muon Solenoid). Accessed 2023/13/03. https://home.cern/science/experiments/cms.

[32] CERN: LHCb (Large Hadron Collider beauty). Accessed 2023/13/03. https://home.cern/science/experiments/lhcb.

[33] CERN: ALICE (A Large Ion Collider Experiment). Accessed 2023/13/03. https://home.cern/science/experiments/alice.

[34] S. Kaiser et. al. "Search for the Higgs Boson in the Process pp to Hqq, H WW with the ATLAS Detector". In: (Mar. 2023).

[35] **ALICE** Collaboration. Accessed 2023/15/03. https://alice-collaboration.web.cern.ch/.

[36] **ALICE** Collaboration. "The alice experiment at the CERN LHC". In: *Journal of Instrumentation* **3** (Aug. 2008).

[37] P. Braun-Munzinger et. al. "Loosely-bound objects produced in nuclear collisions at the LHC". In: *Nuclear Physics A* **987** (Apr. 2019).

[38] P. Kuijer. "The inner tracking system of the Alice experiment". In: *Nuclear Instruments and Methods in Physics Research Section A: Accelerators, Spectrometers, Detectors and Associated Equipment* **530** (2004).

[39] **ALICE** Collaboration et al. *ALICE: Technical design report of the time projection chamber*. 2000.

[40] P. Cortese et. al. *ALICE forward detectors: FMD, TO and VO: Technical DesignReport*. Technical design report. ALICE. Geneva: CERN, 2004.

[41] A.Bilandzic. "Anisotropic flow measurements in ALICE at the large hadron collider". Thesis at CERN. 2012.

[42] Christian Bierlich et al. "Confronting experimental data with heavy-ion models: Rivet for heavy ions". In: *The European Physical Journal C* **80**. no. 5, (May 2020).

[43] P. Braun-Munzinger et al. "Loosely-bound objects produced in nuclear collisions at the LHC". In: *Nuclear Physics A* **987** (Apr. 2019).

[44] G. Giacalone et al. "Skewness of mean transverse momentum fluctuations in heavy-ion collisions". In: *Phys Rev* **C103**. no. 2, (Feb. 2021).

[45] N.G. Van Kampen. "Chapter II - RANDOM EVENTS". In: *Stochastic Processes in Physics and Chemistry*. Third Edition. Amsterdam: Elsevier, 2007.

[46] N. Borghini et al. "New method for measuring azimuthal distributions in nucleus-nucleus collisions". In: *Phys Rev* **C63**. no. 5, (2001).

[47] J. Cimerman et al. "Anisotropic flow decorrelation in heavy-ion collisions at RHIC-BES energies with 3D event-by-event viscous hydrodynamics". In: (2021). arXiv: 2110.05578 [nucl-th].

[48] R. Snellings. "Collective expansion at the LHC: selected ALICE anisotropic flow measurements". In: *Journal of Physics G: Nuclear and Particle Physics* **41**. no. 12, (Nov. 2014).

[49] A. Bilandzic et al. "Flow analysis with cumulants: Direct calculations". In: *Physical Review C* **83**. no. 4, (Apr. 2011).

[50] N. Borghini et al. "New method for measuring azimuthal distributions in nucleus-nucleus collisions". In: *Physical Review C* **63**. no. 5, (Apr. 2001).

[51] A. Bilandzic et al. "Generic framework for anisotropic flow analyses with multiparticle azimuthal correlations". In: *Physical Review C* **89**. no. 6, (June 2014).

[52] **STAR**Collaboration. "Incident energy dependence of pt correlations at relativistic energies". In: *Physical Review C* **72**. no. 4, (Oct. 2005).

[53] S. Bhatta et al. "Higher-order transverse momentum fluctuations in heavy-ion collisions". In: *Physical Review C* **105**. no. 2, (Feb. 2022).

[54] Ulrich W. Heinz. Concepts of Heavy-Ion Physics. 2004. arXiv: hep-ph/0407360 [hep-ph].

[55] K. Gajdosova. "Investigations of collectivity in small and large collision systems at the LHC with ALICE". Presented 23 Aug 2018. 2018.

[56] R. Kubo. "Generalized Cumulant Expansion Method". In: *Journal of the Physical Society of Japan* **17**. no. 7, (1962).

[57] P. Smith. "A Recursive Formulation of the Old Problem of Obtaining Moments from Cumulants and Vice Versa". In: *The American Statistician* **49**. no. 2, (1995).

[58] **ALICE** Collaboration AliPhysics github. Accessed 2023/08/04. https://github.com/alisw/AliPhysics.

[59] S. Agostinelli et al. "GEANT4. A Simulation toolkit". In: *Nucl. Instrum. Methods Phys. Res., A* **506**. no. 3, (2003).

[60] K. Singh et al. "Bootstrap Method". In: *International Encyclopedia of Education (Third Edition)*. Ed. by Penelope Peterson, Eva Baker, and Barry McGaw. Third Edition. Oxford: Elsevier, 2010. ISBN: 978-0-08-044894-7.

[61] A. Pandav et al. "Effect of limited statistics on higher order cumulants measurement in heavy-ion collision experiments". In: *Nuclear Physics A* **991** (Nov. 2019).

[62] Roger Barlow. Systematic Errors: facts and fictions. 2002.

[63] XN. Wang et al. "HIJING: A Monte Carlo model for multiple jet production in p p, p A and A A collisions". In: *Phys. Rev. D* **44** (1991).

[64] R. Andrade et al. "Importance of Granular Structure in the Initial Conditions for the Elliptic Flow". In: *Physical Review Letters* **101**. no. 11, (Sept. 2008).

[65] ZW. Lin et al. "Multiphase transport model for relativistic heavy ion collisions". In: *Physical Review C* **72**. no. 6, (Dec. 2005).

[66] B Bally et al. "Evidence of the Triaxial Structure of". In: *Physical Review Letters* **128**. no. 8, (Feb. 2022).

[67] G. Giacalone. "Observing the Deformation of Nuclei with Relativistic Nuclear Collisions". In: *Physical Review Letters* **124**. no. 20, (May 2020).

[68] B. Hu. "Ab initio predictions link the neutron skin of 208Pb to nuclear forces". In: *Nature Physics* **18**. no. 10, (Aug. 2022).

[69] R. Workman et al. "Review of Particle Physics". In: *PTEP* **2022** (2022).

[70] ZW Lin et al. "Multiphase transport model for relativistic heavy ion collisions". In: *Physical Review C* **72**. no. 6, (Dec. 2005).

A Efficiency correction for transverse momentum

In section 3 the procedure to obtain efficiency correction by Monte-Carlo simulation where obtained. The section includes the remaining NUE as used for each systematic check in this thesis. On the right is the NUE as for weighting of the particles. The right side contain the ratio between default and systematic variation. The collision system and the anchored period is listed on each figure.

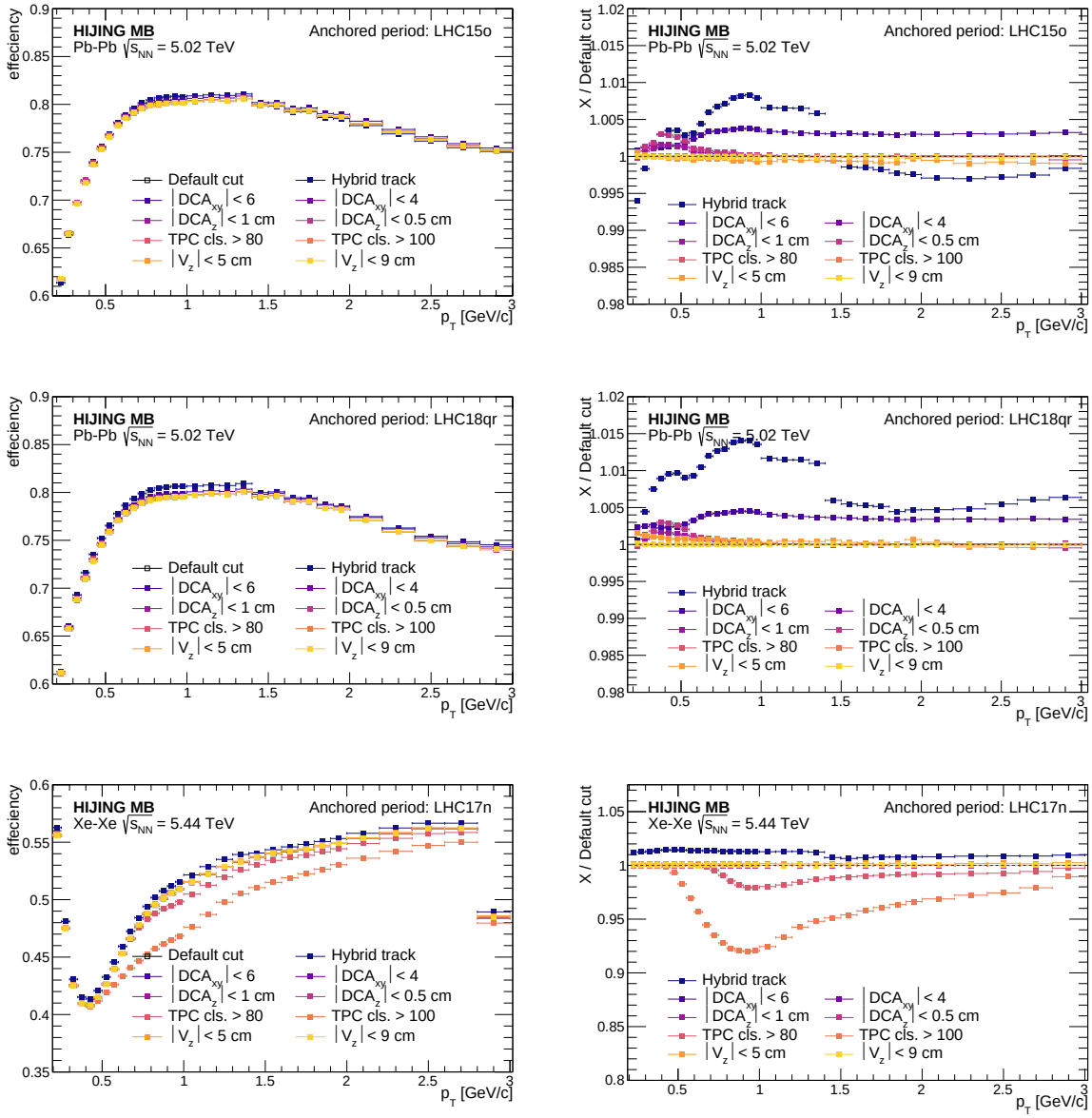

Figure A.1: Left: Efficiency for Pb-Pb and Xe-Xe as obtained with different systematics cut. Right: Change of efficiency with respect to the default cut used as outlined under Event selection and Track selection.

B Transverse momentum fluctuations

B.1 HIJING - Non-collective responses

As there where not found any advantage in using higher order cumulants in the HIJING model, most of the observables are presented here as reference. This include up to eight order cumulants and standardized cumulants.

Cumulants $\kappa(p_T^{lm})$ response to momentum range

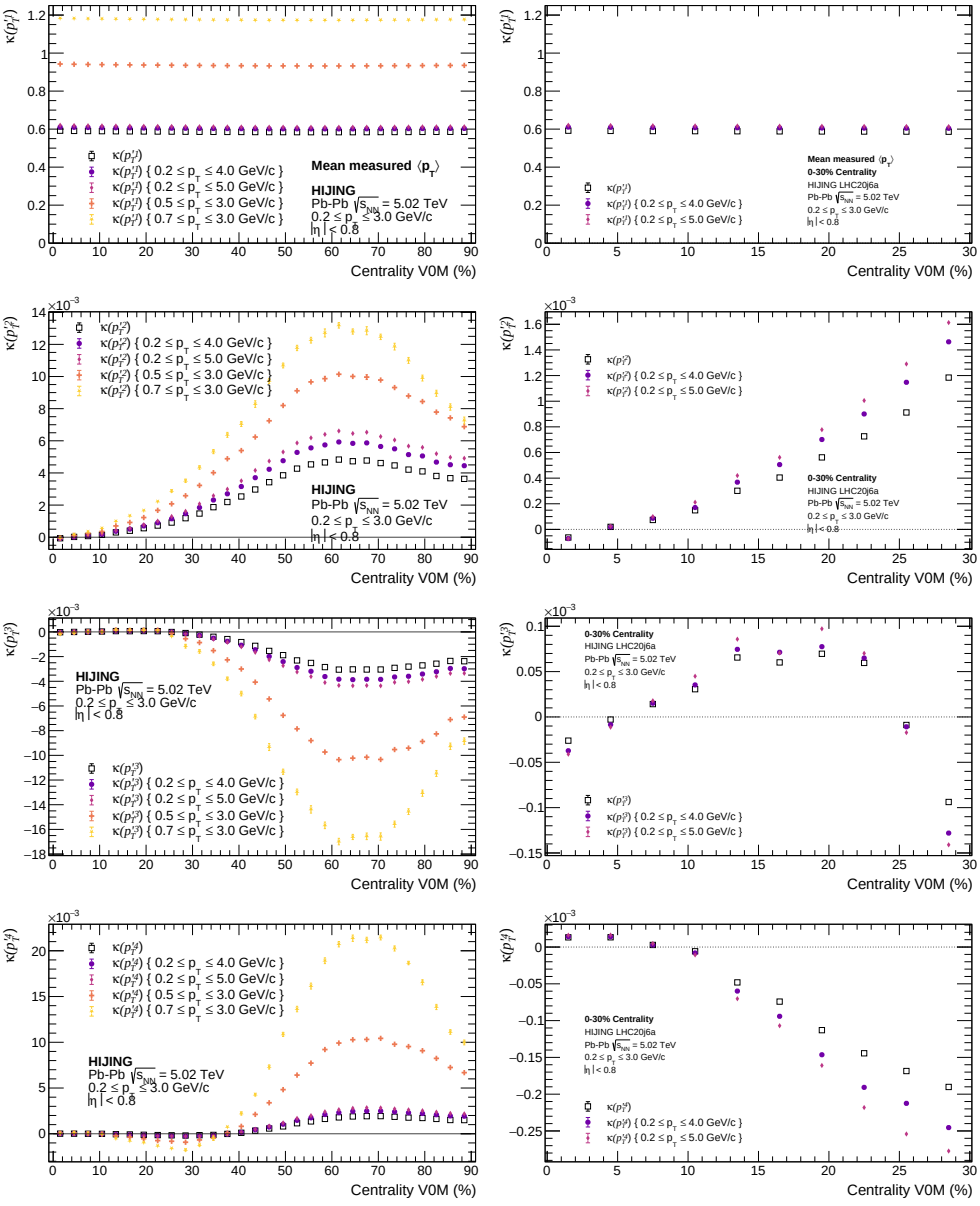

Figure B.1

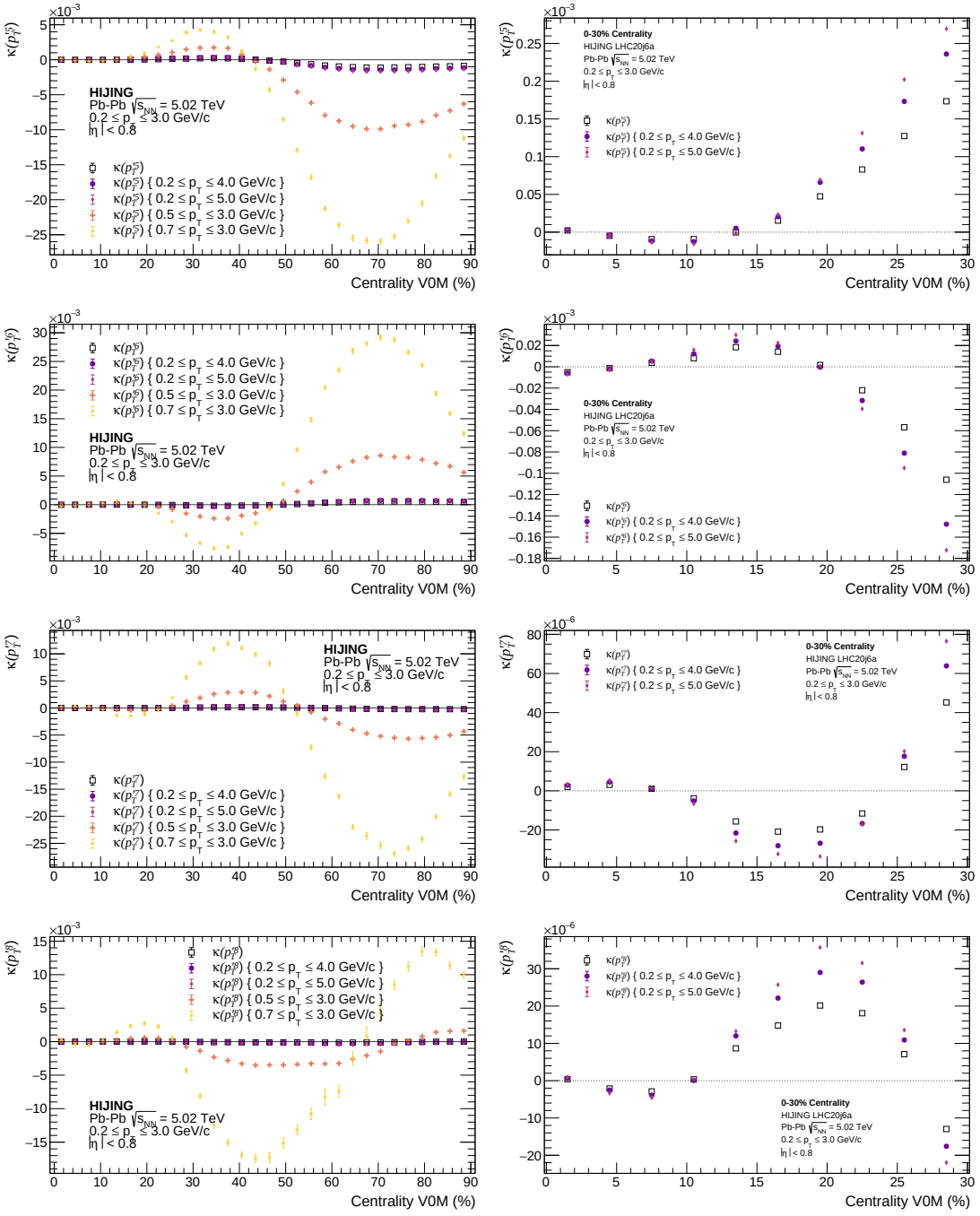
HIJING
Pb-Pb √s_NN = 5.02 TeV
0.2 ≤ p_T ≤ 3.0 GeV/c
|η| < 0.8
κ(p_T^5)
κ(p_T^5) { 0.2 ≤ p_T ≤ 4.0 GeV/c }
κ(p_T^5) { 0.2 ≤ p_T ≤ 5.0 GeV/c }
κ(p_T^5) { 0.5 ≤ p_T ≤ 3.0 GeV/c }
κ(p_T^5) { 0.7 ≤ p_T ≤ 3.0 GeV/c }
0-30% Centrality
HIJING LHC20j6a
Centrality V0M (%)
κ(p_T^6)
κ(p_T^6) { 0.2 ≤ p_T ≤ 4.0 GeV/c }
κ(p_T^6) { 0.2 ≤ p_T ≤ 5.0 GeV/c }
κ(p_T^6) { 0.5 ≤ p_T ≤ 3.0 GeV/c }
κ(p_T^6) { 0.7 ≤ p_T ≤ 3.0 GeV/c }
κ(p_T^7)
κ(p_T^7) { 0.2 ≤ p_T ≤ 4.0 GeV/c }
κ(p_T^7) { 0.2 ≤ p_T ≤ 5.0 GeV/c }
κ(p_T^7) { 0.5 ≤ p_T ≤ 3.0 GeV/c }
κ(p_T^7) { 0.7 ≤ p_T ≤ 3.0 GeV/c }
κ(p_T^8)
κ(p_T^8) { 0.2 ≤ p_T ≤ 4.0 GeV/c }
κ(p_T^8) { 0.2 ≤ p_T ≤ 5.0 GeV/c }
κ(p_T^8) { 0.5 ≤ p_T ≤ 3.0 GeV/c }
κ(p_T^8) { 0.7 ≤ p_T ≤ 3.0 GeV/c }

Figure B.2

High order $\kappa(p_T'^m)$ response

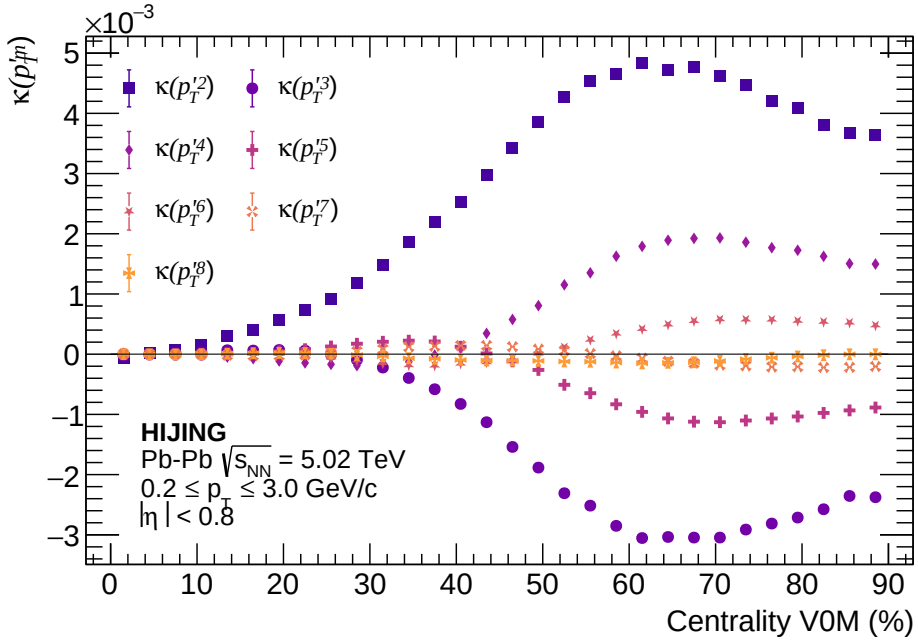

Figure B.3

Standardized cumulants $\widetilde{\kappa}(p_T^{\prime m})$ response to momentum

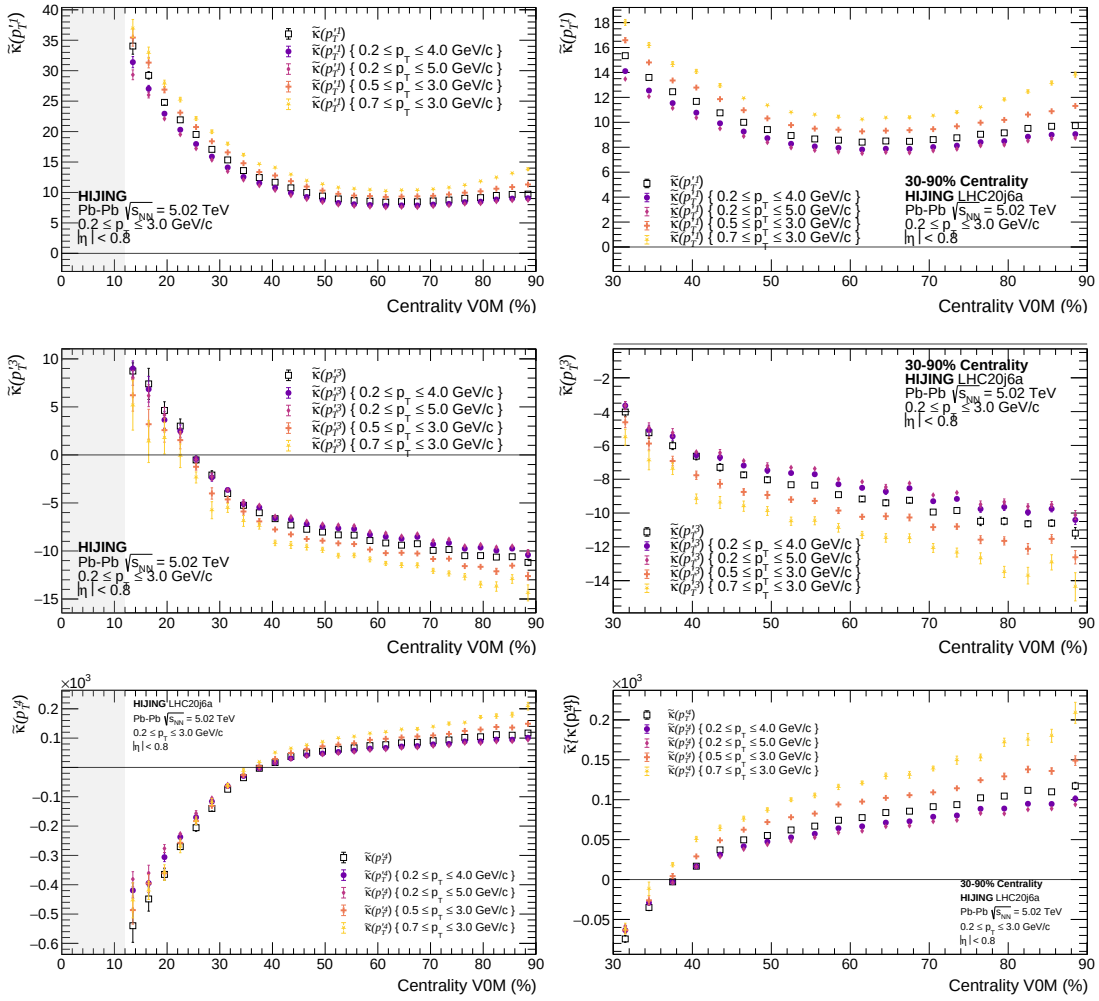

Figure B.4

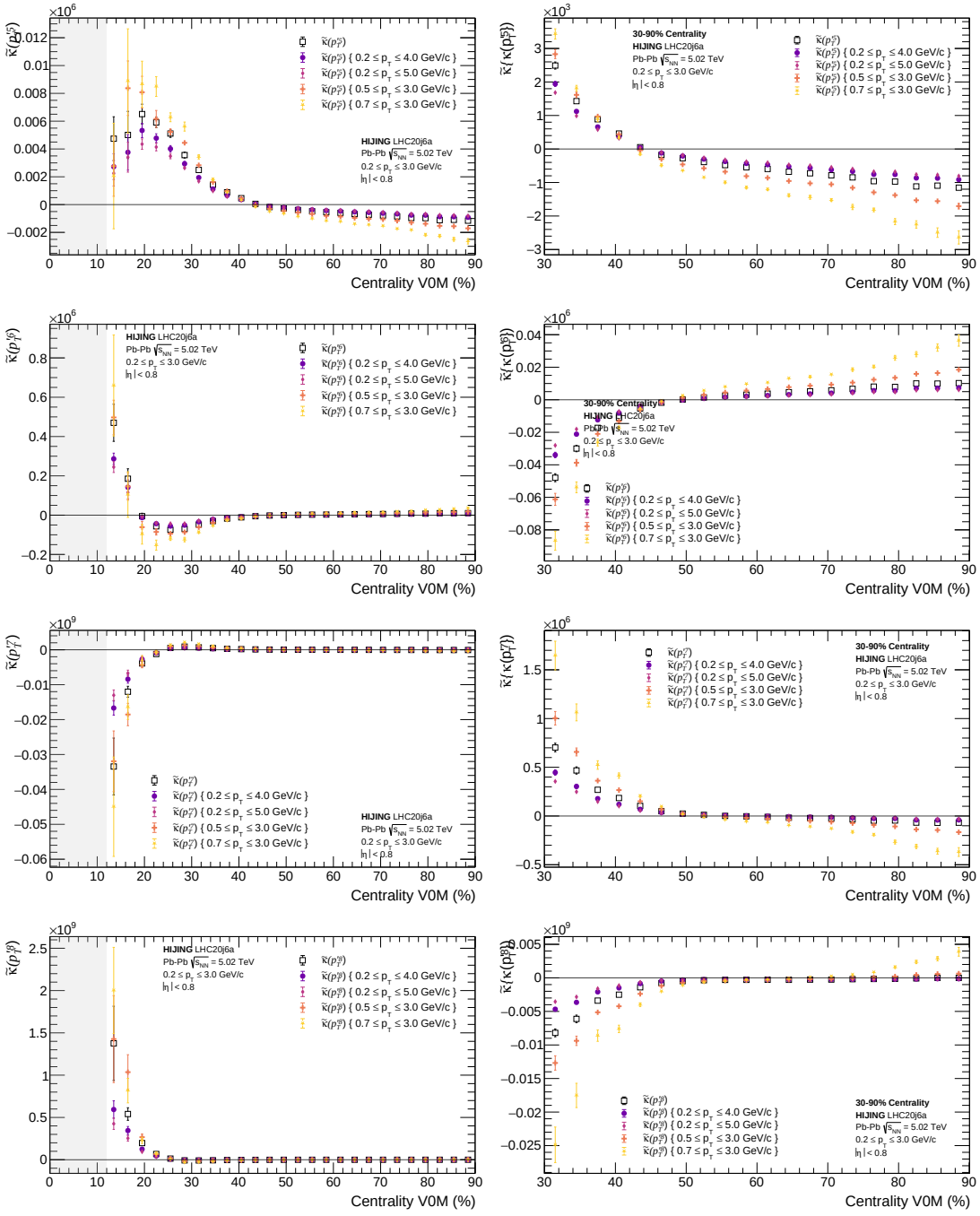
HIJING LHC20j6a
Pb-Pb $\sqrt{s_{NN}}$ = 5.02 TeV
0.2 ≤ p_T ≤ 3.0 GeV/c
|η| < 0.8
30-90% Centrality
Centrality V0M (%)
$\tilde{\kappa}(p_T^n)$
$\tilde{\kappa}(p_T^n)$ { 0.2 ≤ p_T ≤ 4.0 GeV/c }
$\tilde{\kappa}(p_T^n)$ { 0.2 ≤ p_T ≤ 5.0 GeV/c }
$\tilde{\kappa}(p_T^n)$ { 0.5 ≤ p_T ≤ 3.0 GeV/c }
$\tilde{\kappa}(p_T^n)$ { 0.7 ≤ p_T ≤ 3.0 GeV/c }

Figure B.5

B.2 AMPT (Default) - Collective response

This section outlines the higher order cumulants as calculated in the AMPT model with default configuration. As the the default version of AMPT is mostly outdated these results exist purly as reference. Unfortunately a cirect comparison of default AMPT and with string melting could not be presented in the scope of this thesis.

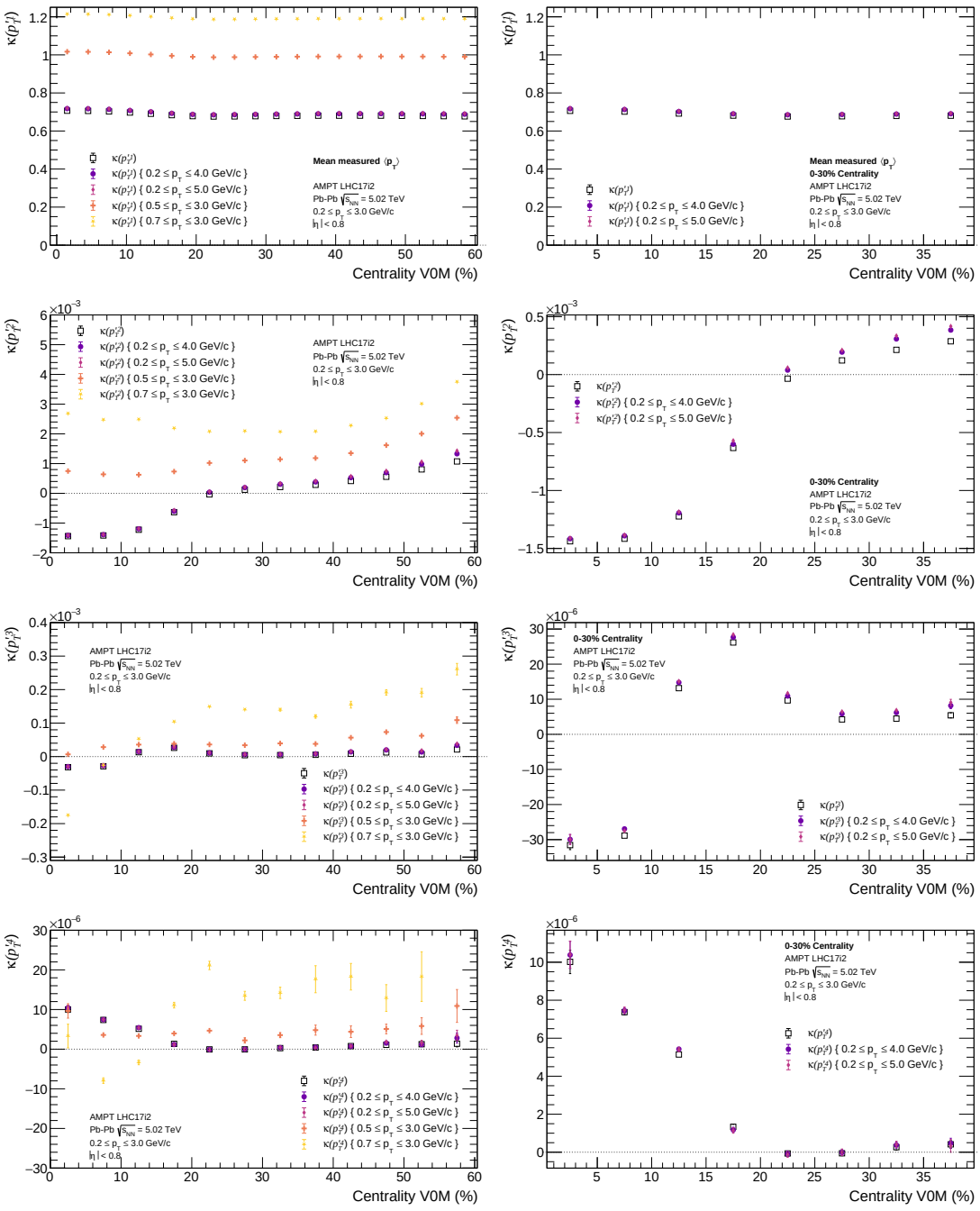

Figure B.6

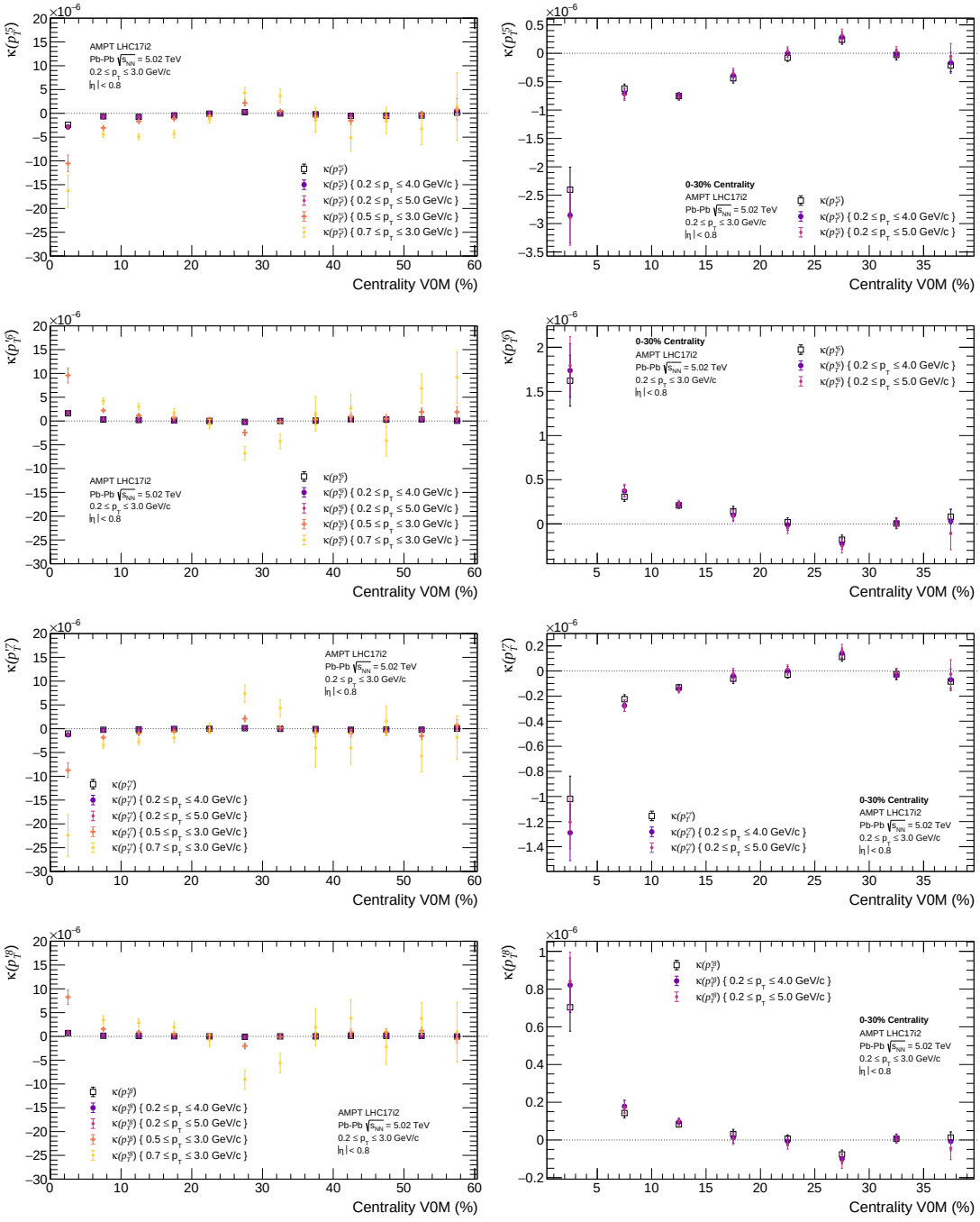
AMPT LHC17i2
Pb-Pb $\sqrt{s_{NN}}$ = 5.02 TeV
$0.2 \le p_T \le 3.0$ GeV/c
$|\eta| < 0.8$
0-30% Centrality
$\kappa(p_T^{ch})$
$\kappa(p_T^{ch})$ { $0.2 \le p_T \le 4.0$ GeV/c }
$\kappa(p_T^{ch})$ { $0.2 \le p_T \le 5.0$ GeV/c }
$\kappa(p_T^{ch})$ { $0.5 \le p_T \le 3.0$ GeV/c }
$\kappa(p_T^{ch})$ { $0.7 \le p_T \le 3.0$ GeV/c }
$\kappa(p_T^{\pi^+})$
$\kappa(p_T^{K^+})$
$\kappa(p_T^{p})$
$\kappa(p_T^{\pi^-})$
$\kappa(p_T^{K^-})$
$\kappa(p_T^{\bar{p}})$
Centrality V0M (%)

Figure B.7

Standardized cumulants $\widetilde{\kappa}(p_T^{\prime m})$ response to momentum

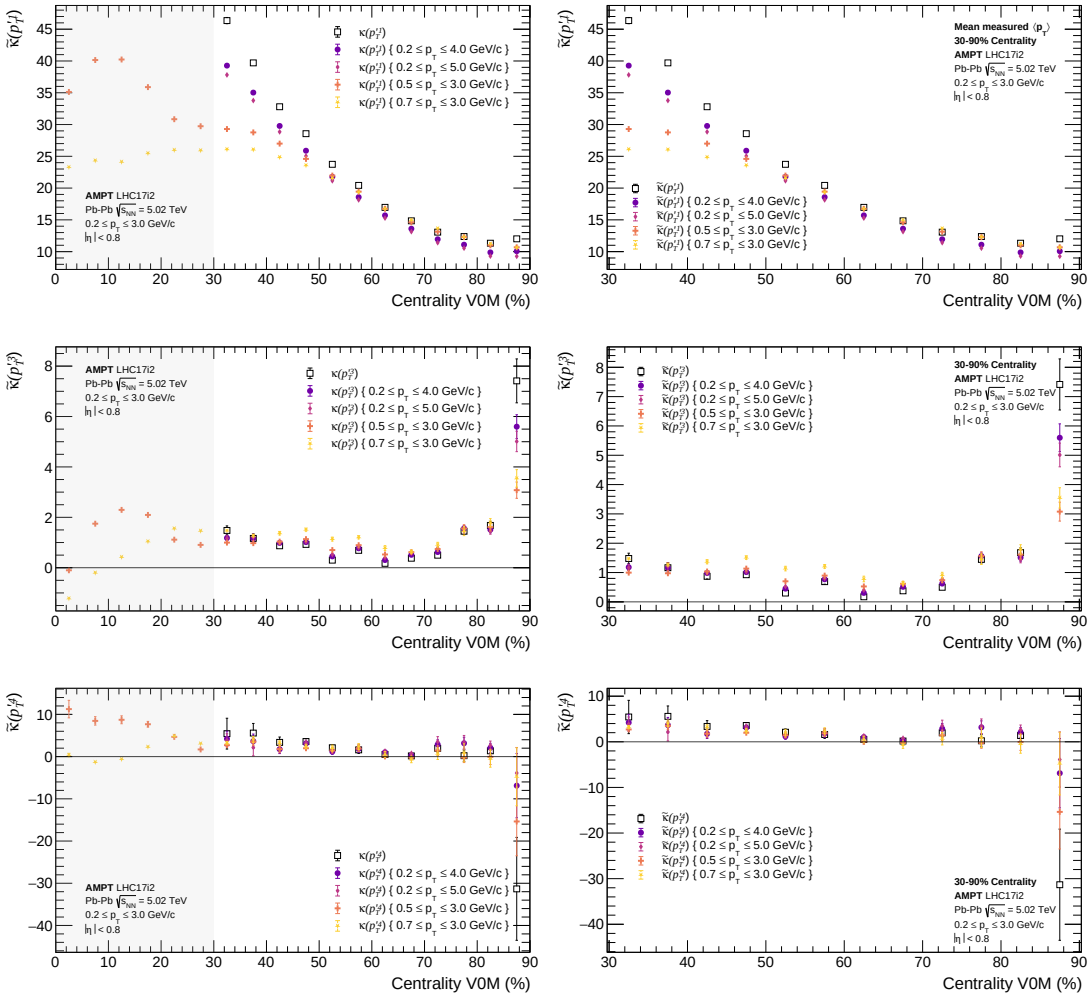

Figure B.8

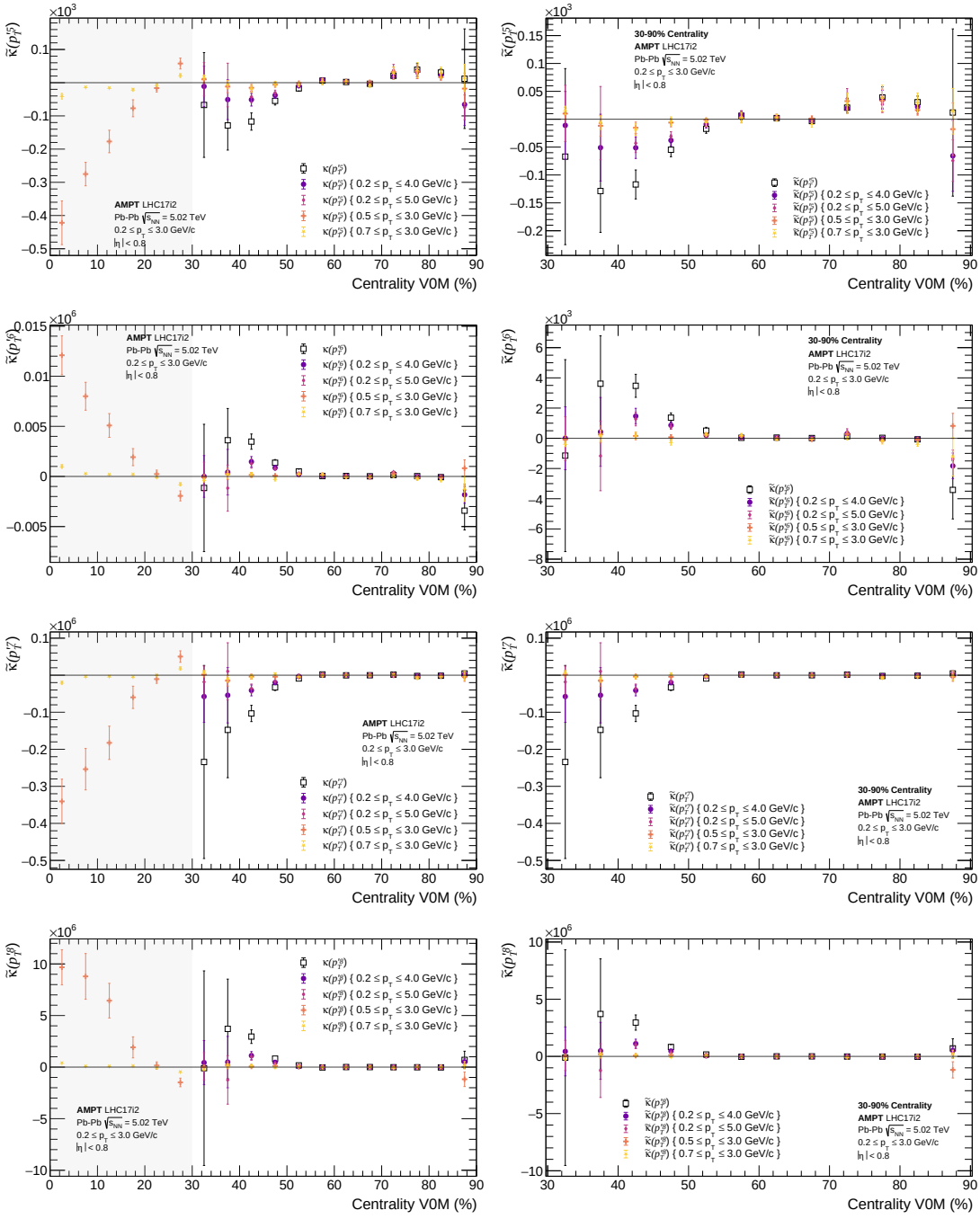
AMPT LHC17i2
Pb-Pb $\sqrt{s_{NN}}$ = 5.02 TeV
0.2 ≤ p_T ≤ 3.0 GeV/c
|η| < 0.8
30-90% Centrality
Centrality V0M (%)
$\kappa(p_T^{pp})$
$\kappa(p_T^{pp})$ { 0.2 ≤ p_T ≤ 4.0 GeV/c }
$\kappa(p_T^{pp})$ { 0.2 ≤ p_T ≤ 5.0 GeV/c }
$\kappa(p_T^{pp})$ { 0.5 ≤ p_T ≤ 3.0 GeV/c }
$\kappa(p_T^{pp})$ { 0.7 ≤ p_T ≤ 3.0 GeV/c }
$\kappa(p_T^{p\bar{p}})$
$\kappa(p_T^{\bar{p}\bar{p}})$
$\kappa(p_T^{K^+K^+})$
$\kappa(p_T^{K^-K^-})$
$\kappa(p_T^{K^+K^-})$
$\kappa(p_T^{\pi^+\pi^+})$
$\kappa(p_T^{\pi^-\pi^-})$
$\kappa(p_T^{\pi^+\pi^-})$

Figure B.9

B.3 Deformation response

Fits of all ratios. The current figures only carries the ratio to the spherical baseline $\beta_2 = 0.0$. Ratios with respect prolate nuclei are not reproduced as the only relevant figure has been presented on the thesis.

$\gamma = 0.$	$\widetilde{\kappa}(p_T'^1)$	$\widetilde{\kappa}(p_T'^3)$	$\widetilde{\kappa}(p_T'^4)$	$\widetilde{\kappa}(p_T'^5)$	$\widetilde{\kappa}(p_T'^6)$	$\widetilde{\kappa}(p_T'^7)$	$\widetilde{\kappa}(p_T'^8)$
χ^2/NDF	6.275.	2.206	1.073	1.341	1.095	1.215	1.335
f(0)	0.075	0.476	0.269	0.179	0.117	0.135	0.168

Table 7: Fit of $\gamma = 0$ standardized cumulants ratios with respect to spherical baseline. Listed with reduced χ^2

$\gamma = 27$	$\widetilde{\kappa}(p_T'^1)$	$\widetilde{\kappa}(p_T'^3)$	$\widetilde{\kappa}(p_T'^4)$	$\widetilde{\kappa}(p_T'^5)$	$\widetilde{\kappa}(p_T'^6)$	$\widetilde{\kappa}(p_T'^7)$	$\widetilde{\kappa}(p_T'^8)$
χ^2/NDF	2.873.	2.863	1.223	1.182	1.027	1.019	1.039
f(0)	3.183	1.013	0.086	0.082	0.07	0.102	0.118

Table 8: Fit of $\gamma = 27$ standerdized cumulants ratios with respect to spherical baseline. Listed with reduced χ^2

$\gamma = 60$	$\widetilde{\kappa}(p_T'^1)$	$\widetilde{\kappa}(p_T'^3)$	$\widetilde{\kappa}(p_T'^4)$	$\widetilde{\kappa}(p_T'^5)$	$\widetilde{\kappa}(p_T'^6)$	$\widetilde{\kappa}(p_T'^7)$	$\widetilde{\kappa}(p_T'^8)$
χ^2/NDF	2.545.	0.809	1.573	0.759	0.566	0.742	0.764
f(0)	4.015	4.997	0.111	0.108	0.139	0.163	0.167

Table 9: Fit of $\gamma = 60$ standerdized cumulants ratios with respect to spherical baseline. Listed with reduced χ^2

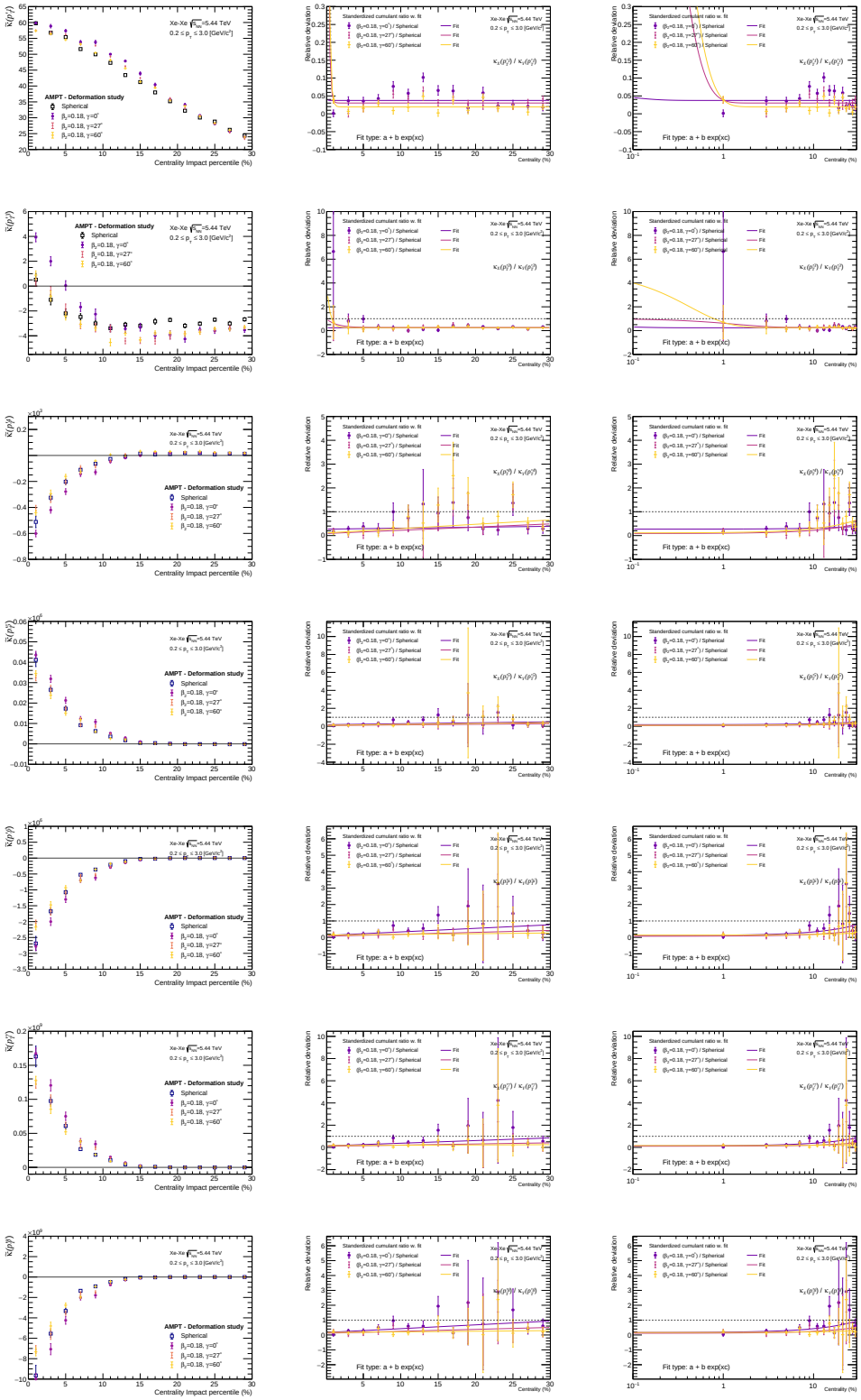
AMPT - Deformation study
Spherical
Xe-Xe $\sqrt{s_{NN}}$=5.44 TeV
0.2 ≤ p_T ≤ 3.0 [GeV/c]
Centrality Impact percentile (%)
Standardized cumulant ratio w. fit
Relative deviation
Fit type: a + b exp(xc)

Figure B.10

C Systematics checks

C.1 Systematics in Pb-Pb

C.2 Systematics for $\kappa(p_T'^2)$

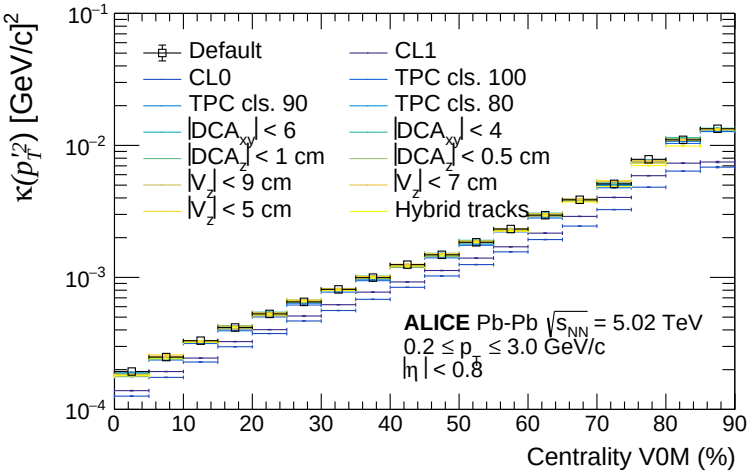

Figure C.1

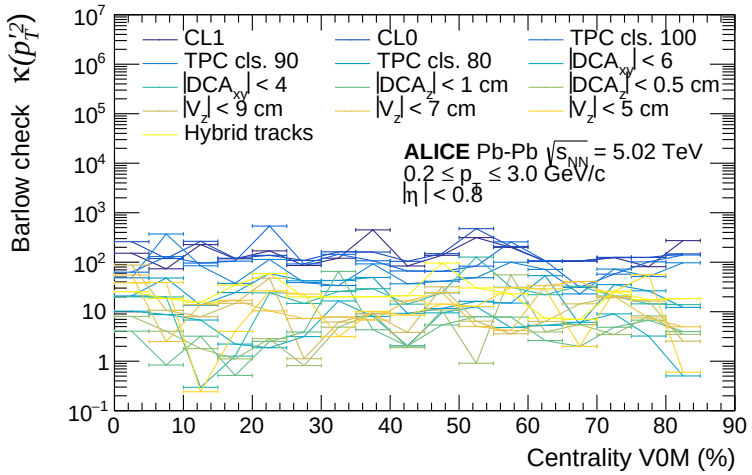

Figure C.2

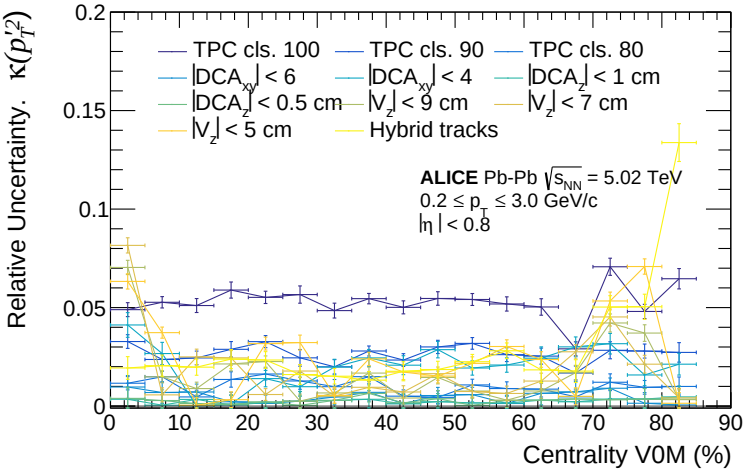

Figure C.3

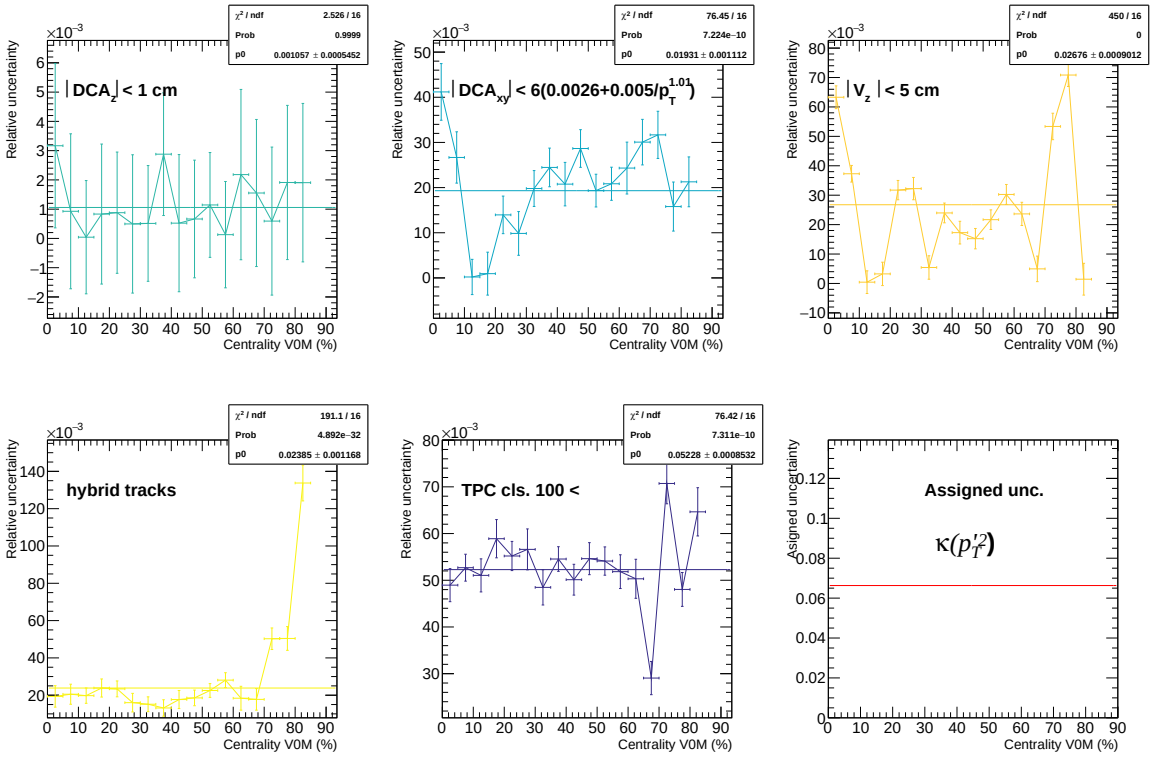

Figure C.4

Systematics for $\widetilde{\kappa}(p_T^{\prime 1})$

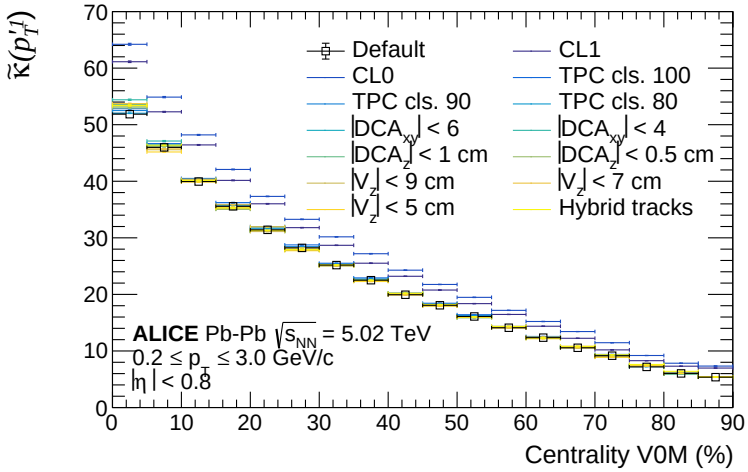

Figure C.5

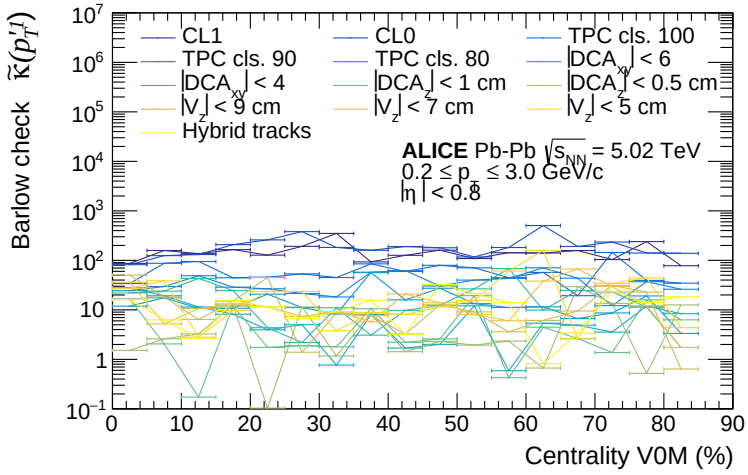

Figure C.6

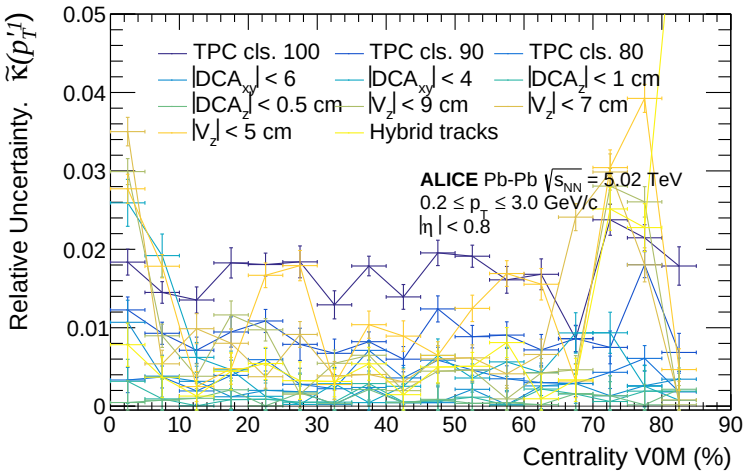

Figure C.7

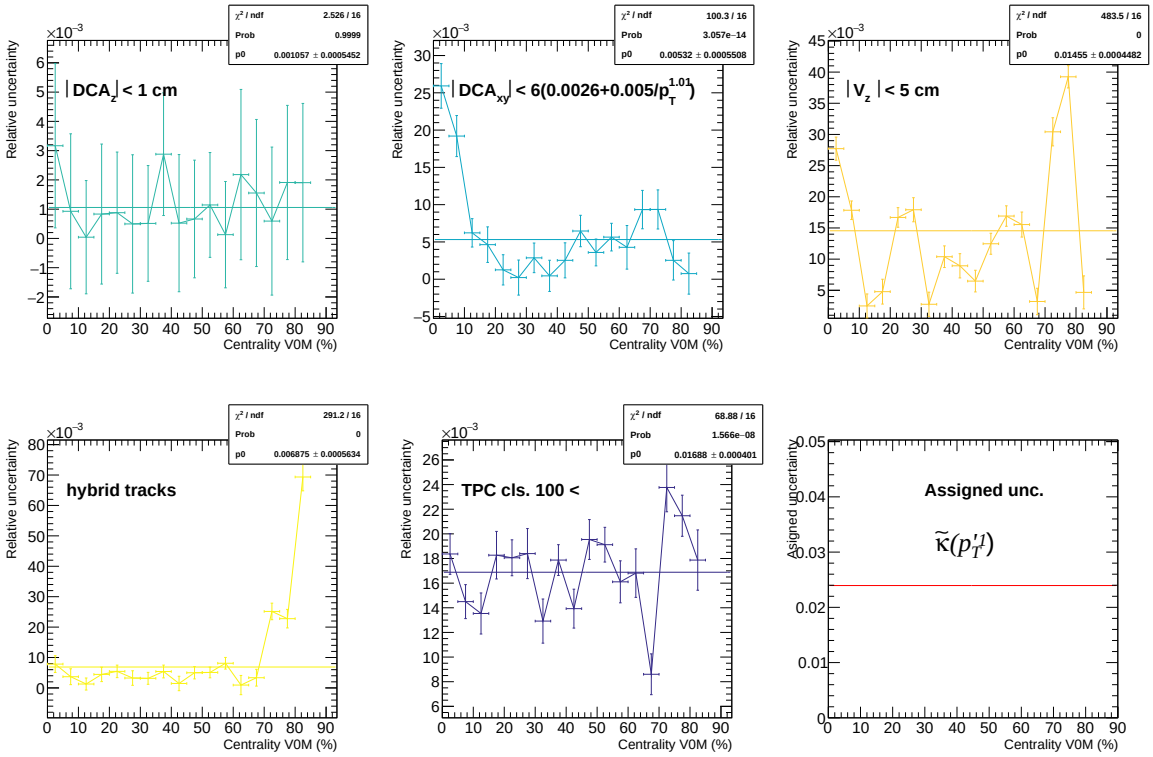

Figure C.8

Systematics for $\widetilde{\kappa}(p_T'^3)$

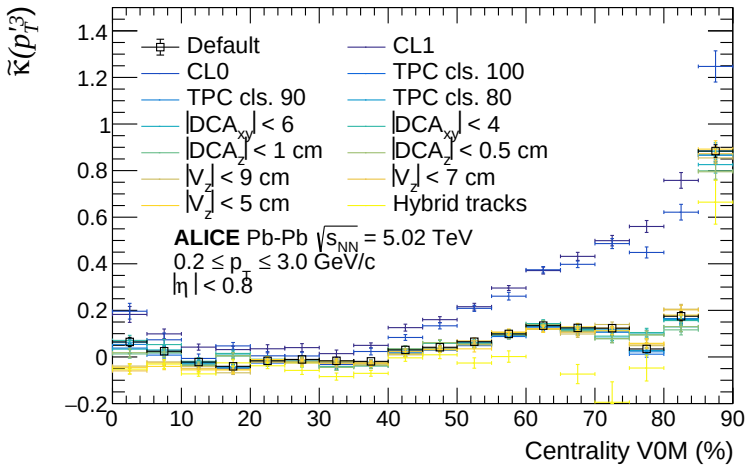

Figure C.9

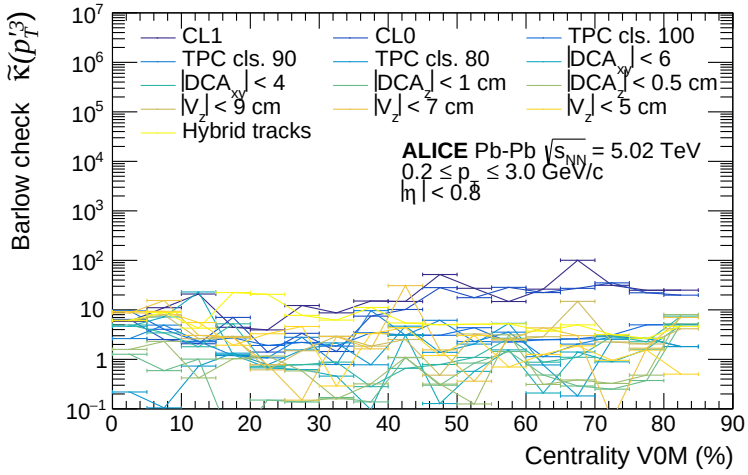

Figure C.10

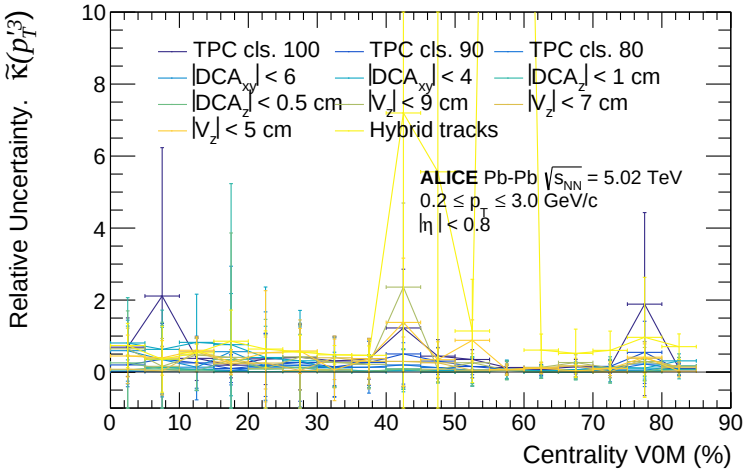

Figure C.11

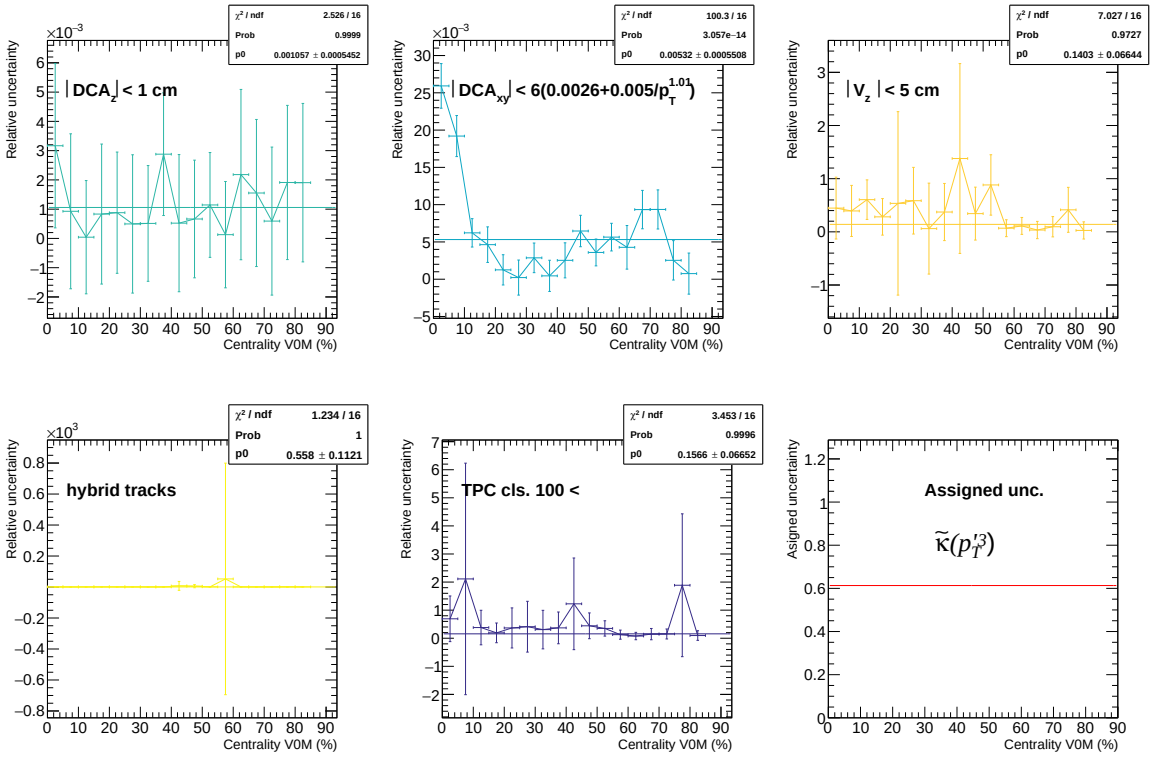

Figure C.12

C.3 Systematics in Xe-Xe

C.4 Systematics for $\kappa(p_T'^2)$

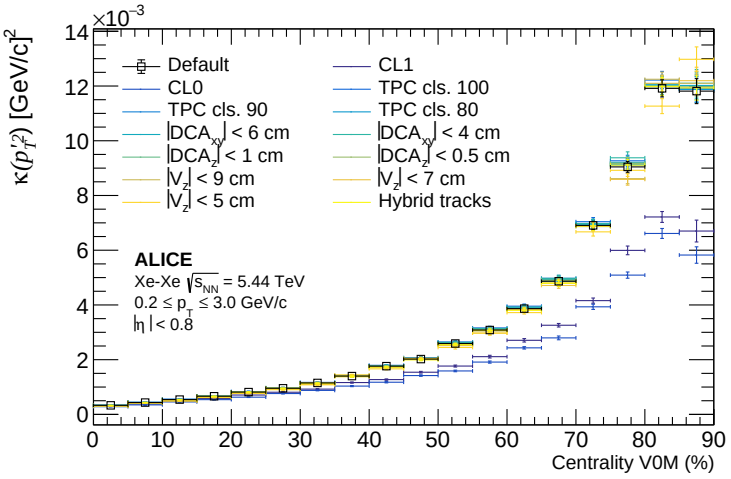

Figure C.13

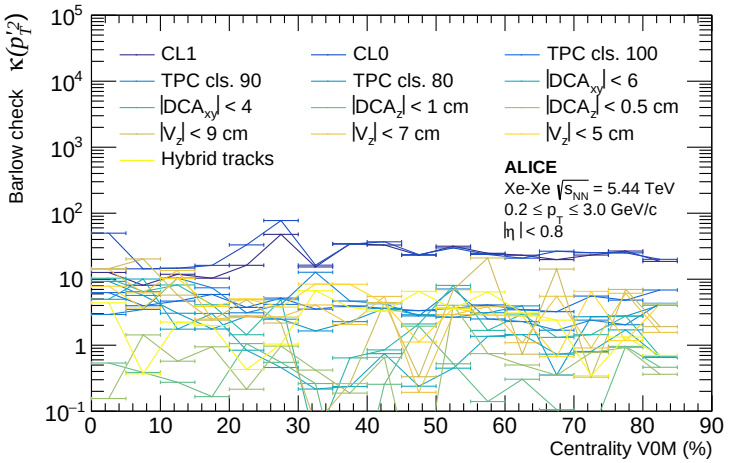

Figure C.14

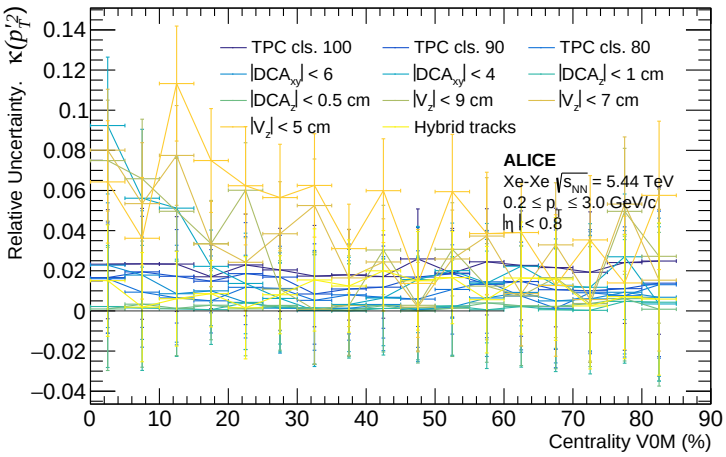

Figure C.15

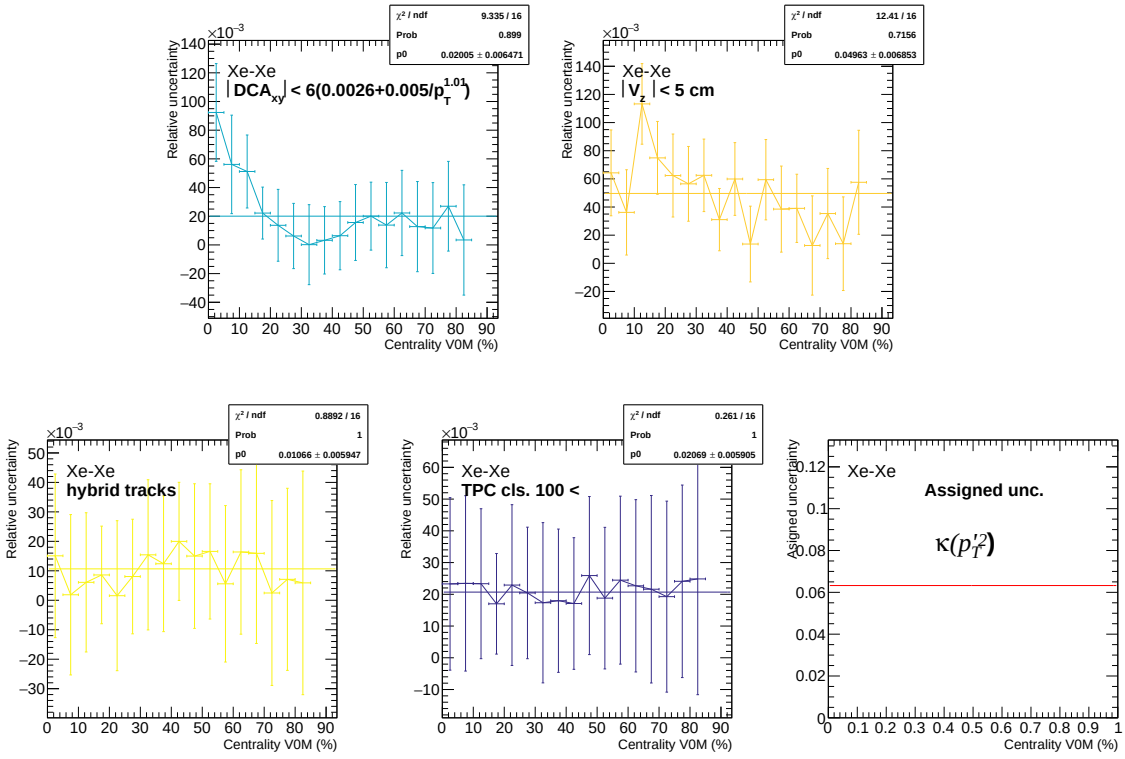

Figure C.16

Systematics for $\widetilde{\kappa}(p_T^{\prime 1})$

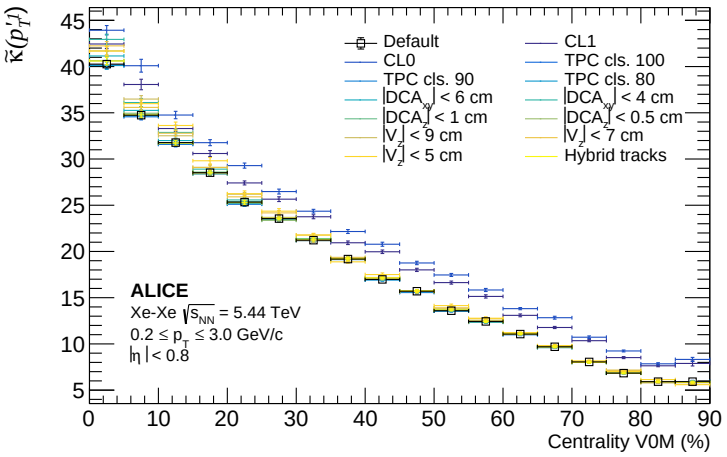

Figure C.17:]

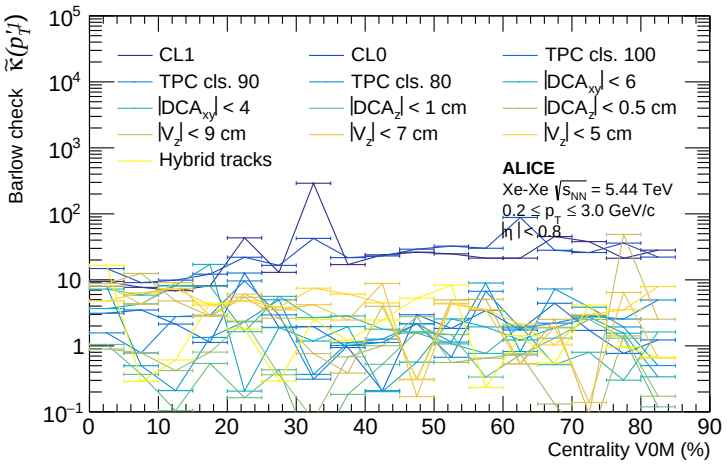

Figure C.18

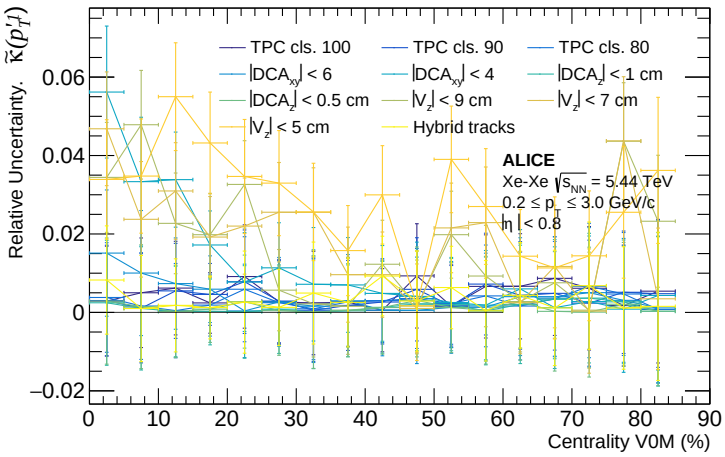

Figure C.19

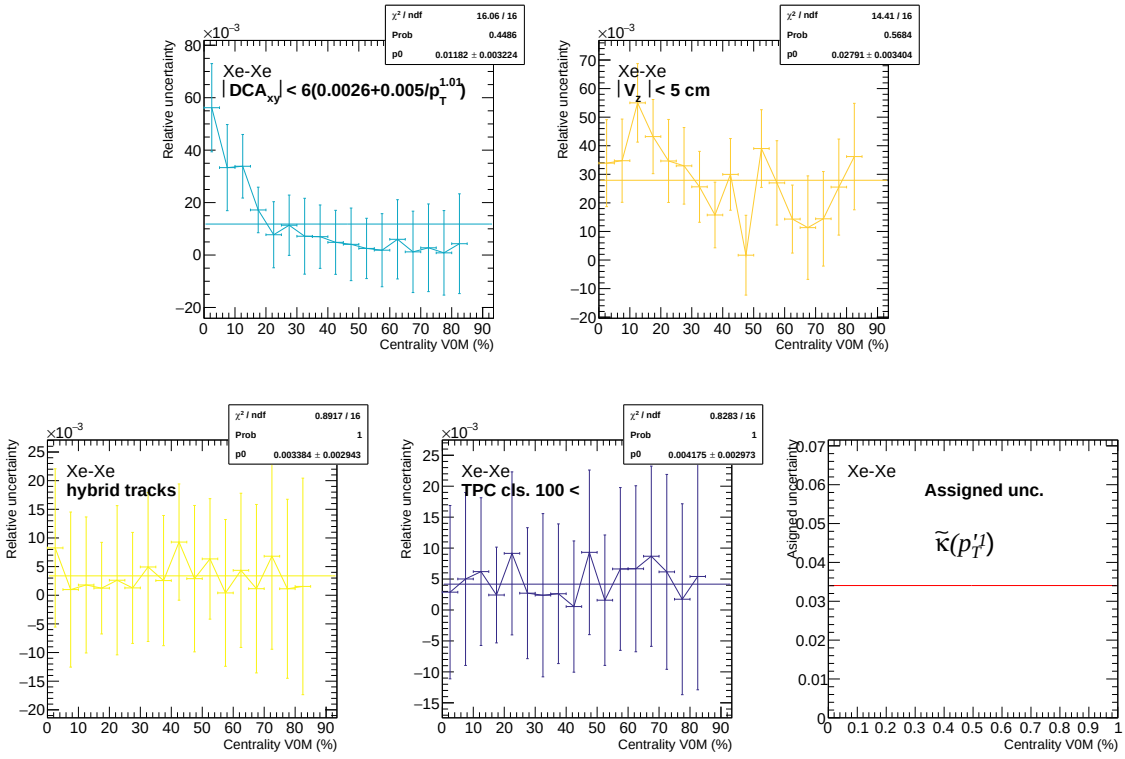

Figure C.20

Systematics for $\widetilde{\kappa}(p_T')$

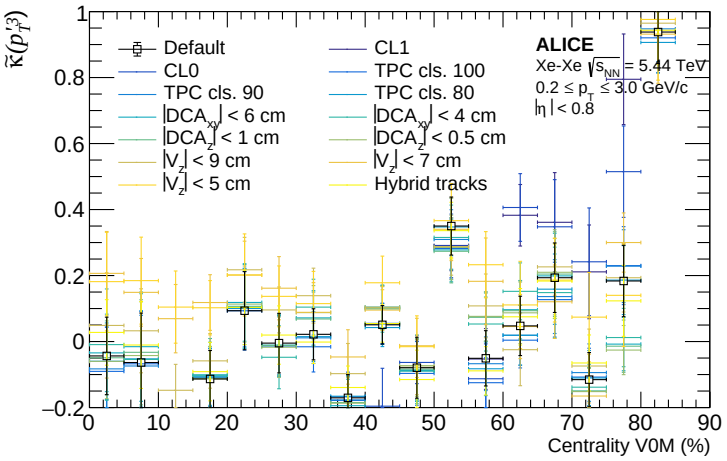

Figure C.21:]

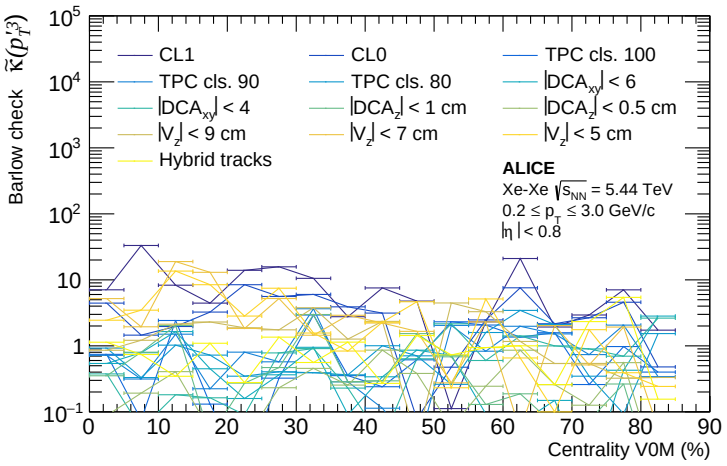

Figure C.22

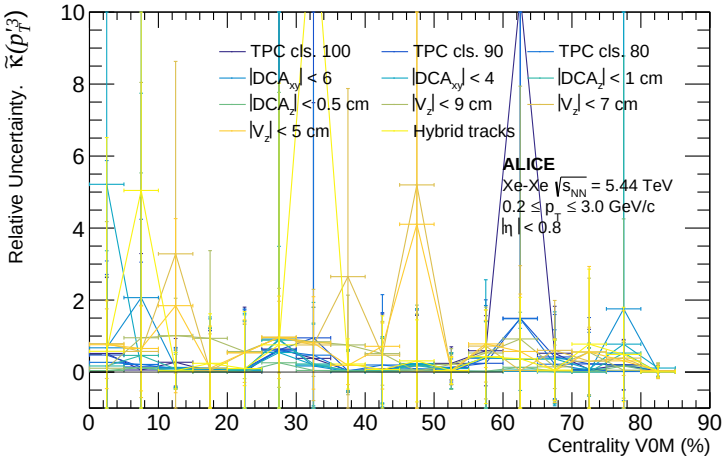

Figure C.23

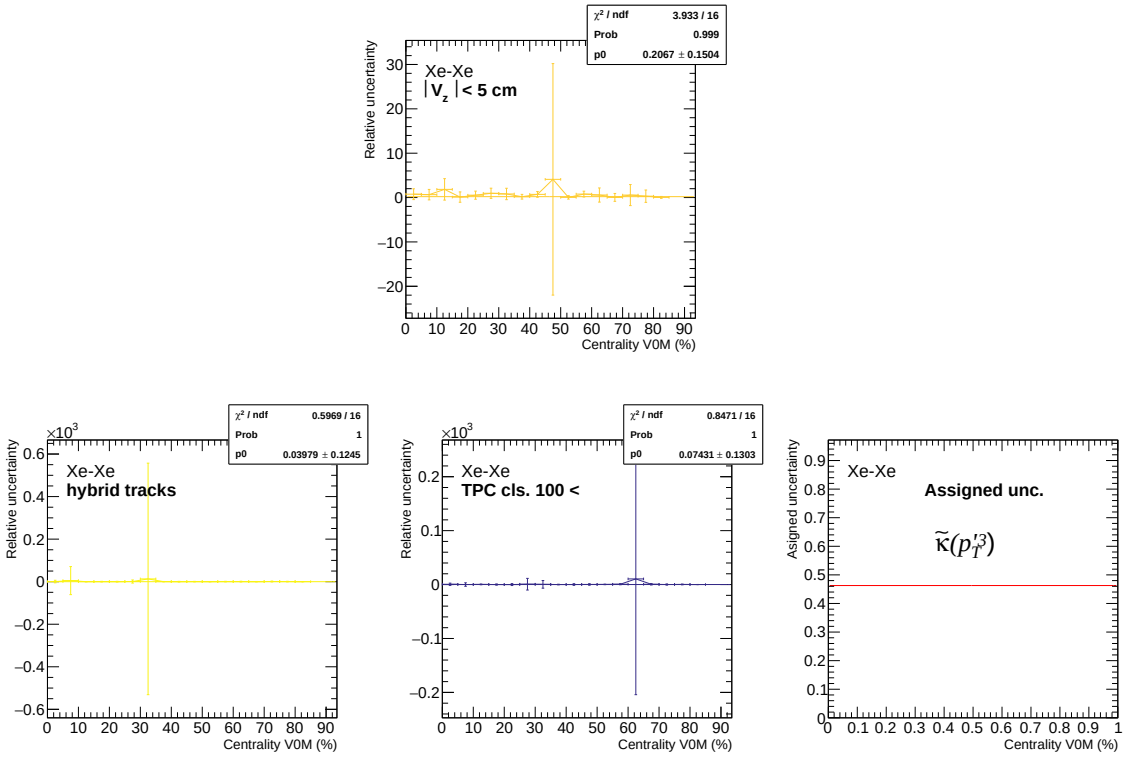

Figure C.24

D AMPT Production

This section aims to go over AMPT model configuration used for simulating collisions of deformed nuclei as presented in this thesis. Additionally the post processing of data are also reviewed as many steps are needed before it can be compared to real data. The post processing covers initial calculation of the particles momentum to a more appropriate basis, as well as check on the produced particles spectra, where the latter is mainly used for to make sure only charged particles are used. Additionally, the centrality of each deformation production are calculated based on the impact parameter of the colliding nuclei.

D.1 Coordinate basis

The track record for each event contains particle momentum (p_x, p_y, p_z) and position (r_x, r_y, r_z) for all particles at the kinetic freeze-out. Though as the final state coordinates are given in cartesian basis, some calculation are made for a more appropriate set of coordinates. Firstly we let the z-axis denote the beam direction and setting $z = 0$ as the interaction point of the two colliding nuclei. We define the transverse momentum as the momentum component in the xy-plane which are calculated as

$$p_T = \sqrt{p_x^2 + p_y^2}$$

where p_x and p_y are the x and y-component of the momentum vector respectively. As viewed from a moving frame the transverse-energy and transverse-momentum are conserved measures [6, 69]. Additionally the azimuthal angle is measured around the beam line and are calculated so every angle are in the range $[0; 2\pi]$. Here it is important to note what "quadrant" of the xy-plane the particle is in as calculations depends on it.

$$\phi = \pi + \arctan_2(p_y, p_x)$$

The polar angle θ describes the relative angle of the particle with respect to the beam line. The polar angle are not *lorentz* invariant quantity under boost along the beam line[6] and are threfore not generally used in collider physics. Instead the *psuedorapidity* is used, which are defined as

$$\eta = -\ln\left[\tan\left(\theta/2\right)\right]$$

where the polar angle can be obtained by $\theta = \arccos(p_z/|\vec{p}|)$, with $\vec{p}$ being the magnitude of the momentum. With this we outline the three basic track variables used in collider physics.

$$(p_T, \eta, \phi)$$

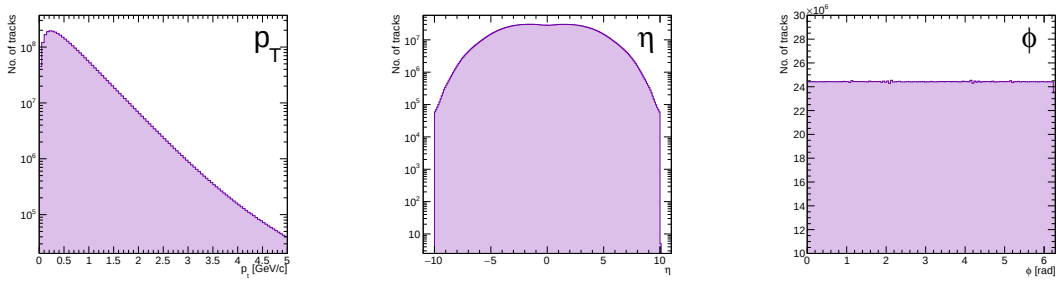

Figure D.1: Illustration of track variables as obtained in local production

D.2 Particle Yield

All final states particles in the AMPT productions are referenced by the corresponding PYTHIA particle ID[70]. The particle ID, also referred to as PDGID, follows a *Monte Carlo numbering scheme* that facilitates the particle composition and are used as a standard notation for particles in MC event generators. The numbering scheme are updated and expanded by the Particle Data Group (PDG)[69]. The particle yield pr. event in central collisions (0-30%) are drawn to make sure the final state particles at freeze-out corresponds to primary particles that can be detected in detector at the LHC and no numerical artefacts remains. External libraries are used to reference all particle PDGID with a database from where relevant information are retrieved such as charge and class (baryon, lepton etc.). The particle are split in neutral and charged as the observed particles depends on the detector setup itself.[25]

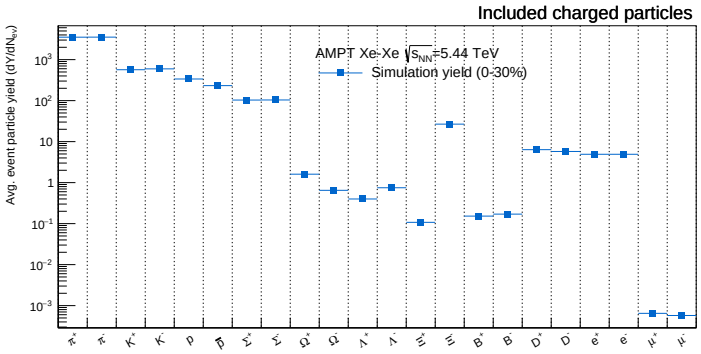

Figure D.2: Figure of the avg number of charged particles species produced in AMPT simulation of central (0-30%) Xe-Xe collision $\sqrt{s_{NN}} = 5.44$TeV

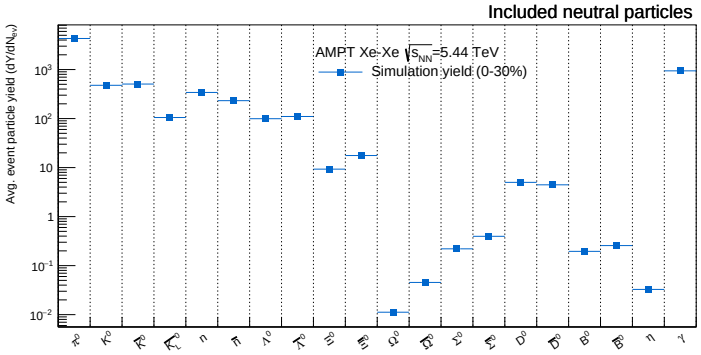

Figure D.3: Figure of the avg number of neutral particles species produced in AMPT simulation of central (0-30%) Xe-Xe collision $\sqrt{s_{NN}} = 5.44$TeV

Anomalies in production

Additional to the pr. event yield of charged and neutral particles shown in Figure D.2-D.3 some anomalies where present in terms of free quarks, gluons, *diquarks* and *Leptoquarks* (LQ^c), where the former two represent theoretical particles in *"Beyond Standard Model* physics (BSM). The combined yield of anomaly particles are 0.113 pr. event, and with an average multiplicity of $\approx$ 16K they poses no significant effect to calculation in this thesis. Regardless it is chosen to keep the yield fixed at SM particles and are therefore not included in any results presented.

[25] ALICE are a tracking detector that requires charged particle to ionise a gas along its trajectory before it can be observed. Hence neutral particles are not observed as they do not ionise matter

D.3 Centrality determination

To efficient evaluate the produced xenon collisions the centrality estimation is based on the impact parameter. This is to reduce multiplicity fluctuation and efficiently get a faster converging, and precisely result. As giving in [42] the centrality distribution based on the impact parameter are giving by

$$c_b = \frac{1}{\sigma_{\text{inel}}} \int_0^b \mathrm{d}b' \frac{\mathrm{d}\sigma_{\text{inel}}}{\mathrm{d}b'}$$

A minimum bias (MB) production are made with the purpose of centrality determination. This is also made to find a target centrality range (around 0-30%) to focus the production to central collisions. A total of 500K MB are simulated and processed. The impact parameter b distribution are sequently summed and normalised to calculate the cumulative distribution function as can be seenFigure D.4. The centrality estimator where found to be very sensitive to bin width.

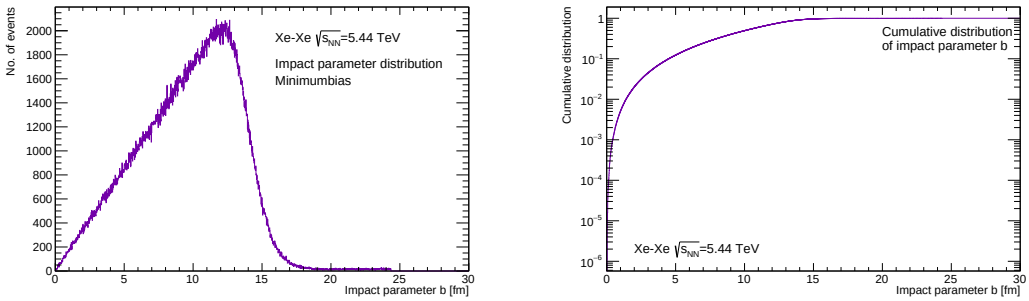

Figure D.4: AMPT Impact parameter distribution with cumulative distribution function

Though it would only be observed if the bin size where too wide. With a fine granularity bin width it where found possible to achieve a high resolution estimator by introducing and additional interpolation step. For a giving impact parameter, a linear interpolation between neighbouring bins would be created which creates a smoothening effect.

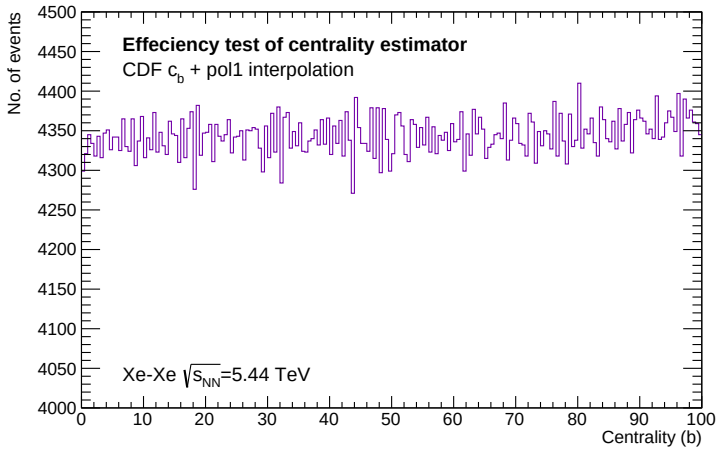

Figure D.5: Efficiency of centrality estimator for local AMPT pproduction.

E Direct calculations of multi-particle intrinsic moments

In this section, the analytical expression for obtaining the intrinsic moments of transverse momentum is provided. Following the same notation from the generic formula as presented in the chapter Analysis method we denote the moments in a numerator and denominator decomposition as

$$\langle p_T'^m \rangle = \frac{N\langle p_T'^m \rangle}{D\langle p_T'^m \rangle} \tag{E.1}$$

where $N\langle p_T'^m \rangle$ denotes the isolated momentum tuples and $D\langle p_T'^m \rangle$ the corresponding associated weight for each tuple and are given by

$$P_k \equiv \sum_{i=1}^{M} \left(w_i p_T^{(i)} \right)^k, \qquad W_k \equiv \sum_{i=1}^{M} w_i^k \tag{E.2}$$

In the following presentation of the formulas we explicitly outline $N\langle p_T'^m \rangle$ as the denominator $D\langle p_T'^m \rangle$ are obtained with the exact same coefficients just by letting $P_K \to W_k$ in the following formulas.

E.1 Four-particle moment

$$\langle p_T'^4 \rangle = \frac{1}{D\langle p_T'^4 \rangle} N\langle p_T'^4 \rangle \tag{E.3}$$

$$= \frac{1}{D\langle p_T'^4 \rangle} \left[N\langle p_T'^3 \rangle P_1 - 3N\langle p_T'^2 \rangle P_2 + 6N\langle p_T'^1 \rangle P_3 - 6P_4 \right] \tag{E.4}$$

$$= \frac{1}{D\langle p_T'^4 \rangle} \left[P_1^4 - 6P_1^2 P_2 + 8P_1 P_3 + 3P_2^2 - 6P_4 \right] \tag{E.5}$$

E.2 Five-particle moment

$$\langle p_T'^5 \rangle = \frac{1}{D\langle p_T'^5 \rangle} N\langle p_T'^5 \rangle \tag{E.6}$$

$$= \frac{1}{D\langle p_T'^5 \rangle} \left[N\langle p_T'^4 \rangle P_1 - 4N\langle p_T'^3 \rangle P_2 + 12N\langle p_T'^2 \rangle P_3 - 24N\langle p_T'^1 \rangle P_4 + 24P_5 \right] \tag{E.7}$$

$$= \frac{1}{D\langle p_T'^5 \rangle} \left[P_1^5 - 10P_1^3 P_2 + 20P_1^2 P_3 + 15P_1 P_2^2 - 30P_1 P_4 - 20P_2 P_3 + 24P_5 \right] \tag{E.8}$$

E.3 Six-particle moment

$$\langle p_T'^6 \rangle = \frac{1}{D\langle p_T'^6 \rangle} N\langle p_T'^6 \rangle \tag{E.9}$$

$$= \frac{1}{D\langle p_T'^6 \rangle} \left[c - 5N\langle p_T'^4 \rangle P_2 + 20N\langle p_T'^3 \rangle P_3 - 60N\langle p_T'^2 \rangle P_4 + 120N\langle p_T'^1 \rangle P_5 - 120P_6 \right] \tag{E.10}$$

$$= \frac{1}{D\langle p_T'^6 \rangle} \left[P_1^6 - 15P_1^4 P_2 + 40P_1^3 P_3 + 45P_1^2 P_2^2 - 90P_1^2 P_4 - 120P_1 P_2 P_3 + 144P_1 P_5 \right.$$
$$\left. -15P_2^3 + 90P_2 P_4 + 40P_3^2 - 120P_6 \right] \tag{E.11}$$

E.4 Seven-particle moment

$$\langle p_T'^7\rangle = \frac{1}{D\langle p_T'^7\rangle} N\langle p_T'^7\rangle \tag{E.12}$$

$$= \frac{1}{D\langle p_T'^7\rangle}\left[N\langle p_T'^6\rangle P_1 - 6N\langle p_T'^5\rangle P_2 + 30N\langle p_T'^4\rangle P_3 - 120N\langle p_T'^3\rangle P_4 + 360N\langle p_T'^2\rangle P_5 \right.$$
$$\left. -720N\langle p_T'^1\rangle P_6 + 720P_7\right] \tag{E.13}$$

$$= \frac{1}{D\langle p_T'^7\rangle}\left[P_1^7 - 21P_1^5P_2 + 70P_1^4P_3 + 105P_1^3P_2^2 - 210P_1^3P_4 - 420P_1^2P_2P_3 \right.$$
$$+504P_1^2P_5 - 105P_1P_2^3 + 630P_1P_2P_4 + 280P_1P_3^2 - 840P_1P_6 + 210P_2^2P_3$$
$$\left. -504P_2P_5 - 420P_3P_4 + 720P_7\right] \tag{E.14}$$

E.5 Eight-particle moment

$$\langle p_T'^8\rangle = \frac{1}{D\langle p_T'^8\rangle}\left[P_1^8 - 28P_1^6P_2 + 112P_1^5P_3 + 210P_1^4P_2^2 - 420P_1^4P_4 - 1120P_1^3P_2P_3 \right.$$
$$+1344P_1^3P_5 - 420P_1^2P_2^3 + 2520P_1^2P_2P_4 + 1120P_1^2P_3^2 - 3360P_1^2P_6$$
$$+1680P_1P_2^2P_3 - 4032P_1P_2P_5 - 3360P_1P_3P_4 + 5760P_1P_7 + 105P_2^4$$
$$\left. -1260P_2^2P_4 - 1120P_2P_3^2 + 3360P_2P_6 + 2688P_3P_5 + 1260P_4^2 - 5040P_8\right] \tag{E.15}$$

F Quality Check for run periods

F.1 QA For LHC17n

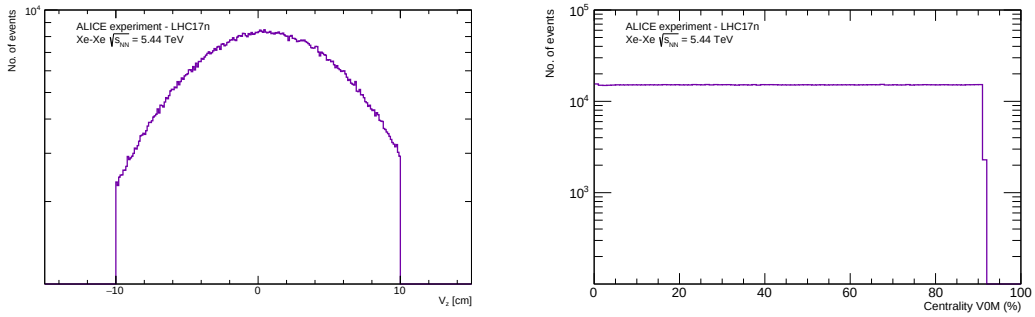

Figure F.1: QA of event selection in LHC17n for: passed triggers and V_z

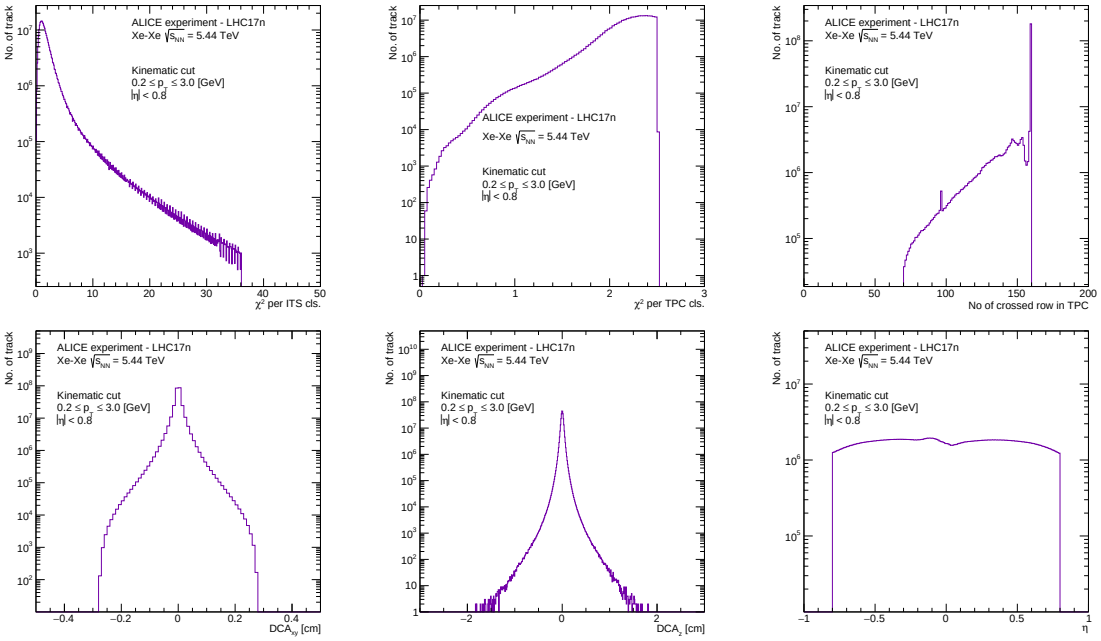

Figure F.2: QA of track selection in LHC17n for: $|DCA_{xy}|$, $|DCA_z|$, η, TPC crossed rows, $|DCA_{xy}|$, χ^2 per TPC cls., χ^2 per ITS cls.

F.2 QA For LHC18qr

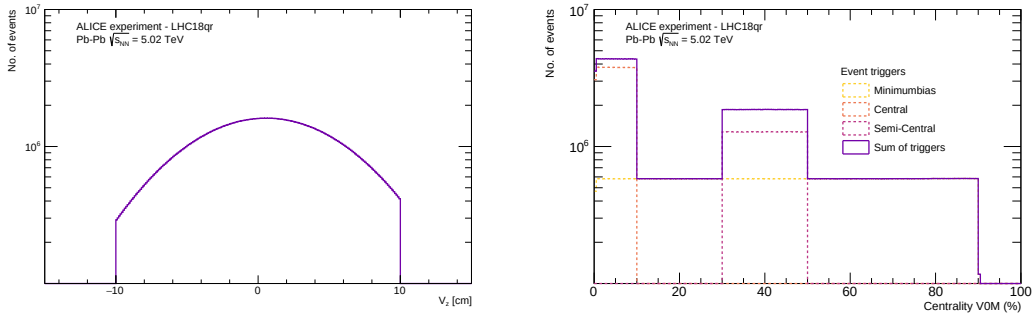

Figure F.3: QA of event selection in LHC18qr for: passed triggers and V_z

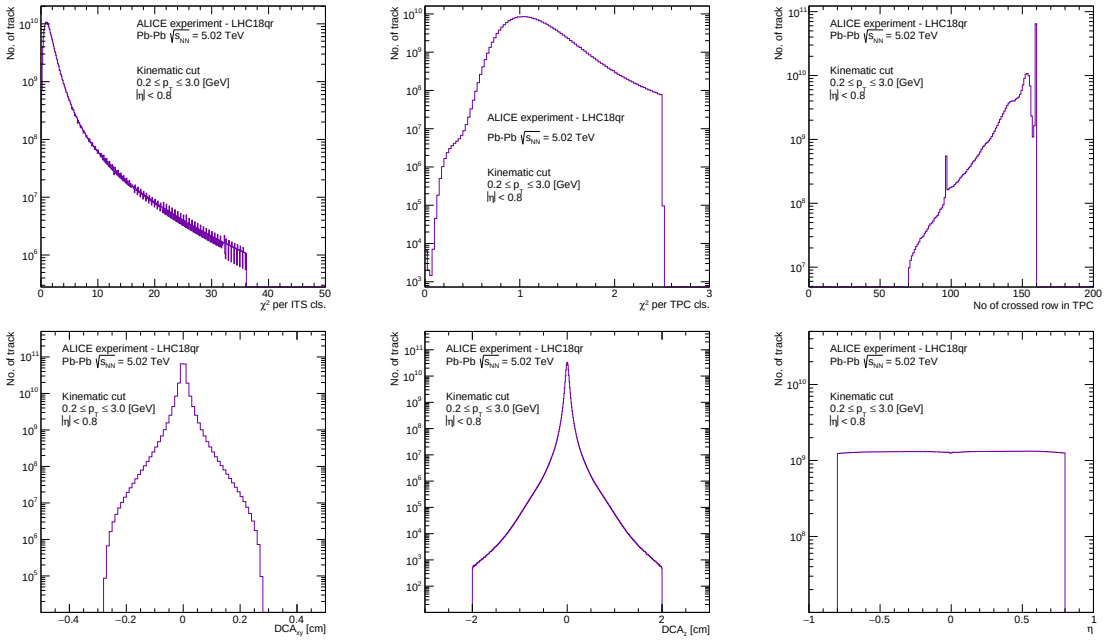

Figure F.4: QA of track selection in LHC18qr for: $|DCA_{xy}|$, $|DCA_z|$, η, TPC crossed rows, $|DCA_{xy}|$, χ^2 per TPC cls., χ^2 per ITS cls.

F.3 QA For LHC15o

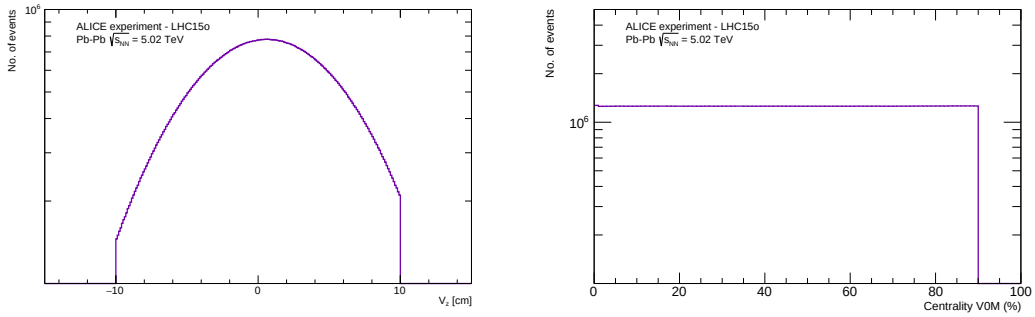

Figure F.5: QA of event selection in LHC15o for: passed triggers and V_z

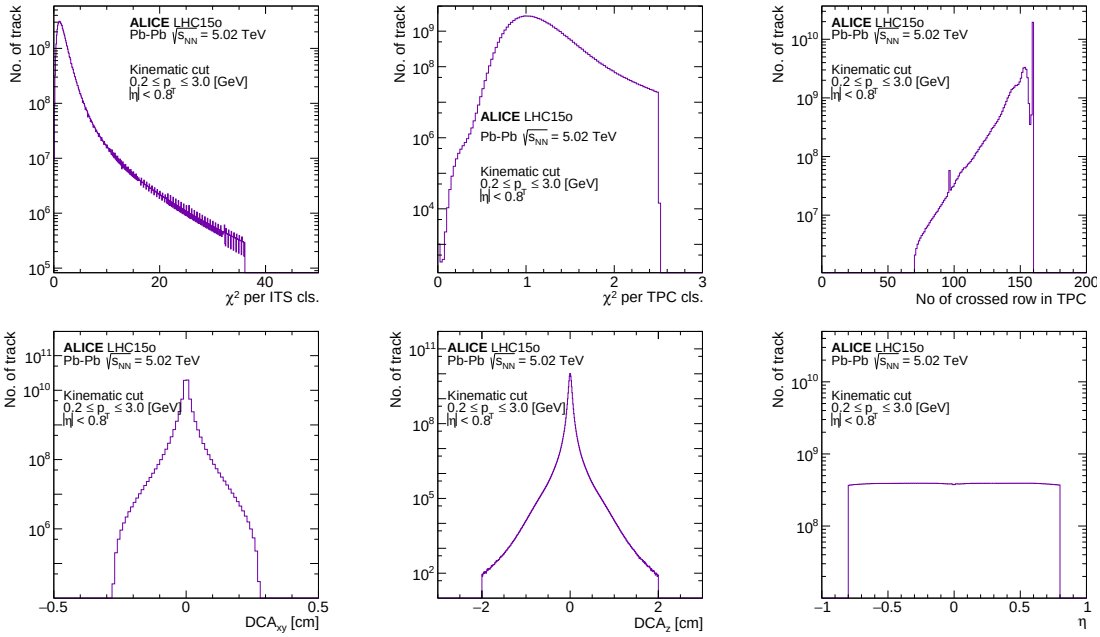

Figure F.6: QA of track selection in LHC15o for: $|DCA_{xy}|$, $|DCA_z|$, η, TPC crossed rows, $|DCA_{xy}|$, χ^2 per TPC cls., χ^2 per ITS cls.

G Joint cumulants

First presented in [56] a method for obtaining cumulants from moments where presented. While this method relies on joint cumulants with multiple variables which consequently produces a long sum of irreducible terms, the method can function as an important tool in analysis with cumulants. While the time frame of this project where too short to introduce higher-order cumulants in sub-events. The formulas now presented were initially going to be used for that purpose but time ran out. While the results are already known and have been presented in more mathematical papers, it is always nice to have the formulas close at hand. Following [41, 56] we can derive the most general expression for cumulants up to fourth order.

One observable
With one observable X_1 we simply have the one possibility.

$$\langle X_1 \rangle = \langle X_1 \rangle_c \tag{G.1}$$

which means the correlation of one particle is just its expectation $\langle X_1 \rangle$.

Two observable
The two observable are $\{X_1, X_2\}$ where we can identify a correlation by themself and between them.

$$\langle X_1 X_2 \rangle = \langle X_1 X_2 \rangle_c + \langle X_1 \rangle \langle X_2 \rangle$$

We recognize the first term on the RHS to be the second-order cumulant. After isolating for $\langle X_1 X_2 \rangle_c$

$$\langle X_1 X_2 \rangle_c = \langle X_1 X_2 \rangle - \langle X_1 \rangle \langle X_2 \rangle \tag{G.2}$$

where RHS shows the removal of any other possible correlation, which is per definition the two-particle cumulant.

Three observable
The three observebles are $\{X_1, X_2, X_3\}$. Beside the correlation of all three observables and the three independently there is also here three distinct ways to sort the genuine correlation of two observables.

$$\begin{aligned}\langle X_1 X_2 X_3 \rangle =& \langle X_1 X_2 X_3 \rangle_c + \langle X_1 X_2 \rangle_c \langle X_3 \rangle + \langle X_1 X_3 \rangle_c \langle X_2 \rangle \\ &+ \langle X_2 X_3 \rangle_c \langle X_1 \rangle + \langle X_1 \rangle \langle X_2 \rangle \langle X_3 \rangle\end{aligned}$$

after expanding all lower order moment in terms cumulants we obtain

$$\begin{aligned}\langle X_1 X_2 X_3 \rangle_c =& \langle X_1 X_2 X_3 \rangle - \langle X_1 X_2 \rangle \langle X_3 \rangle - \langle X_1 X_3 \rangle \langle X_2 \rangle \\ &- \langle X_2 X_3 \rangle \langle X_1 \rangle + 2 \langle X_1 \rangle \langle X_2 \rangle \langle X_3 \rangle\end{aligned} \tag{G.3}$$

Four observable
The four observable are $\{X_1, X_2, X_3, X_4\}$. We now consider five distinct ways to group the four observables with multinomial coefficient.

1. $\langle X_i X_j X_k X_l \rangle$ $(\times 1)$
2. $\langle X_i X_j X_k \rangle \langle X_l \rangle$ $(\times 4)$

3. $\langle X_i X_j\rangle\ \langle X_k\rangle\ \langle X_l\rangle$ $(\times 6)$
4. $\langle X_i X_j\rangle\ \langle X_k X_l\rangle$ $(\times 3)$
5. $\langle X_i\rangle\ \langle X_j\rangle\ \langle X_k\rangle\ \langle X_l\rangle$ $(\times 1)$

$$\begin{aligned}\langle X_1X_2X_3X_4\rangle =&\langle X_1X_2X_3X_4\rangle_c + \langle X_1X_2\rangle_c\langle X_3X_4\rangle_c + \langle X_1X_3\rangle_c\langle X_2X_4\rangle_c\\ &+ \langle X_1X_4\rangle_c\langle X_2X_3\rangle_c + \langle X_1X_2X_3\rangle_c\langle X_4\rangle_c + \langle X_1X_2X_4\rangle_c\langle X_3\rangle_c\\ &+ \langle X_1X_3X_4\rangle_c\langle X_2\rangle_c + \langle X_2X_3X_4\rangle_c\langle X_1\rangle_c + \langle X_1X_2\rangle_c\langle X_3\rangle_c\langle X_4\rangle_c\\ &+ \langle X_1X_3\rangle_c\langle X_2\rangle_c\langle X_4\rangle_c + \langle X_1X_4\rangle_c\langle X_2\rangle_c\langle X_3\rangle_c + \langle X_2X_3\rangle_c\langle X_1\rangle_c\langle X_4\rangle_c\\ &+ \langle X_2X_4\rangle_c\langle X_1\rangle_c\langle X_3\rangle_c + \langle X_3X_4\rangle_c\langle X_1\rangle_c\langle X_2\rangle_c + \langle X_1\rangle_c\langle X_2\rangle_c\langle X_3\rangle_c\langle X_4\rangle_c\end{aligned}$$

Now expanding the cumulants in term of the correlation we find

$$\begin{aligned}\langle X_1X_2X_3X_4\rangle =&\langle X_1X_2X_3X_4\rangle_c\\ &+\langle X_1X_2\rangle\langle X_3X_4\rangle + \langle X_1\rangle\langle X_2\rangle\langle X_3\rangle\langle X_4\rangle - \langle X_1X_2\rangle\langle X_3\rangle\langle X_4\rangle - \langle X_3X_4\rangle\langle X_1\rangle\langle X_2\rangle\\ &+\langle X_1X_3\rangle\langle X_2X_4\rangle + \langle X_1\rangle\langle X_2\rangle\langle X_3\rangle\langle X_4\rangle - \langle X_1X_3\rangle\langle X_2\rangle\langle X_4\rangle - \langle X_2X_4\rangle\langle X_1\rangle\langle X_3\rangle\\ &+\langle X_1X_4\rangle\langle X_2X_3\rangle + \langle X_1\rangle\langle X_2\rangle\langle X_3\rangle\langle X_4\rangle - \langle X_1X_4\rangle\langle X_2\rangle\langle X_3\rangle - \langle X_2X_3\rangle\langle X_1\rangle\langle X_4\rangle\\ &+\langle X_1X_2X_3\rangle\langle X_4\rangle - \langle X_1X_2\rangle\langle X_3\rangle\langle X_4\rangle - \langle X_1X_3\rangle\langle X_2\rangle\langle X_4\rangle - \langle X_2X_3\rangle\langle X_1\rangle\langle X_4\rangle\\ &+2\langle X_1\rangle\langle X_2\rangle\langle X_3\rangle\langle X_4\rangle\\ &+\langle X_1X_2X_4\rangle\langle X_3\rangle - \langle X_1X_2\rangle\langle X_3\rangle\langle X_4\rangle - \langle X_1X_4\rangle\langle X_2\rangle\langle X_3\rangle - \langle X_2X_4\rangle\langle X_1\rangle\langle X_3\rangle\\ &+2\langle X_1\rangle\langle X_2\rangle\langle X_3\rangle\langle X_4\rangle\\ &+\langle X_1X_3X_4\rangle\langle X_2\rangle - \langle X_1X_3\rangle\langle X_2\rangle\langle X_4\rangle - \langle X_1X_4\rangle\langle X_2\rangle\langle X_3\rangle - \langle X_3X_4\rangle\langle X_2\rangle\langle X_4\rangle\\ &+2\langle X_1\rangle\langle X_2\rangle\langle X_3\rangle\langle X_4\rangle\\ &+\langle X_2X_3X_4\rangle\langle X_1\rangle - \langle X_2X_4\rangle\langle X_1\rangle\langle X_3\rangle - \langle X_2X_3\rangle\langle X_1\rangle\langle X_4\rangle - \langle X_3X_4\rangle\langle X_1\rangle\langle X_2\rangle\\ &+2\langle X_1\rangle\langle X_2\rangle\langle X_3\rangle\langle X_4\rangle\\ &+\langle X_1X_2\rangle\langle X_3\rangle\langle X_4\rangle - \langle X_1\rangle\langle X_2\rangle\langle X_3\rangle\langle X_4\rangle + \langle X_1X_3\rangle\langle X_2\rangle\langle X_4\rangle - \langle X_1\rangle\langle X_2\rangle\langle X_3\rangle\langle X_4\rangle\\ &+\langle X_1X_4\rangle\langle X_2\rangle\langle X_3\rangle - \langle X_1\rangle\langle X_2\rangle\langle X_3\rangle\langle X_4\rangle + \langle X_2X_3\rangle\langle X_1\rangle\langle X_4\rangle - \langle X_1\rangle\langle X_2\rangle\langle X_3\rangle\langle X_4\rangle\\ &+\langle X_2X_4\rangle\langle X_1\rangle\langle X_3\rangle - \langle X_1\rangle\langle X_2\rangle\langle X_3\rangle\langle X_4\rangle + \langle X_3X_4\rangle\langle X_1\rangle\langle X_2\rangle - \langle X_1\rangle\langle X_2\rangle\langle X_3\rangle\langle X_4\rangle\\ &+\langle X_1\rangle\langle X_2\rangle\langle X_3\rangle\langle X_4\rangle\end{aligned}$$

Further it reduces to

$$\begin{aligned}\langle X_1X_2X_3X_4\rangle_c =&\langle X_1X_2X_3X_4\rangle - \langle X_1X_2\rangle\langle X_3X_4\rangle - \langle X_1X_3\rangle\langle X_2X_4\rangle - \langle X_1X_4\rangle\langle X_2X_3\rangle\\ &+ 2\Big[\langle X_1X_2\rangle\langle X_3\rangle\langle X_4\rangle + \langle X_1X_3\rangle\langle X_2\rangle\langle X_4\rangle + \langle X_1X_4\rangle\langle X_2\rangle\langle X_3\rangle\\ &+ \langle X_2X_3\rangle\langle X_1\rangle\langle X_4\rangle + \langle X_2X_4\rangle\langle X_1\rangle\langle X_3\rangle + \langle X_3X_4\rangle\langle X_1\rangle\langle X_2\rangle\Big]\\ &- \Big[\langle X_1X_2X_3\rangle\langle X_4\rangle + \langle X_1X_2X_4\rangle\langle X_3\rangle + \langle X_1X_3X_4\rangle\langle X_2\rangle + \langle X_2X_3X_4\rangle\langle X_1\rangle\Big]\\ &- 6\langle X_1\rangle\langle X_2\rangle\langle X_3\rangle\langle X_4\rangle\end{aligned} \tag{G.4}$$

List of Figures

List of Tables

List of Equations